NORTHWESTERN UNIVERSITY

Cardiac Tissue Characterization with Advanced MRI for Quantifying the Substrate of Atrial Fibrillation and Predicting Outcomes following Catheter Ablation

A DISSERTATION

SUBMITTED TO THE GRADUATE SCHOOL

IN PARTIAL FULFILLMENT OF THE REQUIREMENTS

for the degree

DOCTOR OF PHILOSOPHY

Field of Biomedical Engineering

By

Suvai Gunasekaran

EVANSTON, ILLINOIS

March 2020

Abstract

Atrial fibrillation (AF) is the most common arrhythmia in adults in the United States. Despite its prevalence, the etiology of AF and its adverse effects are not completely understood, which has made treatment of AF difficult. However, left atrial (LA) fibrosis is associated with worsening and propagating AF. Additionally, research has demonstrated a relationship between AF and fibrosis in the left ventricle (LV). While quantifying fibrosis in the heart is challenging, advances in magnetic resonance imaging (MRI) afford noninvasive detection of cardiac fibrosis. Unfortunately, these MRI techniques are not optimal for patients with arrhythmia or for quantifying fibrosis in thin cardiac structures, such as the LA. The purpose of this work was to better understand the relationship between AF and LV fibrosis and to develop a sequence to quantify fibrosis in the LA. An arrhythmia-insensitive MRI sequence was used to understand the relationship between AF and LV fibrosis. Furthermore, a study was performed to determine whether LV fibrosis in patients with AF is predictive of success of catheter ablation procedures. The results demonstrate that there is no correlation between AF and LV fibrosis, and thus LV fibrosis is not predictive of catheter ablation success. Additionally, a high resolution MRI sequence was developed for quantifying LA fibrosis using 3D late gadolinium enhancement at 1.5 T with a short scan time (6 min).

Acknowledgements

I would like to first thank my advisor, Dr. Daniel Kim for all of his help as I worked to obtain my doctoral degree. His mentorship and support has been invaluable, and I have become a stronger researcher and person because of him. Additionally, I would like to thank my other committee members, Dr. Michael Markl, Dr. Rod Passman, Dr. Jeremy Collins, and Dr. Jane Wilcox for their help and guidance. I also want to acknowledge all of my co-workers and lab mates who have provided me with day-to-day support and camaraderie making it a joy to come to lab every day. In addition, this work could not have been completed without the help of the staff and technologists at Northwestern who have been very accommodating to include my research into their busy clinical schedule. There are also have numerous other clinicians and professors that have supported my work in various ways, and I am extremely appreciative of that. I want to also thank my friends and classmates whose kindness and encouragement has allowed me to persevere even during difficult times. Finally, I would like to thank my family, my father Sundaram, mother Sujatha, and brother Suman have always been and will continue to be a constant source of support and inspiration.

List of Acronyms

ACE: Angiotensin-converting enzyme

ADC: Data converter

AF: Atrial fibrillation

AIR: Arrhythmia-insensitive rapid

ANOVA: Analysis of variance

ARB: Angiotensin II receptor blocker

BAV: Bicuspid aortic valve

BM3D: 3D block matching

BMI: Body mass index

BSA: Body surface area

b-SSFP: Balanced steady state free precession

BW: Bandwidth

CABG: Coronary artery bypass grafting

CAD: Coronary artery disease

CB: Cryoballoon

CMR: Cardiac magnetic resonance

CS: Compressed sensing

ECV: Extracellular volume fraction

EDV: End diastolic volume

EF: Ejection fraction

eGFR: Estimated glomerular filtration rate

ESV: End systolic volume

FFT: Fast Fourier transform

FID: Free induction decay

FOV: Field-of-view

GA: Golden angle

GFR: Glomerular filtration rate

GRAPPA: GeneRalized Autocalibrating Partial Parallel Acquisition

HF: Heart failure

HIPPA: Health Insurance Portability and Accountability Act

HR: Hazard ratio

ICC: Interclass correlation

IIR: Image intensity ratio

IR: Inversion recovery

IRB: Institutional review board

LA: Left atrium

LGE: Late gadolinium enhanement

LV: Left ventricle

LVD: Left ventricular dysfunction

LVEF: Left ventricle ejection fraction

LVH: Left ventricle hypertrophy

LVSD: Left ventricle systolic dysfunction

MI: Myocardial infarction

MOLLI: Modified Look-Locker inversion recovery

MRA: Magnetic resonance angiography

MRI: Magnetic resonance imaging

NMR: Nuclear magnetic resonance

NUFFT: Non-uniform fast Fourier transform

pAF: Paroxysmal atrial fibrillation

PCA: Principal component analysis

peAF: Persistent atrial fibrillation

PV: Pulmonary vein

PVI: Pulmonary vein isolation

RF: Radio-frequency

RMSE: Root mean square error

ROI: Region of interest

SA: Sinoatrial

SCMR: Society of Cardiovascular Magnetic Resonance

SENSE: Sensitivity Encoding

ShMOLLI: Shortened modified Look-Locker inversion recovery

SNR: Signal-to-noise ratio

SR: Saturation recovery

SSIM: Structural similarity index

SV: Stroke volume

TE: Echo time

TGA: Tiny golden angle

TI: Inversion time

TR: Repetition time

US: United States

XD-GRASP: eXtra-Dimensional Golden-angle RAdial Sparse Parallel

Table of Contents

List of Figures

List of Tables

1 Atrial Fibrillation

1.1 Introduction

Atrial fibrillation (AF) is the most common arrhythmia in the US (1). The rhythm of AF is "irregularly irregular" and no distinct P waves, which indicate atrial contraction, are found on electrocardiography. Unfortunately, the etiology of AF is not completely understood, which had made treatment difficult. While the exact mechanism of AF has not been established, left atrial (LA) fibrosis has been shown to be associated with worsening and propagating AF. Treatment of AF is necessary for improving potential reductions in cardiac output and preventing stroke.

1.2 Prevalence and implications of AF in the US

AF affects between 2.7 to 6.1 million Americans (1) and this is expected to double over the next 25 years (2). Patients with European descent have a lifetime risk of developing AF after age 40 of 26% for men and 23% for women (3), while African American patients have a lower AF prevalence (4). AF is associated with a 5 fold increased risk of stroke (5), 3 fold risk of heart failure (6), and 2 fold risk of both dementia (7) and death (5). In addition, AF is expensive, costing each AF patient around $8,700 per year for care, and costing the US healthcare system a total of $26 billion to treat patients with AF (8).

1.3 Classifications of AF

There are four general classifications of AF – paroxysmal, persistent, long-standing persistent, and permanent. Paroxysmal AF (pAF) refers to AF that begins suddenly and ends spontaneously within 7 days. The frequency of pAF is uncertain because in many situations, patients with pAF are asymptomatic (9). Persistent AF (peAF) is AF that begins suddenly but does not end spontaneously until after 7 days after onset. Long-standing AF refers to patients with uninterrupted AF for over one year (10). Permanent AF is used to identify patients with persistent AF for which both the patient and clinician have determined that they no longer will pursue rhythm control.

The term "lone AF" was previously used to describe patients with AF without structural heart disease. However, this term is not being used as often as it has been previously as it does not improve the understanding of the mechanism of AF or patient care (11). Therefore a more appropriate way to describe these patients is by the CHA_2DS_2-VASc score (0 for males, 1 for females). Finally, subclinical AF is a term used to describe AF detected in asymptomatic patients who did not have a prior diagnosis of AF (12).

1.4 Mechanisms of AF

1.4.1 Healthy atrial electrophysiology

Before discussing the mechanisms of AF, it is important to understand the basic electrophysiology that occurs in healthy tissue. As seen in Figure 1.1 A, in a healthy heart, a heartbeat begins in a small region, called the sinoatrial (SA) node, in the right atrium. The SA

node produces a regularly conducting electrical signal that transmit into the left atrium, allowing the atria to pump blood into their corresponding ventricles. From here, the electrical signals synchronously travel into the right and left ventricles and allow the heart to pump blood to the lungs and the rest of the body, respectively (13). Normal atria have several important properties that allow for them to function correctly. First, they have a short action-potential duration which allows for rapid cellular reactivation due to the short refractory period (14). This is different than in the ventricle where Purkinje fibers have a longer refractory period. Next, in the atria, the refractory period shortens with increasing heart rate to allow for faster beating of the heart. Finally, electrical conduction in the LA can occur very rapidly. In healthy tissue, all these characteristics work in sync to provide normal conduction and contraction.

However, in patients with AF, these properties permit the development of complex patterns of conduction and extremely rapid atrial rate. As we see in Figure 1.1 B, there is dyssynchrony within the atria, allowing for rapid and irregular contraction. This results in a rapid and irregular ventricular response which worsens overall cardiac function.

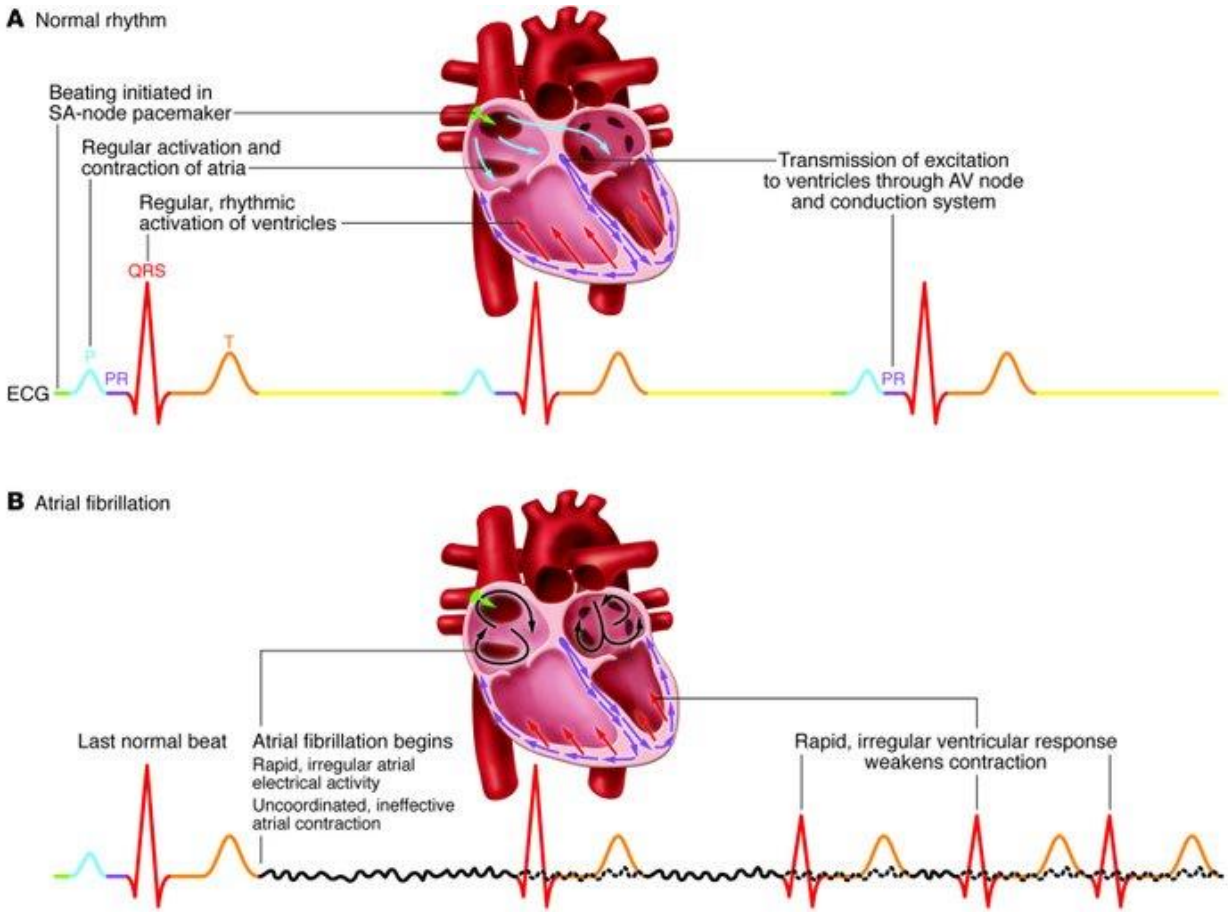

Figure 1.1: Normal rhythm vs. Atrial Fibrillation. A) In a healthy patient, there is a regular rhythm. Conduction starts in the sinoatrial (SA) node and then propagates throughout the rest of the heart. B) In atrial fibrillation, there is a regularly irregular heart beat due to the rapid and disconcerted contraction of the atria. Adapted from Wakili 2011 (13).

1.4.2 1.4.2 Triggers of AF

In AF, normal conduction through the LA is disrupted causing an uncoordinated contraction of the heart (15). While there is not one cause of AF, there are several pathophysiological mechanisms that lead to either a structural or electrophysiological abnormality which promote abnormal impulse formation and/or propagation (10) (Figure 1.2). Structural abnormalities arise when there is a disturbance in the atrial architecture. These

changes take the form of processes such as inflammation, fibrosis, and hypertrophy, which can due to an underlying heart disease (16). Electrophysiologic disturbances occur when ectopic focal discharges interfere with sinus rhythm (17). Most commonly, these focal areas of ectopic signaling occurs in the pulmonary veins (PV) (18). In addition, stretch of the LA can activate stretch sensitive ion channels which increases the likelihood of rapid firing from PVs (19). While PVs are the main source of atrial premature beats, AF can also be triggered by non-PV sites or by other types of supraventricular arrhythmias including atrioventricular nodal reentrant tachycardia, orthodromic AV reciprocating tachycardia, and atrial flutter (18, 20).

1.4.3 Maintenance of AF

Once AF is triggered, the arrhythmia can be sustained by itself, thus the description: "AF begets AF" (21). Once AF is initiated, the LA can undergo atrial and/or electrical remodeling. Atrial remodeling occurs when there are structural changes, such as fibrosis, or electrical changes, such as refractory-period dispersion, which perpetuates and maintains AF. Structural remodeling in the form of fibrosis is considered the major factor in the creation of the AF substrate. Irregular deposition of fibrosis causes heterogeneity in conduction which allows for reentrant circuits in the dilated atria (22). Electrical remodeling occurs when there is a high rate of electrical conduction which stimulates reduction in the refractory period in the myocardium (23). The tachycardia changes the refractoriness of the myocardium in a non-uniform way which perpetuates irregular and rapid conduction. Fibrosis is considered the major factor in the creation of the AF substrate. Irregular deposition of fibrosis causes heterogeneity in conduction which allows for reentrant circuits in the dilated atria (18).

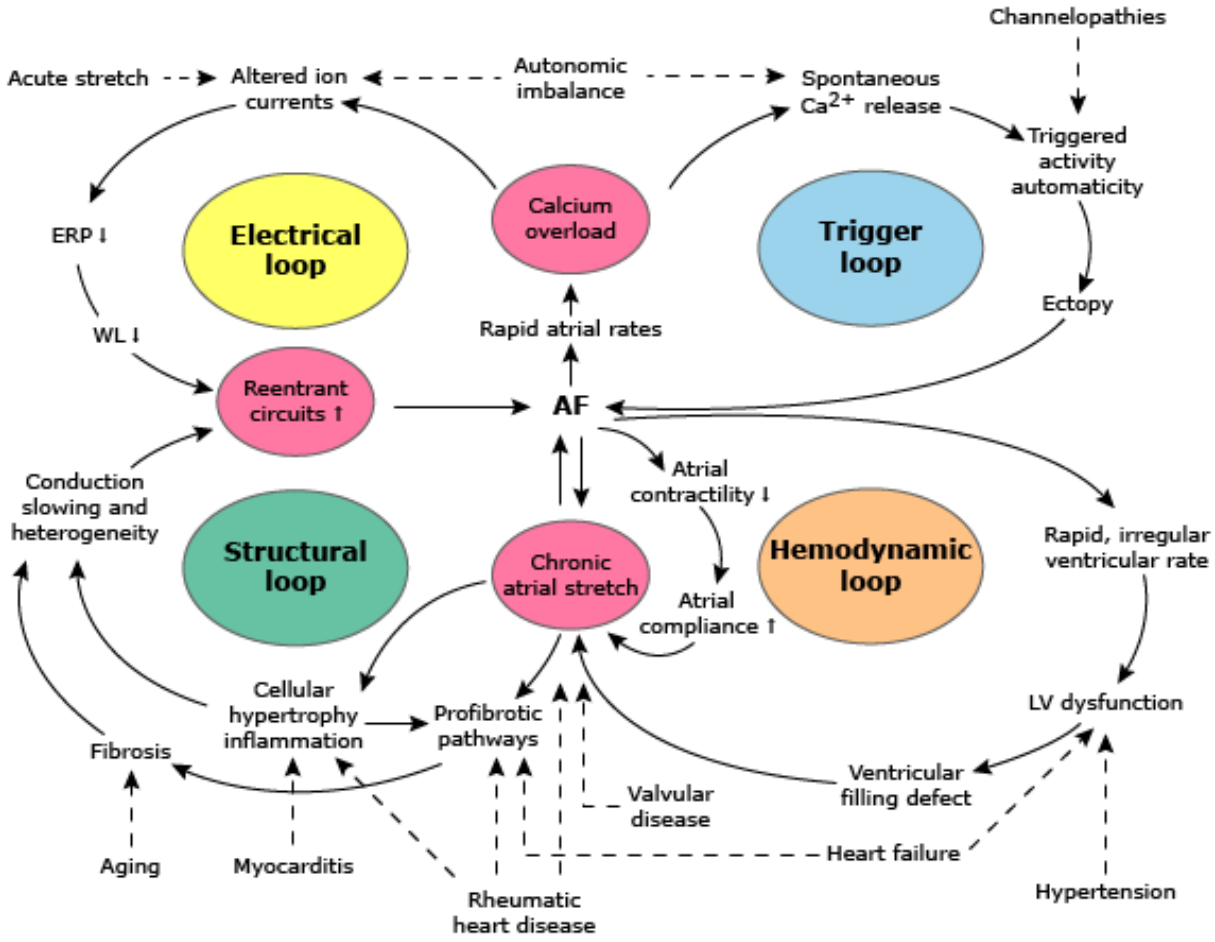

Figure 1.2: Pathophysiology of Atrial Fibrillation. The mechanism for atrial fibrillation (AF) are complex and not fully understood. There are four main contributors, the electrical loop, structural loop, trigger loop, and hemodynamic loop, but these loops interact with one another making the treatment of AF very difficult. Adapted from Schotten 2011 (18).

1.5 Biomarkers of AF

Since AF can lead to many serious consequences, such as stroke and heart failure, it is important have a well the disease well characterized to provide optimal treatment. Various medical tests are administered to assess the state of the heart which can help direct patient-specific treatment. These biomarkers include cardiac rhythm, contraction, fibrosis, and flow.

1.5.1 Rhythm monitoring

The severity of AF is determined by how long the patient is in AF as determined by electrophysiologic reports. The easiest test for detecting AF are electrocardiograms, during which electrodes are used to monitor electrical signal through the heart (24). While these tests are simple and inexpensive, they only provide a snapshot view of a patient's rhythm status. For more thorough monitoring over a longer period, holter and ZIO patch monitoring are options. These are physical devices that are attached to a patient for 2-4 weeks and continuously monitor the heart rhythm (25).

1.5.2 Ejection Fraction

To determine the efficacy of the heart's ability to pump blood, the ejection fraction (EF) is measured. The EF of the left ventricle (LV) is usually considered most important as it is a marker for the amount of blood that is pumped into the rest of the body, but in patients with AF EF of the left atrium (LA) can also be an important biomarker. EF is computed by:

$$\text{Ejection Fraction} = \frac{\text{Stroke Volume}}{\text{End Diastolic Volume}} \times 100$$

where

$$\text{Stroke Volume} = \text{End Diastolic Volume} - \text{End Systolic Volume}$$

EF is measured through imaging, most commonly echocardiography or magnetic resonance imaging (MRI) with cardiac MRI (CMR) being the gold standard technique for EF quantification (26).

1.5.3 Myocardial fibrosis

1.5.3.1 Mechanism and Types

One of the most common structural abnormalities in AF is the presence of fibrosis (27). In healthy myocardium, fibroblasts, which are a critical component of the myocardium, help provide the cellular scaffold which is required for normal mechanical function and uniform electrical conduction (28) (Figure 1.3 A). In pathological conditions, such as in AF, fibroblasts, in an attempt to repair damaged tissue, may proliferate, increase the production of collagen in the extracellular matrix, and differentiate to myofibroblats which may directly slow down conduction (29) (Figure 1.3 C). This general state produces diffuse or interstitial fibrosis and is common in the LA in patients with AF. Fibrosis can also take the form of focal or replacement fibrosis which results in dense areas of tissue (Figure 1.3 B). This most commonly occurs in the LV after a myocardial infarction. The areas of the LV that experience ischemia use fibrosis as a way to attempt to fix the damaged tissue (30).

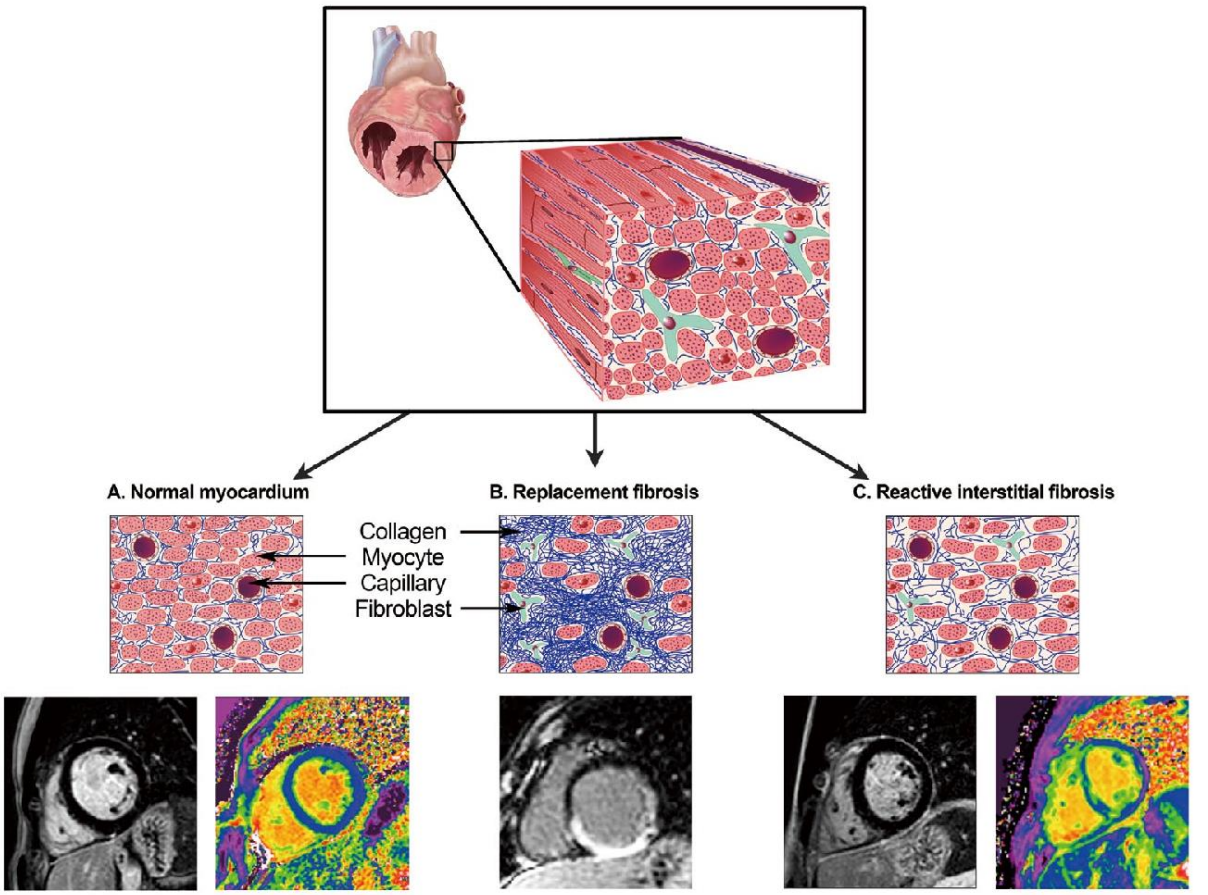

Figure 1.3: Myocardial Fibrosis. A) Healthy myocardium contains all components of the extracellular matrix, but in low levels. There is no enhancement seen on MRI. B) Replacement fibrosis is characterized by dense collagen production by fibroblasts that have filled the area. Bright areas can be seen on MRI that are enhanced by the fibrosis. C) Interstitial or diffuse fibrosis is characterized by the presence of collagen deposition by fibroblast, but the collagen is not very dense making it undetectable using traditional MRI. Adapted from Rathod 2016 (31).

1.5.3.2 Biopsy

A myocardial biopsy is the gold standard technique for quantifying myocardial fibrosis. This technique involves an invasive procedure of removing a sample of endomyocardial tissue through the internal jugular vein or femoral artery to access the right or left ventricle,

respectively (28). However, due to the invasive nature of the technique and its high rate of sampling error, a biopsy is rarely used for quantifying fibrosis.

1.5.3.3 Blood analysis

Blood serum and plasma molecules that have been proposed as markers for myocardial fibrosis such as serum carboxy-terminal telopeptide of procollagen type I, amino-terminal propeptide of procollagen type III, MMP-1, -2, and -9, and TIMP-1 (29). While these biomarkers are easy to test for, they do not provide sufficient information and are weakly associated with histology of the myocardial tissue (30).

1.5.3.4 Imaging

Another non-invasive way to measure fibrosis is through imaging through either echocardiography or MRI. Echocardiography can indirectly measure fibrosis by detecting the changes in ultrasound scattering and attenuation which is altered by increasing collagen presence in the extracellular matrix (32). MRI has been increasingly used for measuring myocardial fibrosis because MRI provides various methods to create contrast of tissue which can elucidate the presence of fibrosis (33).

1.5.4 Flow

As discussed earlier, measuring blood flow through the heart and especially in the LA is crucial for patients with AF as stasis can indicate higher likelihood of thrombus formation. There are several imaging techniques for quantifying flow.

1.5.4.1 Echocardiography

Doppler echocardiography can be used to measuring mitral inflow patterns (34). However, echocardiography is known to underestimate functional parameters of the heart (35).

1.5.4.2 Phase contrast MRI

MRI can take advantage of phase contrast imaging which allows for accurate quantification of blood flow through the heart. 2D blood flow can be used for simple flow quantification (36), while 4D flow MRI, which uses phase contrast in 3 dimensions, can be used for a thorough analysis of flow through the heart (37).

1.6 Therapeutic goals for AF

The major symptoms of AF include an increased heart rate and an irregular rhythm. To tackle these problems, there are different strategies of rate control and rhythm control which vary from medications to procedures. Additionally, an important aspect of AF treatment is stroke prevention.

1.6.1 Rate control

Commonly, the first treatment for AF is a rate control medication. Several forms of rate control medications exist such as beta blockers, calcium channel blockers, and digoxin. Most commonly beta blockers are used for rate control, but a physician personalizes medication based on the individual patient (10).

1.6.2 Rhythm control

Patients with long-term AF will use a variety of strategies to try and revert back to sinus rhythm. These include antiarrhythmic drugs, cardioversion, and catheter ablation. Antiarrhythmic drugs can be administered to attempt to restore sinus rhythm or aid electrical cardioversion. Common rhythm control medications include amiodarone, dofetilide, flecainide, and propafenone. Cardioversion is a procedure where current is applied as an electrical shock synchronized with the heart's natural beat to attempt to reset normal sinus rhythm (38). Finally, catheter ablation is a surgical intervention in which a patient has their pulmonary veins isolated by cryoballon or radiofrequency in an attempt to stop any ectopic signals that is causing the AF. Catheter ablation has been shown in many systematic reviews to be the most effective treatment for AF (39).

1.6.3 Stroke prevention

The risk of stroke from AF increases progressively with age (40). The mechanism for AF induced stroke is attributed to a combination of an abnormal atrial substrate with fibrillation

which lead to blood stasis, ultimately allowing for thrombus formation that can embolize to the brain (41). Anticoagulants are most commonly used to prevent thrombus formation, but there are complications of severe bleeding in some patients.

1.7 Gaps in AF Management

Since there is no cure for AF, the main goal for AF management is rhythm control, which as discussed above can take the form of antiarrhythmic drugs, cardioversion, or catheter ablation. Catheter ablation is superior to antiarrhythmic drugs and cardioversion for rhythm control treatment for AF, but catheter ablation success rates are moderate: 70-80% for patients with paroxysmal AF and < 70% for patients with persistent AF (42, 43). Additionally catheter ablation is generally an elective procedure which can cost $16,000 to $21,000 (44). Therefore, identifying accurate predictors for AF recurrence is important for risk stratification for optimizing patient outcomes.

Unfortunately, simple clinical characteristics (e.g. AF duration) and imaging metrics (e.g., left atrial [LA] size, left ventricular [LV] function) of AF patients have not been proven as predictors for AF recurrence. Since it is suggested that LA fibrosis is the arrhythmogenic substrate for initiating and maintaining AF in some individuals (45-48), LA fibrosis may be plausible predictor of AF recurrence following catheter ablation. CMR is a noninvasive tool that can be used for quantifying LA fibrosis, and the methods for how this works is described in the next chapter.

2 Background on MRI

2.1 Introduction

Magnetic resonance imaging (MRI) is an imaging modality that is commonly used in clinical radiology. MRI takes advantage of the intrinsic nuclear magnetic resonance (NMR) properties of human tissues for imaging organs in the body. Depending on the way the MRI sequence is configured, the machine can create different types of images based on the type of contrast produced. The data generated from these manipulations is converted to an image using the Fourier transformation.

2.2 NMR

2.2.1 Nuclear spin

Atomic and subatomic particles possess a property known as spin which is an angular momentum (Figure 2.1 A). Therefore, all protons, neutrons, and electrons possess spin and are considered to be in a constant state of rotation (49). While all molecules have some intrinsic spin, Hydrogen atoms are unique in that their nuclei are a single proton. Therefore, these protons, which are in perpetual rotation, which gives rise to a small magnetic field (Figure 2.1 B).

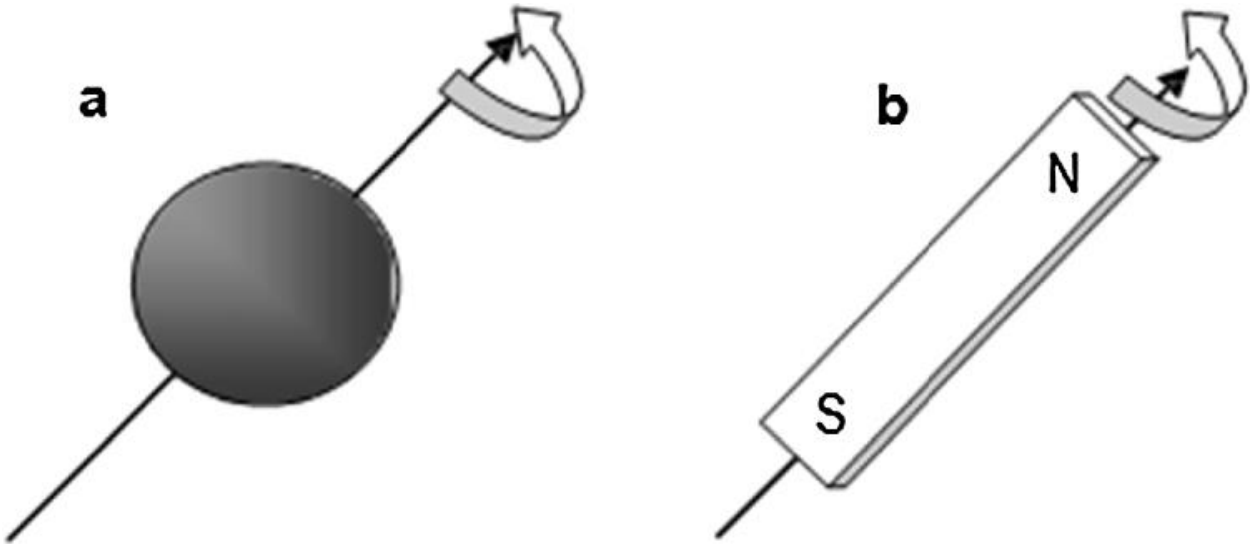

Figure 2.1: Nuclear spin. A) Diagram of the spin exhibited by a hydrogen atom. B) Demonstration that this spin creates a small magnetic field which is taken advantage of during MR imaging. Adapted from Grover 2015 (49).

2.2.2 Magnetization in a static magnetic field

Since the human body is made up mostly of water, there is an abundance of Hydrogen atoms that MRI can use for imaging. To take advantage of the small magnetic field produced by the spin of the Hydrogen proton, a large, externally applied magnet, (the main magnet of an MRI), is used to align all of these atoms along the same vector of the main magnet (B_0), which usually is at strength 1.5 T or 3 T. While all the protons are aligned with B_0, the spins can be aligned, representing a low energy state, or antialigned, representing a higher energy state (Figure 2.2 A). More spins align in the low energy state, so in the same direction as B_0, which results in a net magnetization vector, $\vec{M}$ (Figure 2.2 B).

2.2.3 2.2.3 Radio-frequency pulse

A radio-frequency (RF) pulse produces a magnetic field (B_1) that is perpendicular to that of B_0. This RF pulse is applied at a specific frequency that is tuned to magnet, called the Larmor frequency (ω_0). The frequency is determined by the Larmor equation:

$$\omega = \gamma B_0$$

where γ is the gyromagnetic ratio (4.26 MHz/Tesla for the proton). This Larmor frequency effectively rotates the proton spins from the B_0 to precess perpendicularly around B_0 (Figure 2.2 C). The idealized signal after $\vec{M}$ is tipped into the transverse plane is:

$$S(t) \sim M_{xy}(t) = M_0(\cos\omega_0 t - i\sin\omega_0 t) = M_0 e^{-i\omega_0 t}$$

The same RF coil that is used to produce the B_1 field and stimulate the spins, is also the same coil that is used to detect the signals from the excited spins. When the RF pulse is removed, the true signal is known as free-induction decay (FID), and this signal decay is due to the effects of transverse relaxation (Figure 2.2 E).

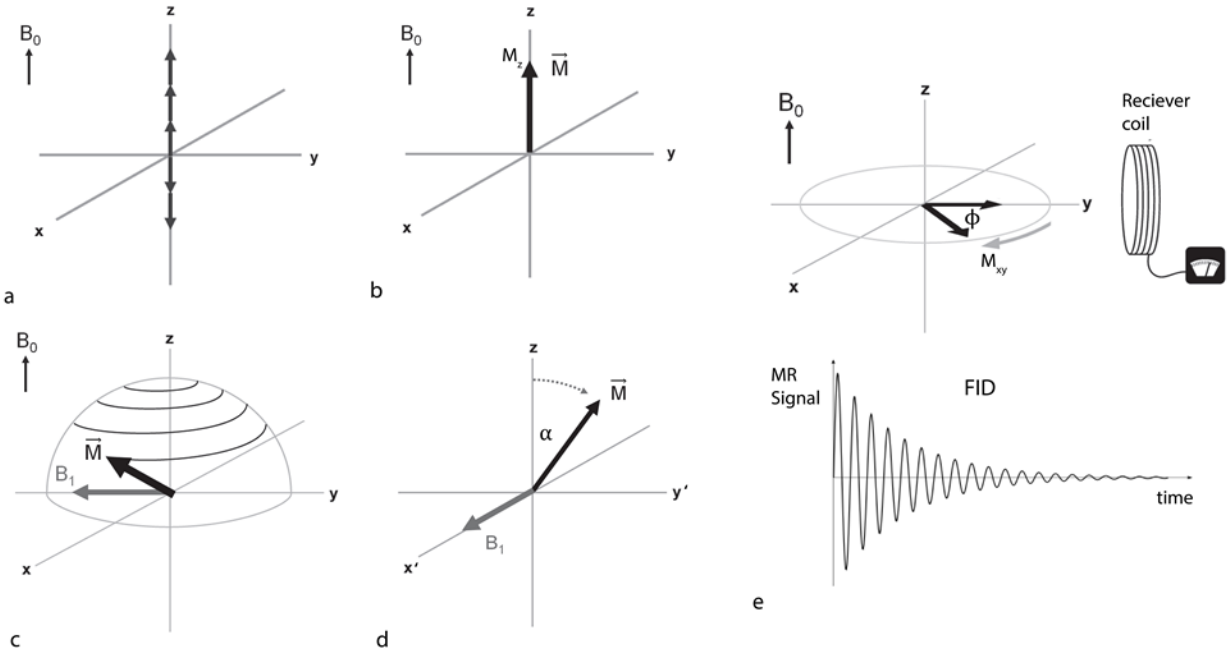

Figure 2.2: Net magnetization, excitation, and signal detection. a) When main magnetic field B_0 is applied, spins align, with more spins in the same direction with B_0 than in antialignment. b) The alignment of spins creates a net magnetization vector $\vec{M}$. c) The radiofrequency field B_1 is applied to tip $\vec{M}$ into the transverse plane by flip angle α and will precess about the z-axis; d) Tipping of $\vec{M}$ in the rotating frame. e) The precessing magnetization vector has phase ϕ and generates an oscillating signal in the receiver coil. Figure adapted from Korosec 2012 (50).

2.2.4 Longitudinal relaxation time (T_1)

The longitudinal relaxation time (T_1) represents the time it takes for the longitudinal magnetization (M_z) to return back to equilibrium after being tipped by the RF pulse. T_1 itself is the time it takes for the magnetization to reach 63% of M_0 (Figure 2.3). This value is dependent on the surrounding environment, and is commonly referred to spin-lattice relaxation. Therefore, different tissues, with different compositions, have different T_1. The behavior of M_z can be described as:

$$\frac{dM_z}{dt} = -\frac{M_z - M_0}{T_1}$$

And, can be solved as

$$M_z(t) = M_0 + (M_z(0) - M_0)e^{\frac{-t}{T_1}}$$

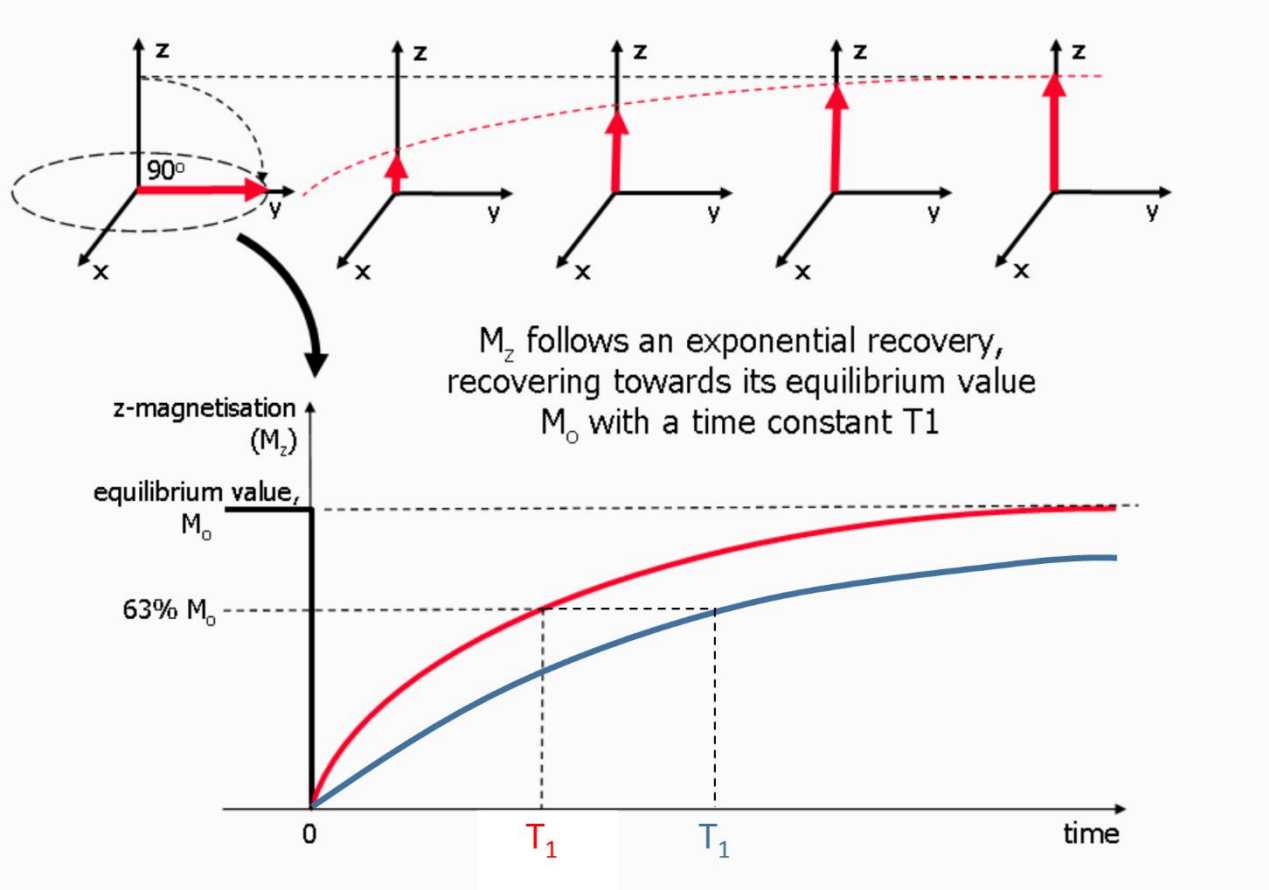

Figure 2.3: T_1 longitudinal relaxation. After the RF pulse is applied, the longitudinal component of the magnetization (M_z) will regrow exponentially until reaching equilibrium ($M_z = M_0$). T_1 is the time it takes to regrow to 63% of M_0. Here we see how two different tissues, with different T_1 and their longitudinal relaxation. Tissue with a shorter T_1 (red) will reach equilibrium more quickly than a tissue with a longer T_1 (blue). The tissue with the shorter T_1 will appear brighter in a T_1 -weighted image. Figure adapted from Ridgeway 2010 (51).

2.2.5 Transverse relaxation time (T_2)

The transverse relaxation time (T_2) represents the time it takes for the transverse magnetization (M_{xy}) to return to equilibrium, or 0. In this case, T_2 is the time it takes to decay to 37% of M_0. T_2 is a loss of signal in the transverse direction, and is due to a loss of phase coherence, so is commonly referred to as spin-spin relaxation. The behavior of M_{xy} can be described as:

$$\frac{dM_{xy}}{dt} = -\frac{M_{xy}}{T_2}$$

And solved as:

$$M_{xy}(t) = M_{xy}(0)e^{\frac{-t}{T_2}}$$

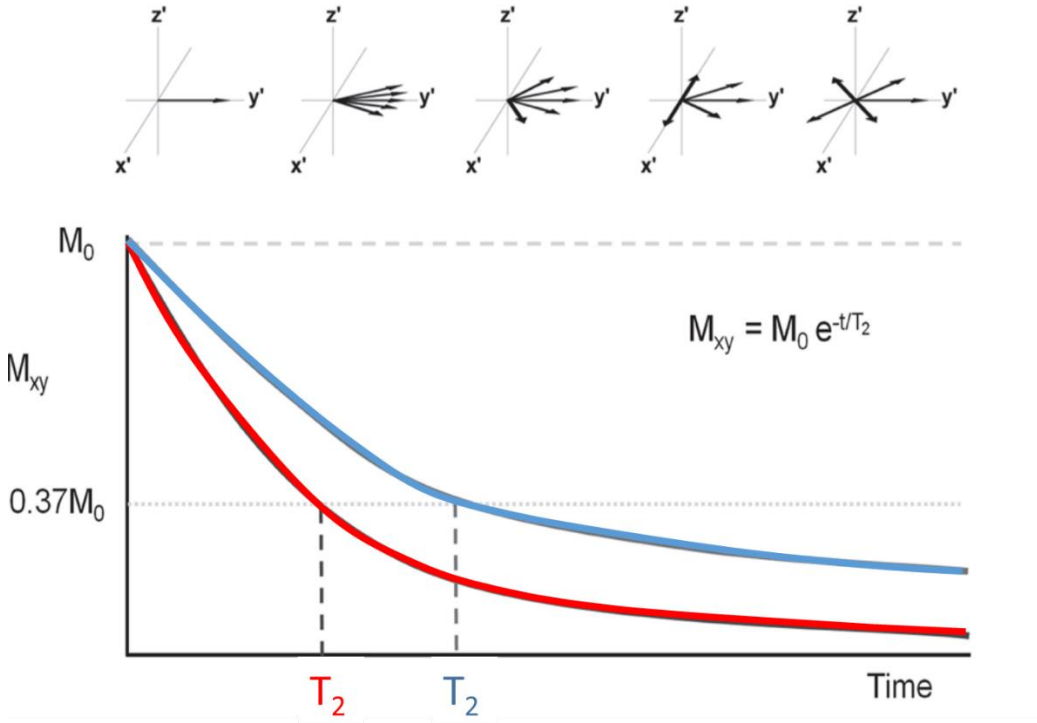

Figure 2.4: T_2 relaxation. After the RF pulse is applied, the transverse component of the magnetization (M_{xy}) will decay exponentially until reaching equilibrium ($M_{xy} = 0$). The time constant, T_2, is the time it takes to decay to 37% of M_0. Here we see how two different tissues, with different T_2 and their transverse decay. Tissue with a longer T_2 (blue) will decay more slowly than tissue with a shorter T_2 (red). The tissue with the longer T_2 will appear brighter in a T_2 -weighted image. Figure adapted from Korosec 2012 (50).

2.2.6 Transverse relation time (T_2*)

While the T_2 time is the time M_{xy} takes to return to equilibrium, due to loss of coherence, there is another factor that plays in to cause signal decay: magnetic inhomogeneities. The magnet ideally produces a constant magnetic field throughout the entire body, but in reality, this is not the case. Therefore, even small aberrations or changes in the magnetic field will cause local inhomogeneities which further dephase the signal and cause decay. This true signal loss is

represented by the time constant of T_2*. Therefore, the relationship between the spin-spin interactions (T_2), inhomogeneity of the magnetic field (T_2'), and true transverse relaxation (T_2*) is described in the following equation:

$$\frac{1}{T_2^*} = \frac{1}{T_2} + \frac{1}{T_2'}$$

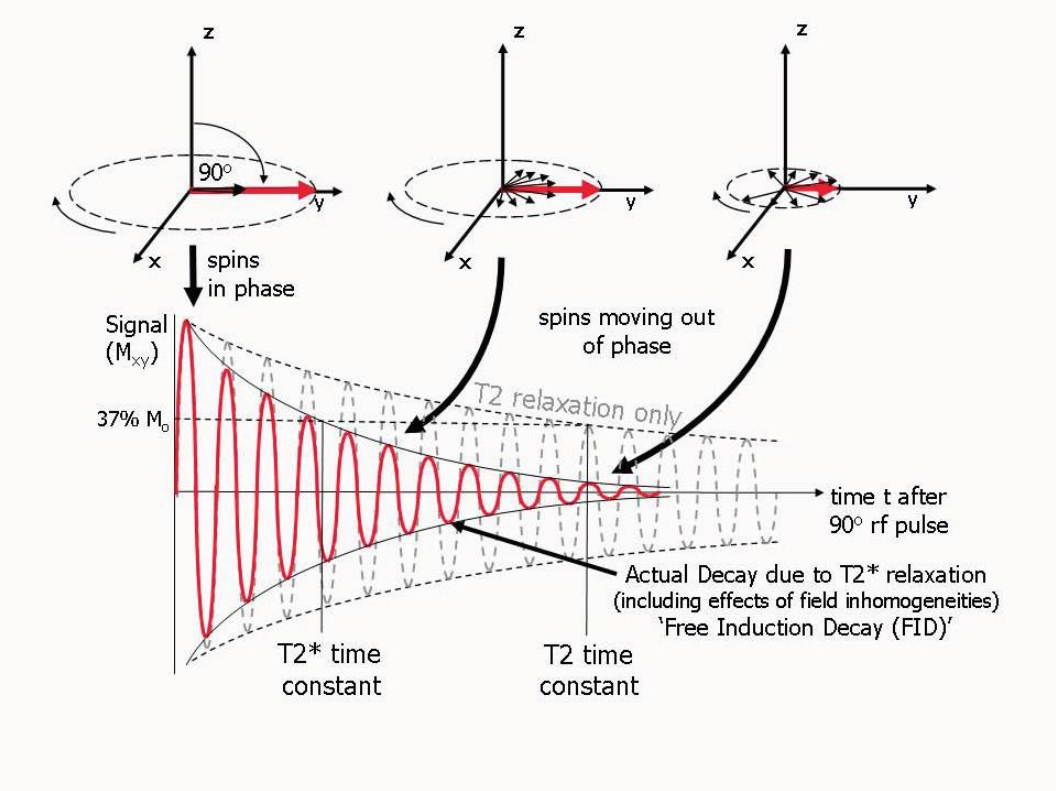

Figure 2.5: T_2 and T_2^* relaxation. Here we see the difference between the idealized T_2 relaxation and the actual FID associated T_2^* time. From Ridgeway 2010 (51).

2.2.7 Bloch equation

The behavior of the net magnetization $\vec{M}$ is described by the Bloch equation:

$$\frac{d\vec{M}}{dt} = \vec{M} \times \gamma\vec{B} - \frac{M_x i + M_y i}{T_2} - \frac{(M_z - M_0)k}{T_1}$$

Where $\vec{B}$ is the applied magnetic fields (B_0, B_1, and gradient fields) and **i**, **j**, and **k** are unit vectors in the x, y, and z directions, respectively. This equation represents both the rotation of $\vec{M}$, including precession and excitation, with the relaxation processes of T_1 and T_2, which change the length of $\vec{M}$ but not the direction.

2.3 MR Imaging

2.3.1 Image formation

In order to create an image using an MRI, several important steps must take place. First, the correct imaging slice/volume must be selected using a slice-select gradient and the appropriate RF excitation pulse. Then frequency and phase encoding gradients are used to extract the information from the region of interest, and this frequency information is captured in k-space. Finally, a Fourier transform is applied to convert the frequency information into the image domain.

2.3.1.1 Slice selection

The first step in MR image formation, is slice selection. Here two steps are required. First, a slice-selective gradient is applied perpendicular to the plane of the desired slice. Next a specially designed RF pulse is applied. This RF pulse will match the frequencies of the region desired, therefore only exciting protons in the volume of interest. The center frequency $\omega_{\mathrm{Larmor}}\,(\mathrm{z})$ for each slice is dependent on where along the slice selection gradient it is. This can be described by the equation:

$$\omega_{Larmor}(z) = \gamma(B_0 + zG_z)$$

Where γ is the Larmor frequency, B_0 is the main magnetic field strength, z is the distance along the slice selective gradient, and G_z is the slice selective gradient. Additionally, the slice thickness can be determined by the bandwidth of the RF pulse which is calculated as:

$$\mathrm{BW} = \omega(\mathrm{z}_2) - \omega(\mathrm{z}_1) = \gamma G_z(z_2 - z_2) = \gamma G_z \Delta \mathrm{z}$$

Where z_1 and z_2 are the range of z for which the slice should be selected. Once the appropriate slice has been selected with the slice selective gradient and coordinating RF pulse, the next steps in MR imaging can begin.

2.3.1.2 Frequency and phase encoding

Once the slice of interest for imaging is selected, frequency and phase encoding are used to enable the localization of 2-dimensional (2D) information. In order to localize the MR signals (FID) within a 2D plane, linear gradients are applied along both the x and y directions, similar to

how slice selection was performed along the z direction. The x direction is traditionally designed to be frequency encoding:

$$\omega(x) = \gamma(B_0 + G_x x)$$

and the gradient in the y direction provides a phase shift and thus is phase encoding:

$$\omega(y) = \gamma(B_0 + G_y y)$$

Thus, together the location within a 2D slice is:

$$\omega(x,y) = \gamma(B_0 + G_x x + G_y y)$$

In the case of 3D imaging, an additional partition encoding gradient (Gs) is required to control the Larmor frequency in the partition direction (z). This results in the equation for a 3D volume:

$$\omega(x,y,z) = \gamma(B_0 + G_x x + G_y y + G_s z)$$

The MR signal is collected over time, and is recorded with frequency encoding at an echo time (TE) after the initial RF pulse. This process of acquiring MR signal information is repeated periodically after the repetition time (TR) (Figure 2.6).

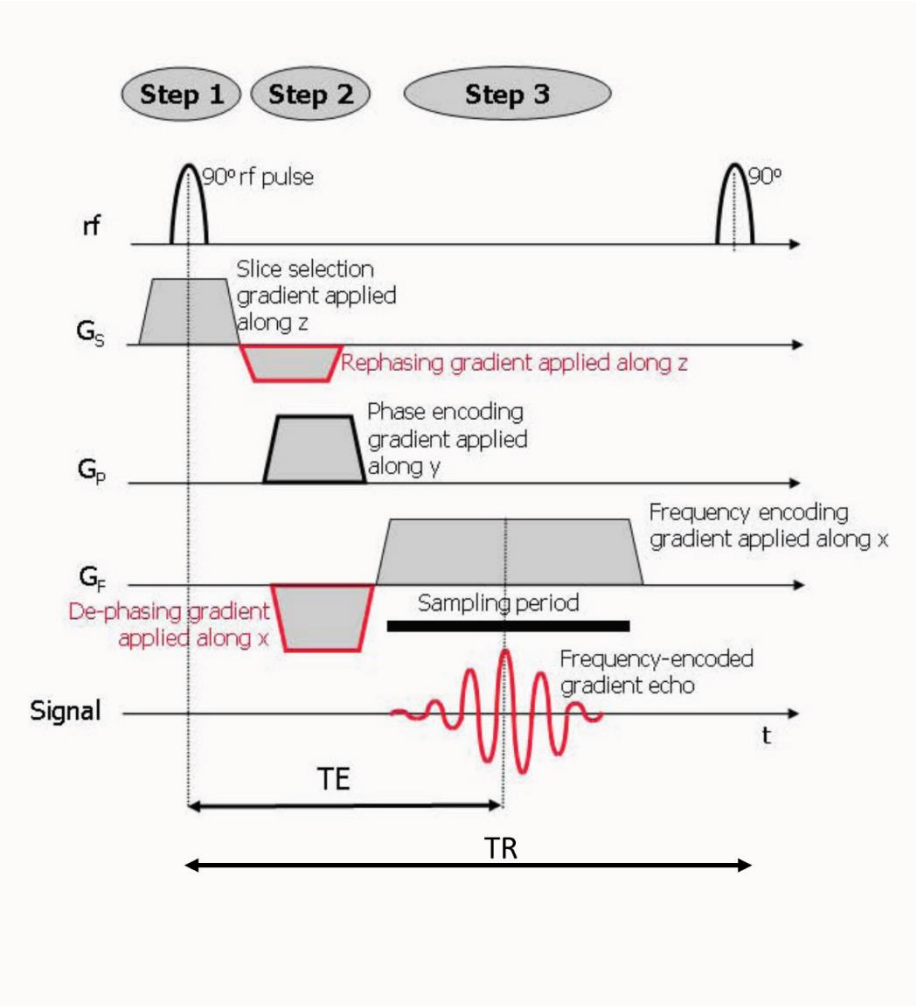

Figure 2.6: MRI pulse sequence diagram. This diagram represents how the different parts of the MRI pulse sequence works. The initial RF pulse tips the magnetization vector to the transverse plane. Then slice selection is applied along z. Then phase and frequency encoding are applied in the y and x, respectively. TE is the echo time between the start of the sequence and when the signal is sampled, and TR is the repetition time between the first RF to the next one. Adapted from Ridgeway 2010 (51).

2.3.1.3 k-space

The data from the MR image is captured through the signals, $S(t)$, and represented in k-space, $S(k)$, which is a spatial frequency domain. For each slice of k-space, the equation for $S(k)$ is:

$$S\big(k_x(t), k_y(t)\big) = \int_{-\infty}^{\infty}\int_{-\infty}^{\infty} I(x,y)e^{-i2\pi(k_x(t)x+k_y(t)y)}dxdy$$

where $I(x,y)$ is an expected image, and $k_x(t) = \frac{\gamma}{2\pi}\int_0^t G_x(\tau)d\tau$, and $k_y(t) = \frac{\gamma}{2\pi}\int_0^t G_y(\tau)d\tau$. Once the data is in k-space, it is converted to image space ($I(x,y)$) by applying the inverse Fourier transform on $S(k)$ (Figure 2.7). Data in k-space is displayed in a 2D grid with principal axes k_x and k_y. Since k-space represents spatial frequencies, each point in k-space contains spatial frequency and phase information for every pixel in image space. That being said, different areas of k-space have different information necessary for forming an image. The center of k-space contains information with low spatial frequencies, which gives rise to the most important information such as general shapes and contours. The peripheral regions of k-space contain the high frequency information which are important for the fine details such as edges (Figure 2.8).

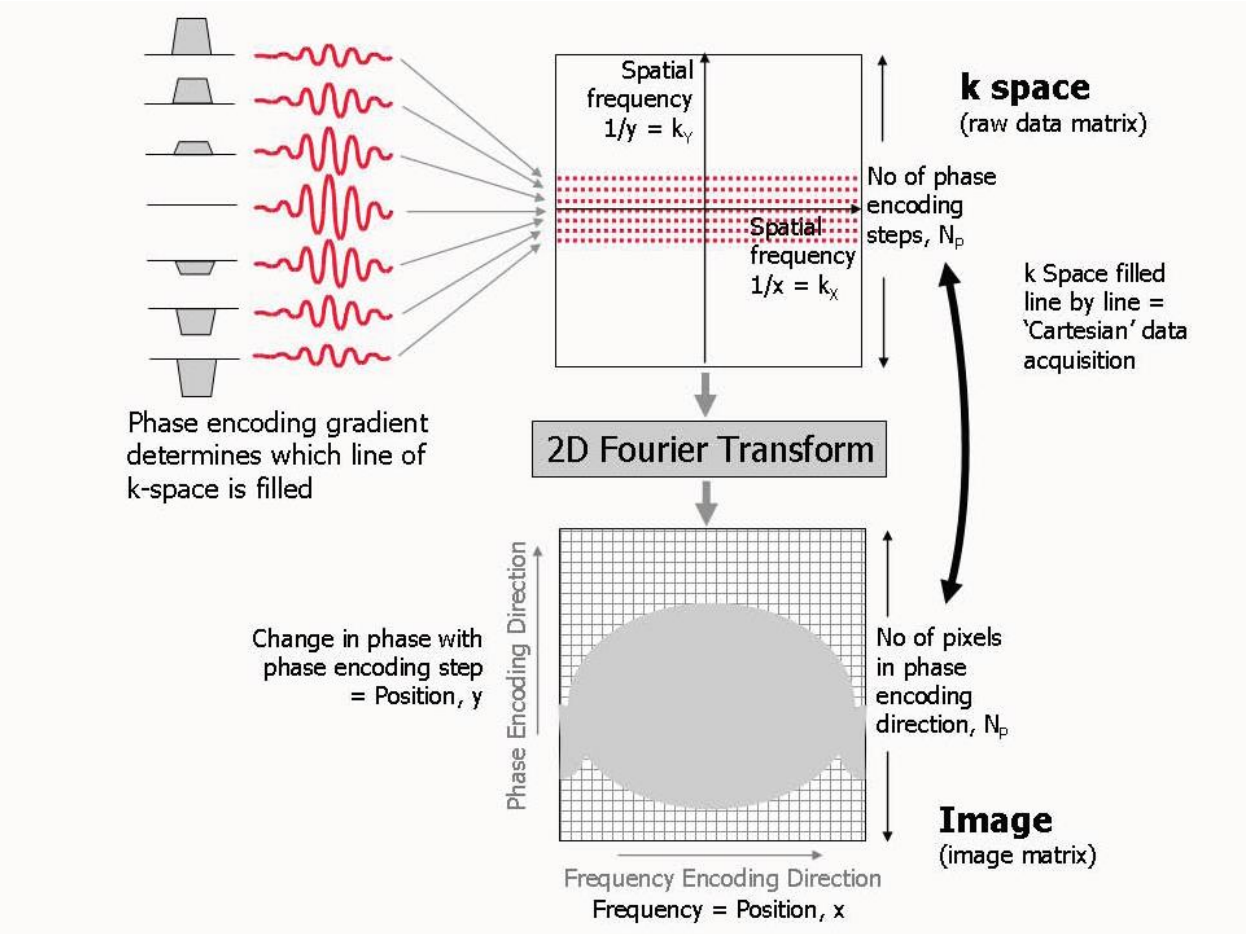

Figure 2.7: Image reconstruction. Here we see how the signals detected from the MRI are used to fill k-space and then transformed by the Fourier Transform into image space. Adapted from Ridgeway 2010 (51).

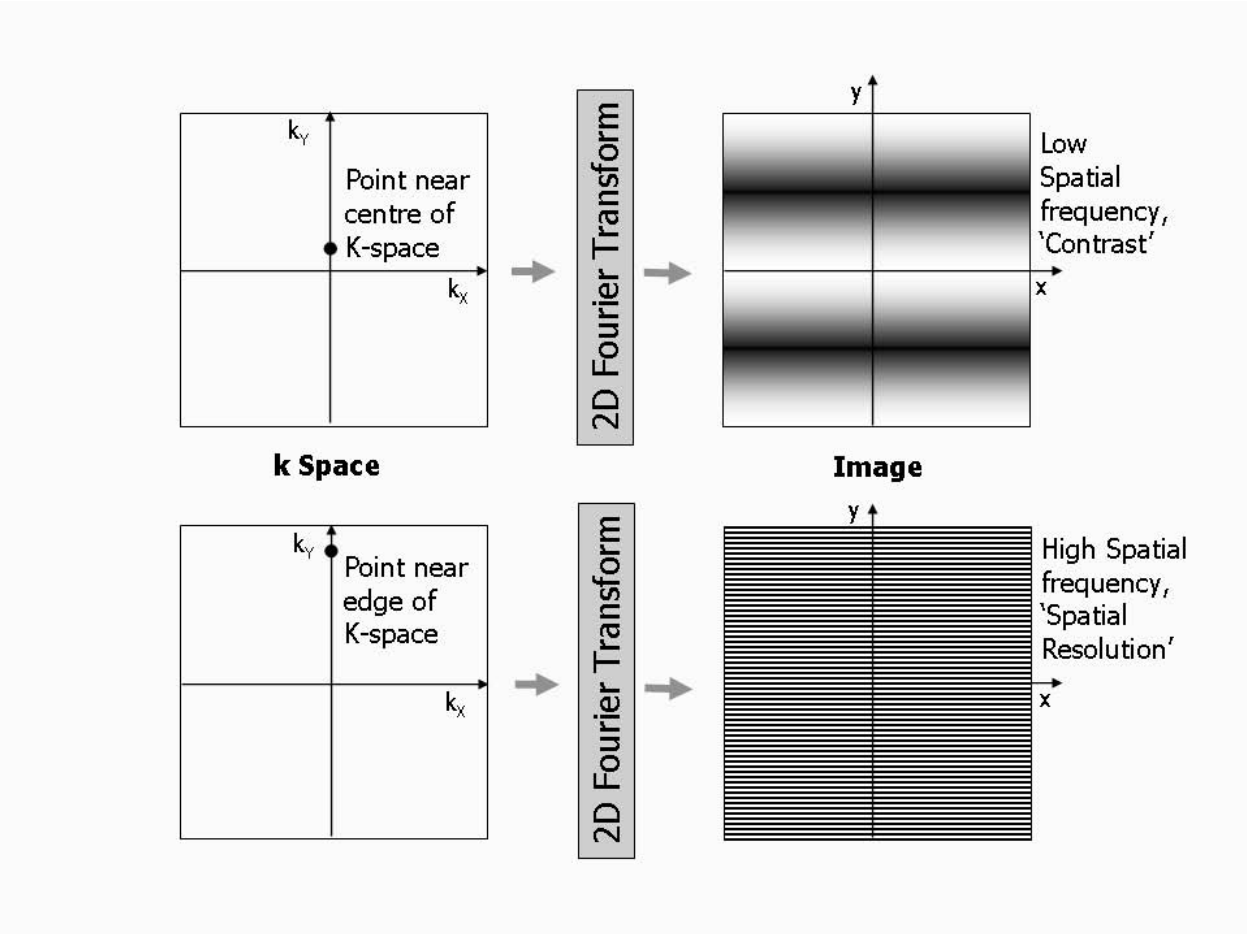

Figure 2.8: Regions of k-space. Here we see the differences between the data contained within k-space. Each point provides information in all of image space. Data in the center of k-space contains low frequency information needed for the general shape of the image. On the other hand, data near the edge of k-space contains high frequency information needed for details such as edge definition. Adapted from Ridgeway 2010 (51).

2.3.1.4 Imaging parameters

There are other important imaging parameters that are used for creating the optimal MR image. Field-of-view (FOV) refers to the distance over which the MR image is acquired. The FOV is inversely proportional to the distance between sampling points in k-space:

$$\mathrm{FOV} = \frac{1}{\Delta k}$$

Therefore, a more closely sampled in k-space an image is, the larger its FOV.

The receiver bandwidth (BW) refers to as the sampling rate for the ADC. A narrow BW is used to extend sampling time thus improving signal-to-noise (SNR). However, by reducing the BW, the image is more prone to chemical shift and susceptibility artifacts, and limits the reduction of the repetition time (TR) and echo time (TE). Therefore, BW is inversely proportional to sampling time:

$$\mathrm{BW} = \frac{1}{t_d} = \frac{1}{t_s/n_s} = \frac{n_s}{t_s}$$

where t_d is the interval between successive digital measurements, t_s is the total sampling time, and n_s is the number of complex samples digitized.

Finally, SNR represents the ability for the true signal of the MR image to be displayed in comparison with the underlying noise. SNR is proportional to voxel size and inversely proportional to BW:

$$\mathrm{SNR} \propto \Delta x \Delta y \Delta z \sqrt{\frac{1}{\mathrm{BW}}}$$

All of these parameters must be optimized in tandem to create the best image quality.

2.4 Acceleration techniques

2.4.1 Introduction

MRI, while a useful tool for imaging different information in the body, can be a time intensive test. This is due to the time required to fill k-space with the information needed to create an image. Therefore, one of the main areas of research to improve MRI is how to accelerate the scan to make it a more cost and time efficient imaging modality.

2.4.2 Sampling

The Nyquist sampling theorem states that to accurately measure a signal, the digital sampling rate must be at least twice the highest frequency contained within that signal. If Nyquist is not met, aliasing occurs and this will affect the quality of the image obtained. However, depending on the method of k-space sampling, the pattern of the aliasing will appear differently. The most common forms of k-space sampling are Cartesian and radial.

2.4.2.1 Cartesian k-space sampling

In Cartesian k-space sampling, the data in k-space is acquired in a row-by-row method where each line starts at the left side of k-space and moves along the phase encoding (k_y) direction to acquire data in a straight line. The data acquisition then goes row-by-row to collect data within the entire k-space. Therefore Cartesian sampling data is regularly spaced and can be easily converted from k-space to image space using the Fourier transform and therefore is most commonly used in clinic (52) (Figure 2.9 A). While this method is a thorough and simple way to

collect k-space information, it is a slow sampling pattern. Additionally, in Cartesian sampling, the center of k-space, which contains the most important information for image formation, is only sampled once, making this sampling sensitive to motion artifact (53). Attempts to undersample k-space using a Cartesian sampling pattern result in coherent aliasing which make the images difficult to read (52) (Figure 2.9 B). Variable density Cartesian sampling, where more lines of k-space are acquired closer to the center of k-space than the edges, does help to reduce the amount of aliasing, but still creates severe artifact (Figure 2.9 C).

2.4.2.2 Radial sampling

To overcome the challenges of Cartesian sampling, researchers developed radial k-space sampling patterns. In this sampling method, lines of k-space are acquired in a star-like fashion with every line going through the center of k-space (52) (Figure 2.9 D). In radial sampling, the center of k-space is more densely sampled compared to the outer edges, allowing for more efficient sampling of the important low frequency k-space information. Radial sampling is advantageous as it is less sensitive to motion, and undersampling in radial k-space creates incoherent artifact that can be removed using different techniques. However, radial sampling has some drawbacks compared to Cartesian sampling such as lower SNR, sensitivity to trajectory errors (54), and sensitivity to eddy currents (55). There are ways to address these issues, such as acquiring trajectory calibration scans, and optimizing the radial angles used to diminish eddy currents (55). Additionally, data collected in a radial fashion does not fall into a regularly spaced rectangular matrix, and so is converted by a nonuniform Fourier transform (NUFFT) which grids

the polar data into a Cartesian grid (56). Steps like this take additional reconstruction time, making MRI sequences with a radial sampling pattern slower to be adopted in the clinic.

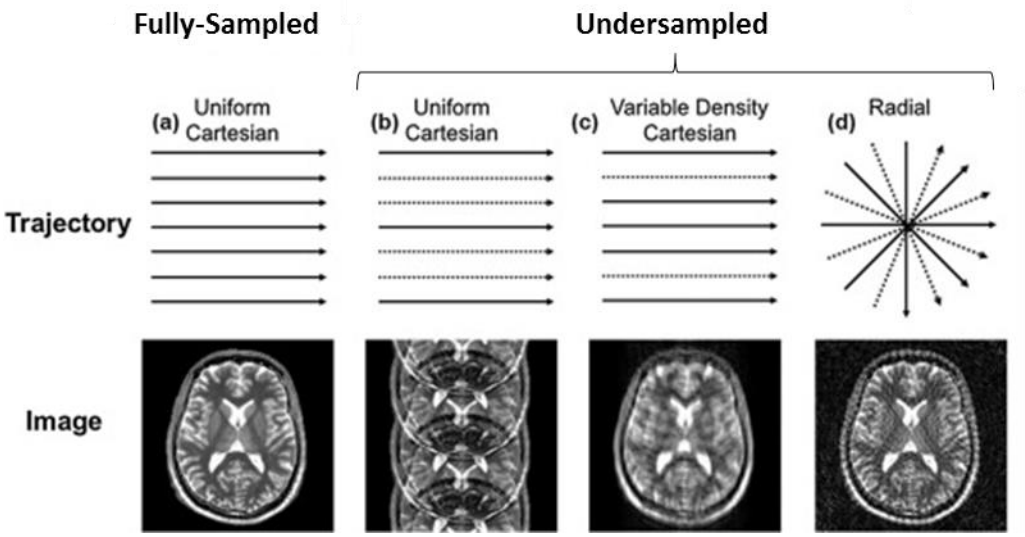

Figure 2.9: Types of k-space undersampling. A) Uniform Cartesian fully-sampled allows for data with no aliasing. B) Uniform Cartesian undersampling produces significant aliasing. C) Variable Density Cartesian does not produce significant aliasing, but suboptimal image quality. D) Radial undersampling produces high image quality due to the over sampling close to the center of k-space. Adapted from Hamilton 2017 (57).

2.4.2.3 Parallel Imaging

A popular approach for decreasing scan time is parallel imaging, such as through sensitivity encoding (SENSE) (58) or GeneRalized Autocalibrating Partially Parallel Acquisitions (GRAPPA) (59). In these parallel imaging techniques, the position of coil elements and their sensitivities are taken advantage of by imaging simultaneously to decrease scan time. This technique results in a significant reduction in scan time proportional to the acceleration factor (R). An additional benefit is the reduction in susceptibility artifacts, namely phase-related distortions. Some of the disadvantages of parallel imaging are a reduction in the SNR and

potential image-processing related artifacts, which are increased as R increases. These disadvantages can be mitigated by using a higher field strength (to increase SNR) and increasing the number of coil elements used (to reduce artifacts), but as with an acceleration technique, there are always potential for error.

2.4.2.4 Compressed sensing

A newer technique for decreasing scan time is to use an undersampled radial acquisition and deal with the incoherent artifact during image reconstruction through compressed sensing (CS). CS is a theory that states that signals can be reconstructed using sampling rates much lower than Nyquist if two conditions are met: 1. The signal is compressible allowing for sparse representation in a known transform domain, and 2. The signal frequency information was randomly undersampled (60). If these two conditions are met, the aliasing artifact appears noise-like in the transform domain and can be removed using denoising algorithms. Therefore, when a MR image (m) can be represented sparsely in a known transform domain W (sparsifying transform), m can be recovered by loving the L_1 norm minimization problem:

$$\min_{m} \|\boldsymbol{Em} - \boldsymbol{y}\|_2^2 + \boldsymbol{\lambda}\|\boldsymbol{Wm}\|_1$$

where E represents the sampling operator (multi-coil undersampling operator), y is the acquired multi-coil undersampled data, and λ is the Laplacian weight which controls the trade-off between signal sparsity and data fidelity $\|\boldsymbol{Em} - \boldsymbol{y}\|_2^2$ (61). Therefore, with CS, high levels of acceleration can be achieved data for the MR imaging. While CS allows for high levels of acceleration, the major drawback of CS is the long reconstruction times and the requirement of machines with

high computational power. This generally requires off-line reconstruction, which makes the translation of CS based sequences to the clinic slow.

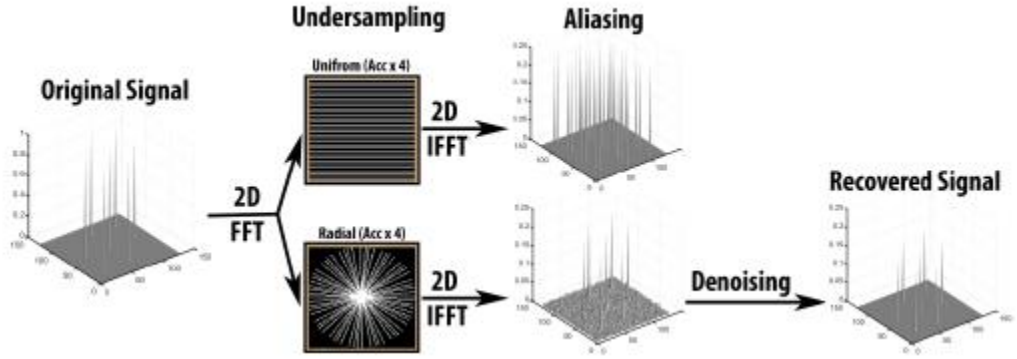

Figure 2.10: Compressed Sensing. If the original signal is undersampled in uniform Cartesian manner, aliasing occurs. However, if undersampling is done in a radial manner, the undersampling results in noise-like signal in the transform domain, so a threshold can be applied to recover the original signal.

2.5 Self-navigation of respiratory motion

During a CMR scan, not only is there motion by the heart beating, but also motion due to respiration. This respiratory motion is a major challenge for developing free breathing MRI pulse sequences. If there is no correction for respiratory motion, lines of k-space can be collected during different respiratory states resulting in ghosting artifacts and blurred images (62, 63). The most straightforward approach to deal with respiratory motion, is to do breath-held imaging, but this requires patients to hold their breath for up to 20 seconds, which can be difficult for patients, especially those with severe cardiac disease. Another option is to perform navigator gating that monitors respiratory motion and then only acquires data when the patient is in a specific

respiratory state (64). However, techniques like these reduce scan efficiency and thus are not optimal.

Therefore, researchers have developed pulse sequences with advanced reconstruction schemes that allow for free breathing scanning and self-navigated respiratory motion correction. Specifically, Feng et. al. developed eXtra-Dimensional Golden-angle Radial Sparse Parallel (XD-GRASP) imaging which exploits breathing motion during the reconstruction process (65). In XD-GRASP, data is collected in real time and is separated into different respiratory dimensions retrospectively based on a single navigator line of k-space that is acquired at the beginning of each readout. Then during CS reconstruction, these multiple respiratory states are used in a temporal sparsifying transform which allows for improved reconstructed image quality compared to CS reconstruction without a temporal sparsifying transform (66).

3 Clinical CMR applications

3.1 Introduction

Cardiovascular disease is the leading cause of death for both men and women in the US with approximately 610,000 deaths per year (67). To accurately prevent cardiovascular complications and treat these patients, regular clinical monitoring is required to assess clinical anatomy and function. Given the need for repeated monitoring, non-invasive techniques, such as imaging, are important. In particular MRI is a very useful non-invasive technique for imaging the heart to understand its anatomy and function.

3.2 Cine imaging

One of the foundational techniques for assessing cardiovascular health is functional imaging. Cardiac cine MRI is the gold standard for non-invasively measuring left ventricle (68) and right ventricle (69) function, but can be used for determining atrial function as well. From cine imaging, not only can general contractility and function be assessed, but also quantitative measurements can be acquired. By drawing ROIs around the blood pool and myocardium at systole and diastole, numerous measurements can be determined, namely end diastolic volume (EDV), end systolic volume (ESV), stroke volume (SV), ejection fraction (EF), and myocardial mass. Of these values, EF of the LV (LVEF) is the most commonly used metric to assess a patient's overall heart health. A LVEF >50% is normal, between 40-50% is considered LV dysfunction (LVD), and below 40% is considered heart failure (70).

3.3 T_1 weighted imaging

One of the basic MRI methods is T_1 weighted imaging which highlights differences based on the various T_1 relaxation times of different tissues. In particular, by manipulating the pulse sequence used to have a short TR and TE, the intensity difference (i.e. contrast) between different tissues is emphasized by their T_1 relaxation time.

3.4 Contrast agents

One way to influence the T_1 and T_2 relaxation times is by the use of contrast agents. Gadolinium (Gd) is the atom most commonly used in contrast agents due to its strong paramagnetic quality. Paramagentism is the ability of certain materials to become temporarily magnetized when placed in an external magnetic field. Gd contains 7 unpaired electrons that create a fluctuating magnetic field while in the presence of a MR magnet. Therefore, Gd that is intravenously administered interacts with protons (i.e. water molecules) in its vicinity allowing for an increase in T_1 and T_2 relaxation. For example, in a T_1-weighted image, a tissue with a shorter T_1 appears brighter on the image. And in the presence of Gd, the T_1 relaxation is increased, thus decreasing the T_1 time. Gd contrast agents change longitudinal relaxation rate ($R_1 = 1/T_1$) before and after contrast administration, and the change is proportional to Gd concentration (71, 72):

$$\Delta R_1 = \frac{1}{T_{1,post}} - \frac{1}{T_{1,pre}} = \gamma[Gd]$$

3.5 MRA

Magnetic resonance angiography (MRA) is a non-invasive way to image the blood vessels as a way to assess the anatomy for patients with various conditions such as bicuspid aortic valve (BAV), possible aortic aneurysm, aortic dilation, aortic dilation, and atherosclerotic stenosis. From MRA, the diameter of the aorta can be quantified which are used as an important clinical biomarker for determining when surgical intervention is necessary. If the ascending aorta or aortic sinus exhibit diameters greater than 5.5 cm, a patient is indicated for surgical intervention (73). Additionally, patients are also considered for surgical repair when their aorta exhibits a growth rate of 0.5 cm/year (74). MRA traditionally uses the power of gadolinium-based contrast administration, because immediately upon administration of Gd, the blood appears significantly brighter during imaging. Therefore, MRA scans are performed immediately after contrast administration to provide the best possible image quality for assessing the blood vessels.

3.6 LGE

One of the most powerful uses of MRI and contrast administration is late gadolinium enhancement (LGE) (75). Immediately upon administration of contrast, the blood vessels become significantly brighter on imaging due to the high concentration of contrast in the blood. As time passes after contrast administration, Gd circulates through the body and is filtered out by the kidney. However, while the Gd concentration in the blood is high, it starts to diffuse out of the blood vessels and into the extracellular space of the myocardium (Figure 3.1). Eventually the Gd will diffuse back into the bloodstream to be filtered by the kidney, but the rate of diffusion

out of the myocardial extracellular space is dependent on the material properties of the extracellular space.

In regions of the myocardium where there is a high concentration of collagen or other biomaterials due to fibrosis, the diffusion of Gd out of the tissues is slower compared to healthy myocardium. Therefore, this difference in Gd creates contrast between healthy and fibrotic tissues, and when imaged appropriately, at the correct time with an inversion recovery pulse, the healthy myocardium is nulled and the scarred tissue appears bright on the image. If there is a steady state infusion of Gd, then this LGE imaging can occur at any time after steady state has been achieved. However, in traditional MRI, Gd is administered as a single bolus, and so the timing of LGE is crucial to image the heart when Gd is preferentially concentrated in regions of fibrosis. Based on previous research, the Society of Cardiovascular Magnetic Resonance had deemed that LGE imaging should be done ~10 minutes after contrast administration (76, 77).

LV LGE is routinely used to determine areas where a patient was affected by a myocardial infarction, as the areas of scar are readily visible using LGE imaging (78). More recently, LGE of the LA is being studied since, as discussed earlier, measuring fibrosis of the LA is a potentially useful diagnostic tool for patients with atrial fibrillation (79-83). However, due to the thin nature of the LA wall (1-3 mm) compared to the LV (8-10 mm) imaging accurate LGE in the LA is difficult.

3.7 T_1 mapping

While T_1-weighted imaging simply exploits the various T_1 relaxation times of different tissues to create contrast, T_1 mapping, is a technique to actually quantify the T_1 relaxation time constant for each point in the image. Therefore, while T_1-weighted imaging provides qualitative images based on T_1 contrast of different tissues, T_1 mapping can provide a quantitative measure for tissues. Traditionally, to perform T_1 mapping, the longitudinal relaxation of the magnetization vector is plotted by imaging at different inversion times (TI) after an inversion recovery (IR) or saturation recovery (SR) RF excitation, using a T_1-weighted imaging technique. Then the T_1 can be calculated through curve fitting to the Bloch equation describing an IR or SR experiment.

As MR research as developed, numerous high resolution T_1 mapping methods have been developed (84-90). The most commonly used cardiac T_1 mapping pulse sequence is MOLLI which uses IR RF pulses, and acquires 11 single-shot T_1-weighted images over a single breath-hold (17 heartbeats) (84). While MOLLI is the most commonly used T_1 mapping sequence, it is sensitive to arrhythmia. Therefore, SR based T_1 mapping sequences were developed to be arrhythmia insensitive (87, 89).

3.8 ECV

As discussed above, T_1 mapping allows for a non-invasive quantitative measure of the T_1 relaxation time for a tissue. Many researchers have studied how to use the T_1 of the myocardium for disease determination and characterization (91-95). The value of T_1 changes after administration of contrast, specifically during the late gadolinium enhancement in the

myocardium. This change in T_1 is be dependent on the composition of the tissue – if there is more fibrosis the post-contrast T_1 will be shorter since more Gd can accumulate in the fibrotic areas. Therefore, based on the Gd kinetics, the extracellular volume (ECV) of the myocardium can be measured. ECV is a surrogate marker for fibrosis, as fibrosis is manifested as a deposition of collagen, which inherently increases the extracellular volume (Figure 3.1). As discussed above, the post-contrast T_1 mapping should occur ~10-15 min after Gd administration, because this is when Gd is preferentially concentrated in fibrotic regions of the myocardium (76, 77). The ECV can be calculated by the following equation (96):

$$\mathrm{ECV} = (1 - \mathrm{hematocrit}) \times \frac{\frac{1}{T_{1,\mathrm{myocardium,post}}} - \frac{1}{T_{1,\mathrm{myocardium,native}}}}{\frac{1}{T_{1,\mathrm{blood,post}}} - \frac{1}{T_{1,\mathrm{blood,native}}}}$$

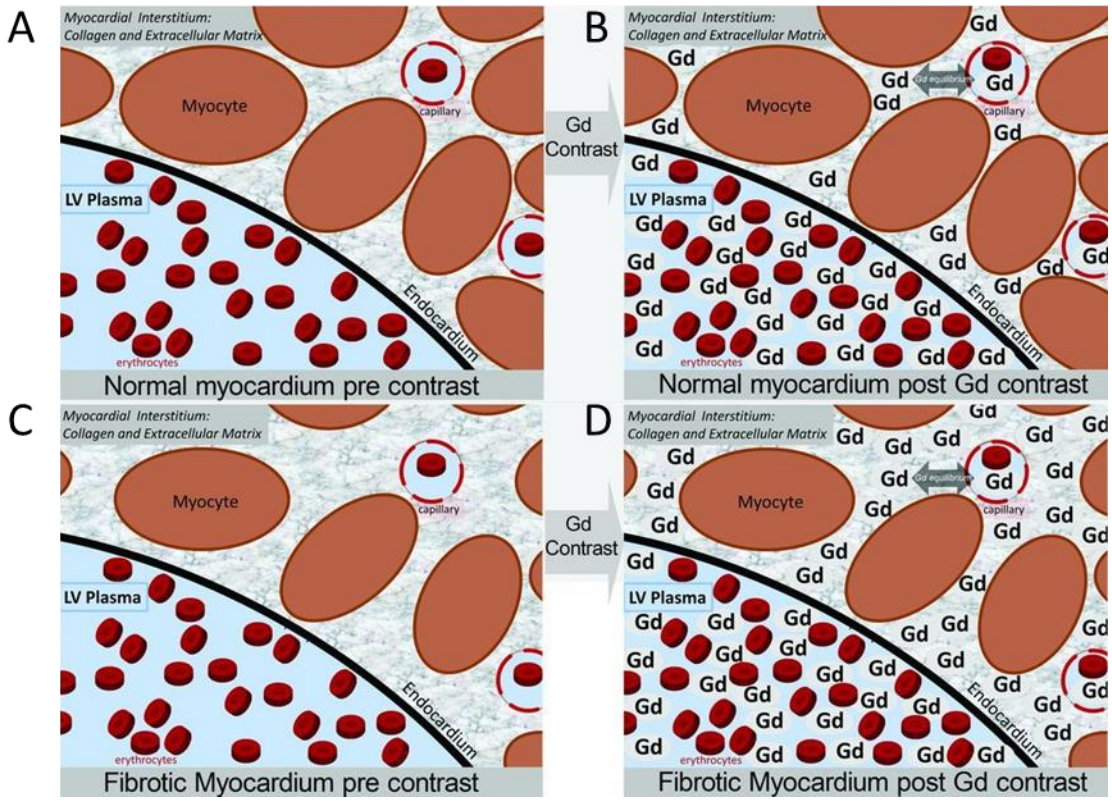

Figure 3.1: Gadolinium in fibrotic tissue. A-B) In healthy myocardium, gadolinium enters the extracellular matrix through diffusion from the bloodstream. C-D) In fibrotic myocardium, there is a much larger volume of extracellular matrix that allows for a higher concentration of Gd to accumulate. This increase in Gd created a lower T_1 of these tissues and can be used to calculate the extracellular volume (ECV) fraction. Adapted from Wong 2012 (97).

3.9 Phase contrast imaging

Another MRI technique that is useful in imaging the heart is phase contrast. This is a way to measure the actual flow through the heart and blood vessels. This technique is important for various clinical application such as valvular heart disease, congenital heart diseases, and general flow assessment (98, 99). Specifically in the context of AF, since the LA does not beat normally, the flow within the chamber can be variable and possibly allow for stasis (100, 101). Blood stasis

is a common cause for blood clot formation which can eventually lead to stroke. Therefore, it is critical to understand flow properties within the cardiovascular system to prevent these potentially deadly consequences. In phase contrast, a flow-encoding gradient is applied along the slice-selection direction of the sequence. By using the appropriate velocity encoding gradients, we can image two different velocity dependent signal phase. Subtraction of these resulting phase images allows us to quantify the velocities of the underlying flow (102).

4 Left Ventricular Extracellular Volume Expansion is not Associated with Atrial Fibrillation or Atrial Fibrillation-mediated Left Ventricular Systolic Dysfunction

4.1 Introduction

Atrial fibrillation (AF) is the most common cause of tachycardia-induced cardiomyopathy (103). Management of AF in patients with left ventricular (LV) systolic dysfunction (LVSD) or heart failure is complex and remains controversial due to mixed results produced by several randomized trials on rhythm control using either antiarrhythmic drugs or catheter ablation (104-107). A common theme in these trials is a high prevalence of confounders such as coronary artery disease (CAD), which may mute the therapeutic response. To bring clarity on this matter, the CAMERA-MRI trial randomized AF patients with idiopathic cardiomyopathy and LV ejection fraction (LVEF) $\leq$ 45% to catheter ablation or rate control, and reported significantly higher improvement in LVEF for catheter ablation (104), suggesting that AF-mediated LVSD is reversible.

For AF-mediated LVSD to be a reversible condition (105), one could surmise that AF by itself does not cause diffuse LV fibrosis. While it is well established that AF is associated with left atrial (LA) fibrosis (45), there are gaps in literature on the relationship between AF and diffuse LV fibrosis in human AF pathophysiology. Indeed, a recent editorial stated, "future studies that focus on uncovering the direction of association between atrial fibrillation and diffuse myocardial fibrosis are warranted" (106). Ling et. al. was the first group to report on the prevalence of diffuse LV fibrosis in patients with AF by measuring post-contrast cardiac T_1 with cardiovascular MR (CMR)(107). The results from this study, however, might have been influenced by the use of post-

contrast cardiac T_1 as a marker of diffuse LV fibrosis, since post-contrast T_1 mapping is known to be sensitive to biological confounders such as gadolinium clearance rate, time of measurement, contrast agent type and dose, magnetic field strength, body composition, and hematocrit. To address these confounders, the CMR community has moved towards myocardial extracellular volume (ECV) fraction mapping (108) instead, since, in the absence of myocardial edema, ECV demonstrates best overall agreement with published human histological validation studies (109). Neilan et. al. subsequently reported on the prevalence of myocardial ECV expansion in patients with AF (110). The results from this study might have been influenced by a high prevalence of LV hypertrophy (LVH), which is known to be associated with diffuse LV fibrosis (111). Moreover, the results from both studies (107, 110) might have been influenced by the imaging method used for measurement, since both used inversion-recovery based cardiac T_1 mapping pulse sequences, which may be sensitive to rapid heart rate and arrhythmia. Thus, additional studies that minimize the influence of such biological and imaging methodological confounders are warranted to determine whether ECV expanstion (i.e. diffuse LV fibrosis in the absence of myocardial edema) is associated with AF or AF-mediated LVSD in human AF pathophysiology. Clear evidence on the relationship between diffuse LV fibrosis and AF has therapeutic implications, because their lack of association may serve as another motivation for restoring sinus rhythm in AF patients with idiopathic LVSD.

In this observational study, we sought to bridge knowledge gaps by testing whether LV ECV expansion is associated with AF or AF-mediated LVSD, while minimizing the influence of biological and imaging methodological confounders. To test our hypothesis, we excluded AF patients with severe LV hypertrophy (LVH) and accurately measured LV ECV in AF ablation

candidates with and without LVSD and non-AF control patients using an arrhythmia-insensitive-rapid (AIR) cardiac T_1 mapping pulse sequence (89).

4.2 Materials and Methods

Justification for AIR Cardiac T_1 mapping for Patients with AF

Briefly, an AIR cardiac T_1 mapping pulse sequence (89) is specifically designed to achieve insensitivity to arrhythmia; it was previously validated in large animals against histology (112) and evaluated in patients with sinus rhythm to show slightly inferior precision than conventional MOLLI (113). At our institution, AIR cardiac T_1 mapping replaced conventional Modified Look Locker inversion recovery MOLLI (84) T_1 mapping in the routine clinical CMR protocol for patients with AF, because conventional MOLLI is known to produce inaccurate results in arrhythmia (89, 114)(see Figure 4.5 for an explanation and results demonstrating why AIR is preferred over conventional MOLLI in patients with AF).

Study Population

Atrial Fibrillation Patients

We identified 156 consecutive patients who underwent a pre-ablation clinical CMR at XX Hospital from June 2016 to March 2018. Among these subjects, 19 patients were excluded due to severe LVH defined as wall thickness > 1.5 cm. In total, we examined 137 patients (mean age = 62 ± 11 years, resting heart rate = 74 ± 19 beats per minute, 92 males and 45 females). The need for informed consent was waived. A retrospective study was approved by our Institutional Review Board (IRB) and was found to comply with the Health Insurance Portability and Accountability

Act (HIPAA). See Table 4.1 for patient characteristics and Table 4.2 for AF history based on clinical chart review.

Patients with a history of coronary artery disease (CAD) were defined as significant coronary stenosis (left main >50% or major epicardial stenosis >70%), a history of coronary revascularization, or prior myocardial infarction; LVSD was defined as LV ejection fraction (LVEF) < 50% from cine CMR. As per a recent white paper (11), we elected to avoid using the term "lone AF" and instead classify patients based on their CHA_2DS_2-VASc scores, for which LVSD or HF adds 1 to the score as originally proposed by Lip et al. (115). Each condition was determined based on clinical chart review.

Non-AF Patients for Establishing Control Values and Converting AIR-to-MOLLI

Ideally, native T_1 and ECV cut points should be statistically derived from age-matched healthy controls using AIR cardiac T_1 mapping, but that would have required considerable resources to conduct. We elected to use native T_1 and ECV cut points derived from a prior study of 94 healthy volunteers (mean age = 50 ± 14 years; 49 males and 45 females) scanned with conventional MOLLI cardiac T_1 mapping (116), because this study used the same MRI vendor and MOLLI protocols as our study (see below for more details). To convert native myocardial T_1 and ECV measurements between AIR and MOLLI, we prospectively enrolled 32 non-AF patients (mean age = 54 ± 16 years; resting heart rate = 69 ± 11 beats per minute; 21 males and 11 females) in sinus rhythm undergoing clinical CMR including MOLLI cardiac T_1 mapping as reference. The resulting linear models were used to convert native T_1 and ECV values between AIR and MOLLI or vice versa. This non-AF cohort also served as a control group. This sub-study was conducted in

accordance with protocols approved by our institutional review board and was Health Insurance Portability and Accountability Act compliant; all 32 patients provided written informed consent in writing. See Table 4.1 for relevant patient clinical and imaging characteristics.

MRI Experiment

AF Patients

CMR was performed on two 1.5 T whole-body MRI scanners (MAGNETOM Aera and Avanto, Siemens Healthcare, Erlangen, Germany) equipped with a gradient system capable of achieving a maximum gradient strength of 45 mT/m and a slew rate of 200 T/m/s. Radio-frequency excitation was performed with a body coil, and signal was received using the body matrix and spine array coils with 18 and 32 coil elements on the Avanto and Aera, respectively.

The relevant imaging parameters for prototype AIR cardiac T_1 mapping with balanced steady-state free precession readout are as follows: field of view = 400 mm x 300 mm, image acquisition matrix size = 192 x 144 (phase-encoding), spatial resolution = 2.1 mm x 2.1 mm, slice thickness = 8 mm, echo time (TE) = 1.1 ms, repetition time (TR) = 2.7 ms, receiver bandwidth = 930 Hz/pixel, flip angle = 55^o, generalized autocalibrating partially parallel acquisitions (GRAPPA)(59) acceleration factor = 1.8, ECG triggering, linear k-space ordering, saturation-recovery time to center of k-space (TS) = 600 ms for native and 300 ms for post-contrast. The breath-hold duration (scan time) was 5 heart beats (one proton density weighted image during heart beat 1, 4 T_1-weighted images during heart beats 2-5) per plane. This acquisition scheme enabled us to account for arrhythmia or respiratory motion by choosing one among 4 T_1-weighted images that best registers with the proton density weighted image upon visual inspection (Fig. 1). For each

subject, we performed AIR cardiac T_1 mapping in two short-axis planes (base, mid-ventricular) and one long-axis (4-chamber) plane. The apical short-axis plane was excluded due to its susceptibility to partial volume averaging around the endocardial border. Each patient received either 0.15 or 0.20 mmol/kg of gadobutrol (Gadavist, Bayer HealthCare Whippany, USA), depending on whether the estimated glomerular filtrate rate (eGFR) was 45-59 mL/min per 1.73 m^2 or $\geq$ 60 mL/min per 1.73 m^2, respectively. Post-contrast T_1 mapping was performed between 10-15 minutes after administration of gadobutrol, immediately after the clinical late gadolinium enhancement (LGE) scans. Both gadolinium dose and post-contrast T_1 mapping time adhere to recommendations made by the SCMR consensus statement (108).

Non-AF Control Patients

In 32 non-AF patients in sinus rhythm undergoing clinical CMR including MOLLI cardiac T_1 mapping in two short-axis planes (base, mid-ventricular) and one long-axis (4-chamber) plane, we additionally performed AIR cardiac T_1 mapping in the same cardiac planes as research using the same imaging parameters described above. The pulse sequence order was randomized to minimize a bias. Relevant imaging parameters for clinical MOLLI included the following: field of view = 400 mm x 300 mm, slice thickness = 8 mm, receiver bandwidth = 1085 Hz/pixel, flip angle = 35^o, GRAPPA acceleration factor = 1.8, ECG triggering, first inversion time (TI) = 100 ms, and TI increment = 80 ms. Native MOLLI T_1 mapping was performed using a 5(3)3 scheme: 8 images and 11 heartbeats scan time. Post-contrast MOLLI T_1 mapping was performed using a 4(1)3(1)2 scheme: 9 images and 11 heartbeats scan time. Our native and post-contrast MOLLI T_1 mapping protocols match the protocols used by the prior MOLLI reference study (116). For patients with

heart rate ≤ 90 beats per minute, image acquisition matrix size = 256 x 144 (phase-encoding), spatial resolution = 1.6 mm x 2.1 mm, TE = 1.1 ms, and TR = 2.7 ms. For patients with heart rate > 90 beats per min, image acquisition matrix size = 192 x 120 (phase-encoding), spatial resolution = 2.1 mm x 2.5 mm, TE = 1.0 ms, and TR = 2.4 ms.

Image Analysis

For assessment of LV ECV expansion, first reader (XX, 5th year MD-PhD student) and second reader (YY, 2nd year MS student) analyzed native T_1 and ECV maps, where ECV was calculated using the native and post-contrast T_1, the difference in blood T_1 based on contours of LV cavity, and the patient's hematocrit, taken from the same day of CMR scan, as per SCMR consensus statement (108, 117). The mean native T_1 and ECV values were calculated after manually drawing the endo- and epi-cardial contours. Using clinical LGE images as a guide, we specifically removed regions with focal fibrosis (e.g. myocardial infarction) since the goal of this study is to evaluate LV ECV expansion as a surrogate for diffuse LV fibrosis. The contour segmentation was performed using a customized tool developed in Matlab (R2017, The Mathworks Inc, Natick, MA, USA). Myocardial fibrosis was defined as native T_1 > 1233.7 ms or ECV > 32.8%. These cut points were based on two standard deviations above the norm of native T_1 (1102 ms) and ECV values (32.7%) derived from a prior study of 94 healthy volunteers (mean age = 50 ± 14 years; 49 males and 45 females) scanned with MOLLI cardiac T_1 mapping (116), which were then applied to our linear models for converting MOLLI to AIR (see Figure 4.2).

For assessment of LA end diastolic volume to body surface area (EDV/BSA), first reader (XX) used CVI[42] (Circle Cardiovascular Imaging Inc., Calgary, AB, Canada) to calculate maximum LA volume based on the area-length method (118), and BSA as determined based on the Mosteller formula. LA EDV/BSA cutoff values defined as two standard deviations above the norms taken from a previous study (LA EDV/BSA: males = 52.4 mL/m^2, females = 53.4 mL/m^2)(119).

Statistical Analysis

The intraclass correlation coefficient (ICC) with model 2, form 1 (120) was calculated to evaluate inter-reader variability in native T_1 and ECV measurements. For remaining analyses, average reader results were used. For detecting differences in 3 subgroups of patients (AF with normal LVEF, AF with LVSD, non-AF) based on clinical characteristics, we used analysis of variance (ANOVA) with Bonferroni correction for continuous variables and two-sided Fisher's Exact test with Bonferroni correction for binary variables with at least 10 samples. To test for interactions between two independent variables, we further analyzed the data using the following procedure. First, two-tailed, two-sample t-tests were used to detect differences in ECV (primary) and native T_1 (secondary) based on age (<65 vs. ≥ 65 years), sex, LVEF in all patients (normal LVEF vs. LVSD), CHA_2DS_2-VASc scores (low vs. high), LA EDV/BSA, LGE (none vs. enhancement present; vascular LGE vs. non-vascular LGE), HF, diabetes, CAD, and hypertension. For CHA_2DS_2-VASc, low corresponds to 0 for males and 1 for females, high corresponds to greater than or equal to 2. Second, for clinical variables that contribute to a significant difference

in ECV (or native T_1), two-factor ANOVA with Bonferroni correction was conducted to test for interactions between the clinical variables and ECV (or native T_1). For AF patients, we also performed linear regression analysis to test whether ECV is correlated with age, LA EDV/BSA, CHA_2DS_2-VASc, AF duration, LVEF, or GFR. $P < 0.05$ is considered statistically significant. A sample size of 169 was needed to conduct one-way ANOVA with alpha 0.05, power 0.8, and effect size greater than equal to 0.244 (i.e. borderline small). Statistical analyses were performed using IBM SPSS Statistics for Windows (Version 23.0. Armonk, NY: IBM Corp.)

4.3 Results

Figure 4.2 shows representative native and post-contrast T_1 maps and ECV maps of a non-AF patient in sinus rhythm obtained using AIR and MOLLI T_1 mapping pulse sequences. As expected, MOLLI (8-9 images, 11 heartbeats) produced higher precision in T_1 and ECV maps compared with AIR (2 images, 2 heartbeats). Figure 4.2 also shows scatter plots representing linear regression analysis on native and post-contrast T_1 and ECV measurements made using AIR and MOLLI data. According to the linear regression analysis, the native T_1 ($R^2 = 0.82$, slope = 0.95, bias = 191.64 ms), post-contrast T_1 ($R^2 = 0.89$, slope = 1.05, bias = 2.44 ms), and ECV ($R^2 = 0.83$, slope = 0.94, bias = 1.98%) measurements were strongly correlated between AIR and MOLLI. The fibrosis cut point using the corresponding linear model was 1233.7 ms for native T_1 and 32.8% for ECV.

As shown in Figure 4.3, AIR T_1 mapping CMR produced artifact-free native, post-contrast T_1, and ECV maps in this challenging cohort with arrhythmia. Native T_1 values were not

significantly (P=0.28) different between the Aera (N=56, T_1 = 1093.5 ± 101.1 ms) and Avanto (N = 101, T_1 = 1108.9 ± 75.4 ms) MRI scanners. The native T_1 and ECV measurements by two readers were in good (ICC = 0.81 for ECV) to excellent (ICC = 0.96 for native T_1) agreement. According to one-way ANOVA, neither the mean ECV (P = 0.98) nor the native T_1 (P = 0.51) was significantly different between AF patients with normal LVEF, AF patients with LVSD, and non-AF patients (Table 4.3). According to two-sample t-test, native T_1 was significantly (P<0.05) different for sex, whereas ECV was significantly (P<0.05) different for sex, age, and CHA_2DS_2-VASc (see Table 4.4). According to two-way ANOVA, there was no significant interaction between native T_1 and sex (P = 0.84); there was no significant interaction between ECV and sex (P =0.80) and between ECV and age (P =0.86), but there was significant interaction between ECV and CHA_2DS_2-VASc (P=0.045).

Compared with literature values (116), 94.9% of AF patients had native T_1 below the fibrosis cut point (1233.7 ms when converted from MOLLI to AIR) and 99.2% of patients had ECV below the fibrosis cut point (32.8% when converted from MOLLI to AIR), including a subset (n=28) of AF patients with low CHA_2DS_2-VASc (0/1 for men/women). In AF patients, ECV was weakly correlated (R^2 < 0.08) with age, LA EDV/BSA, CHA_2DS_2-VASc, AF duration, LVEF, and GFR (Figure 4.4).

4.4 Discussion

AIR cardiac T_1 maps obtained from patients with AF produced good to excellent inter-reader agreement (ICC ≥ 0.81) in native T_1 and ECV measurements. Native T_1 values were not

significantly different (P=0.33) between the Aera and Avanto 1.5 Tesla scanners, justifying our use of a single set of fibrosis cut points for data obtained from both scanners. The mean ECV was not significantly different between AF patients with normal LVEF, AF patients with LVSD, and non-AF patients. Compared with literature values, 94.9% of AF patients had native T_1 below the fibrosis cut point (1233.7 ms) and 99.2% of patients had ECV below the fibrosis cut point (32.8%), suggesting that the vast majority of our cohort did not have LV ECV expansion, including a subset of AF patients with a low CHA_2DS_2-VASc score. Our data suggest that LV ECV expansion is not associated with AF or AF-mediated LVSD.

Cardiac T_1 mapping in AF patients is technically challenging because of their irregular heart rhythm. For inversion-recovery based pulse sequences such as conventional MOLLI and Shortened MOLLI (ShMOLLI)(85) in patients with arrhythmia, multiple T_1-weighted images would be sampled at different cardiac phases, making it difficult for a motion correction algorithm to align the images. Consequently, mis-aligned T_1-weighted images may lead to significant error in T_1 quantification. Indeed, previous studies reported that MOLLI is sensitive to rapid heart rate and arrhythmia (89, 114). One approach to obtain accurate myocardial T_1 and ECV in AF patients is to use systolic variants of MOLLI (121) or ShMOLLI (122). Another approach is to use AIR, which achieves arrhythmia-insensitive T_1-weighting and reduces the image registration requirement to only two images. We posit that ECV measured in AF patients with AIR cardiac T_1 mapping more accurately reflects LV extracellular volume expansion than post-contrast T_1 or ECV measured in AF patients with inversion-recovery based cardiac T_1 mapping pulse sequences reported in previous studies (107, 110), because inversion-recovery based cardiac T_1 mapping such as conventional MOLLI is sensitive to rapid heart rate and arrhythmia (89, 114)(see Figure 4.5).

In contrast, an AIR cardiac T_1 mapping pulse sequence is less sensitive to arrhythmia because it uses saturation-recovery based T_1 weighting (87). Our short breath-hold (~5 s) AIR acquisition (see Figure 4.1) enabled us to identify at least one among 4 T_1-weighted images that best registers to the proton density weighted image for analysis, thereby minimizing sensitivity to arrhythmia and respiratory motion.

As summarized in Table 4.1, our patient population with a mean CHA_2DS_2-VASc score of 2.2 had fewer co-morbidities than prior studies (107, 110), which reflect a patient selection bias of our ablation clinic. On the other hand, this patient bias enabled us to identify 28 (20%) low-risk AF patients classified with a low CHA_2DS_2-VASc score (0 for males and 1 for females). Mean ECV of this subgroup (24.2%) was below the fibrosis cut point (32.8% when converted from MOLLI to AIR) reported by a previous study of nearly age-matched healthy controls (116), supporting our claim that LV ECV expansion is not associated with AF. Our finding is consistent with the concept of tachycardia-induced cardiomyopathy being a reversible condition (123). As shown in Figure 4.4, ECV in AF patients was weakly correlated ($R^2 < 0.07$) with LA ESV/BSA, CHA_2DS_2-VASc, AF duration, LVEF, and GFR.

Our results contradict findings by Ling et al. (107) and Neilan et. al. (110), which reported on the prevalence of diffuse LV fibrosis or myocardial ECV expansion in patients with AF. This discrepancy might be due to differences in metrics (post-contrast T_1 vs. ECV), cardiac T_1 mapping pulse sequences (inversion-recovery vs. saturation-recovery based AIR), and/or patient population (differences in co-morbidities). Our study used ECV, which is less sensitive to confounders than post-contrast T_1 used by Ling et al. Our study used AIR cardiac T_1 mapping, which is less sensitive to rapid heart rate and arrhythmia than inversion-recovery based cardiac T_1 mapping used by Ling

et al. and Neilan et al. Our study had fewer co-morbidities associated with diffuse LV fibrosis than studies by Ling et al. and Neilan et al. Our results indirectly contradict findings by Ravassa et al. (124), who reported that a combination of circulating biomarkers reflecting excessive myocardial collagen type-I cross linking and deposition is associated with higher AF prevalence in patients with heart failure. This discrepancy might be due to the non-specific nature of circulating biomarkers, which may not be able to distinguish between atrial and ventricular fibrosis. A future study is warranted to directly compare the relative strengths and weaknesses of metric (post-contrast T_1 vs. ECV) and method (saturation-recovery based AIR vs. inversion-recovery pulse sequences such as MOLLI) in a well-controlled experiment with histopathology as the reference.

This study has one major limitation that warrant further discussion. Specifically, this study did not obtain native T_1 and ECV values from age-matched healthy controls using AIR cardiac T_1 mapping. That would require considerable resources to screen and enroll age and sex-matched healthy volunteers for CMR with gadolinium based contrast agent, which is likely to be a hindrance given a growing concern for unknown health effects of gadolinium accumulation in the brain after repeated exposure to gadolinium (125). Alternatively, we elected to use control data from a prior study using identical MOLLI protocols (116) as our clinical routine and conducted an in vivo experiment to derive linear regression models for translating between AIR and MOLLI or vice versa. Our alternative approach is supported by the following set of findings and observations. First, as shown in Figure 4.2, myocardial T_1 and ECV values measured with AIR and MOLLI in our non-AF cohort were strongly correlated ($R^2 \geq 0.82$). Second, there was no significant ($P = 0.88$) difference in mean ECV measured with AIR between our AF ($24.4 \pm 2.5\%$) and non-AF cohorts ($24.4 \pm 3.8\%$). Third, mean ECV ($23.8 \pm 3.7\%$) measured with MOLLI in our non-AF

cohort was below the fibrosis cut point (32.7%) measured with identical MOLLI protocols in healthy controls published by Rosmini et al (116). Fourth, mean ECV (24.4 ± 2.5%) measured with AIR in our AF cohort was below the fibrosis cut point (32.8% when converted from MOLLI to AIR) measured with MOLLI in healthy controls published by Rosmini et al (116). Therefore, we deduce that our claim – LV ECV expansion is not associated with AF or AF-mediated LVSD – is supported by our data.

This study has other limitations. First, our patient population undergoing AF ablation at the XX hospital had fewer women than men, fewer minorities (Blacks, Hispanics, or Asians) than Whites, and fewer LVSD patients than normal LVEF patients. Thus, it remains unclear whether the results from this study reflect AF pathophysiology in the general population. Second, this study did not include changes in LVEF following catheter ablation because post-ablation LVEF data were not readily available on chart review. A future study is warranted to investigate whether the 30 patients with LVSD experience significant improvement in LVEF following catheter ablation, as reported by the CAMERA-MRI (104) and CASTLE AF (126) trials. Third, LV ECV was assessed from T_1 maps in 3 cardiac planes. While this approach is plausible for assessing diffuse LV fibrosis, we acknowledge that 3 cardiac planes do not adequately reflect the whole heart. Fourth, this study did not examine diffuse LA fibrosis due to limited spatial resolution supported by current cardiac T_1 mapping methods. A future study including high spatial resolution 3D LA T_1 mapping is warranted to examine the relationship between LA and LV ECV expansion in patients with AF. Fifth, mean LVEF in LVSD patients was only 39.7%. A future study including patients with significantly worse LVSD (LVEF < 35%) is warranted to fully verify whether LV ECV expansion is not associated with AF-mediated LVSD.

In summary, AIR cardiac T_1 mapping is recommended for measuring ECV in patients with AF, because it is insensitive to arrhythmia, rapid heart rate, and/or respiratory motion. Our results indicate that LV ECV expansion is not associated with AF or AF-mediated LVSD. Given the lack of LV ECV expansion, patients with AF-mediated LVSD are likely to benefit from restoration of sinus rhythm with catheter ablation for improvement in LVEF.

Table 4.1: Patient characteristics. Numbers in parenthesis represent percentages. One-way ANOVA with Bonferroni correction for continuous variables and two-sided Fisher's Exact test with Bonferroni correction for binary variables (with more than 10 samples) with $P < 0.05$ corresponds to statistical significance and is indicated for different pairs (* AF patients with normal LVEF vs. AF patients with LVSD; † AF patients with normal LVEF vs. non-AF patients; ℂ AF patients with LVSD vs. non-AF patients). Note, some patients had multiple LGE findings.

	AF Patients with Normal LVEF (n = 107)	AF Patients with LVSD (n = 30)	Non-AF Patients (n = 32)
Age (years)	61 ± 12†	63 ± 8ℂ	54 ± 16†ℂ
Resting Heart Rate (bpm)	73 ± 19	76 ± 16	69.3 ± 11.4
Sex			
M	65 (61)	27 (90)	21 (66)
F	42 (39)	3 (10)	11 (33)
Race			
White	101 (94)	29 (97)	28 (88)
Asian	3 (3)	1 (3)	0 (0)
Black	2 (2)	0 (0)	1 (3)
Hispanic	1 (1)	0 (0)	3 (9)
CHA_2DS_2-VASc Score	2.1 ± 1.6	2.6 ± 1.2	2.0 ± 1.5
LVEF (%)	57.7 ± 4.7*	39.7 ± 9.2*ℂ	55.0 ± 15.1ℂ

LA EDV/BSA (mL/m^2)	42.8 ± 17.3†	46.1 ± 15.0℃	33.8 ± 17.4†℃
GFR (mL/min/1.73 m^2)	74.0 ± 18.8	66.3 ± 18.2	78.0 ± 19.9
LGE findings			
None	81 (76)	19 (63)	24 (75)
Subepicardial	5 (5)	1 (3)	2 (6)
Mid-Wall	12 (11)	6 (20)	3 (9)
Subendocardial	3 (3)	1 (3)	2 (6)
Transmural	4 (4)	4 (13)	2 (6)
Heterogeneous	3 (3)	1 (3)	1 (3)
Right Ventricle Insertion Point	5 (5)	2 (7)	0 (0)
Diabetes	14 (13)	2 (7)	8 (25)
Hypertension	62 (58)	18 (60)	16 (50)
On ACE Inhibitor	20 (19)	7 (23)	5 (16)
On ARB	18 (17)	2 (7)	6 (19)
Coronary Artery Disease	19 (18)	8 (27)	4 (13)
Prior MI	11 (10)	6 (20)	3 (9)
Prior stent	6 (6)	2 (7)	0 (0)

Prior CABG	2 (2)	2 (7)	0 (0)
Severe valve disease	1 (1)	0 (0)	0 (0)
Heart Failure	10 (9)*†	14 (47)*	10 (31) †

Table 4.2: AF history of patients. Numbers in parenthesis represent percentages. Note, some patients were being treated by multiple drugs.

	All AF Patients (n = 137)	AF Patients with Normal LVEF (n = 107)	AF Patients with LVSD (n = 30)
AF type			
Paroxysmal	83 (61)	75 (70)	8 (27)
Persistent	54 (39)	32 (30)	22 (73)
AF Duration			
< 1 year	59 (43)	41 (38)	18 (60)
< 5 years	49 (36)	42 (39)	7 (23)
< 10 years	18 (13)	15 (14)	3 (10)
10 + years	11 (8)	9 (8)	2 (7)
Previous DC Cardioversion			
0	61 (44)	53 (50)	8 (27)
1	42 (31)	26 (24)	16 (53)
2	20 (15)	15 (14)	5 (17)
3+	14 (10)	13 (12)	1 (3)

Previous Ablation			
0	112 (82)	85 (79)	27 (90)
1	20 (15)	17 (16)	3 (10)
2+	5 (4)	5 (5)	0 (0)
Antiarrhythmic Drug Therapy			
Class IC	54 (39)	48 (45)	6 (20)
Class II	67 (49)	48 (45)	19 (63)
Class III	60 (44)	40 (37)	20 (67)
Class IV	24 (17)	17 (16)	7 (23)

Table 4.3: The mean AIR ECV and Native T_1 for three subgroups as shown. Values represent mean ± standard deviation.

Metric	AF Patients with Normal LVEF (n = 107)	AF Patients with LVSD (n = 30)	Non-AF Patients (n = 32)
AIR ECV (%)	24.5 ± 2.8	24.5 ± 2.6	24.4 ± 3.8
AIR Native T_1 (ms)	1109.4 ± 85.1	1092.1 ± 80.1	1114.1 ± 65.0

Table 4.4: Univariate two-tailed, two-sample t-tests in all patients (clinical variables vs. ECV, clinical variables vs. native T_1). * $P < 0.05$ corresponds to statistical significance. Note, 11 male patients with CHA2DS2-VASc = 1 were not categorized.

Variable	N	ECV (%)	P-value	Native T1 (ms)	P-value
Age (years)					
<65	101	24.1 ± 2.8	0.018*	1105.1 ± 86.9	0.68
≥65	68	25.1 ± 3.0		1110.3 ± 70.9	
Sex					
F	56	25.3 ± 2.9	0.012*	1133.9± 75.5	0.0022*
M	113	24.1 ± 2.9		1094.0 ± 80.2	
Resting Heart Rate					
Normal (HR ≤ 100 bpm)	155	24.4 ± 3.0	0.35	1105.2 ± 80.7	0.29
Tachycardia (HR > 100 bpm)	14	25.2 ± 2.5		1129.0 ± 80.2	
LVEF					
Normal (LVEF ≥ 50%)	133	24.3 ± 2.8	0.14	1109.3 ± 80.3	0.53
LVSD (LVEF < 50%)	36	25.1 ± 3.3		1099.6± 82.8	
CHA2DS2-VASc					
Low (M = 0, F = 1)	36	23.2 ± 3.1	0.0083*	1109.1 ± 88.1	0.98
High (≥ 2)	122	24.8 ± 3.0		1109.5 ± 79.4	
LA EDV/BSA (mL/m^2)					
Normal	129	24.3 ± 2.8	0.062	1100.8 ± 80.2	0.066
Elevated	40	25.3 ± 3.2		1127.7 ± 79.7	

LGE					
Present	45	25.1 ± 3.2	0.084	1111.3 ± 67.2	0.69
None	124	24.3 ± 2.8		1105.7 ± 85.3	
Vascular LGE					
Present	14	25.1 ± 2.6	0.41	1110.4 ± 44.9	0.88
None	155	24.4 ± 3.0		1106.9 ± 83.3	
Heart Failure					
Present	34	24.9 ± 3.5	0.32	1115.8 ± 93.4	0.50
None	135	24.4 ± 2.8		1105.0 ± 77.4	
Diabetes					
Present	24	25.6 ± 3.5	0.052	1124.7 ± 107.6	0.25
None	145	24.3 ± 2.8		1104.3 ± 75.4	
Coronary Artery Disease					
Present	31	24.7 ± 3.6	0.70	1113.9 ± 74.3	0.61
None	138	24.5 ± 2.8		1105.7 ± 82.2	
Hypertension					
Present	96	24.9 ± 3.0	0.067	1101.2 ± 81.5	0.27
None	73	24.0 ± 2.8		1115.1 ± 79.5	

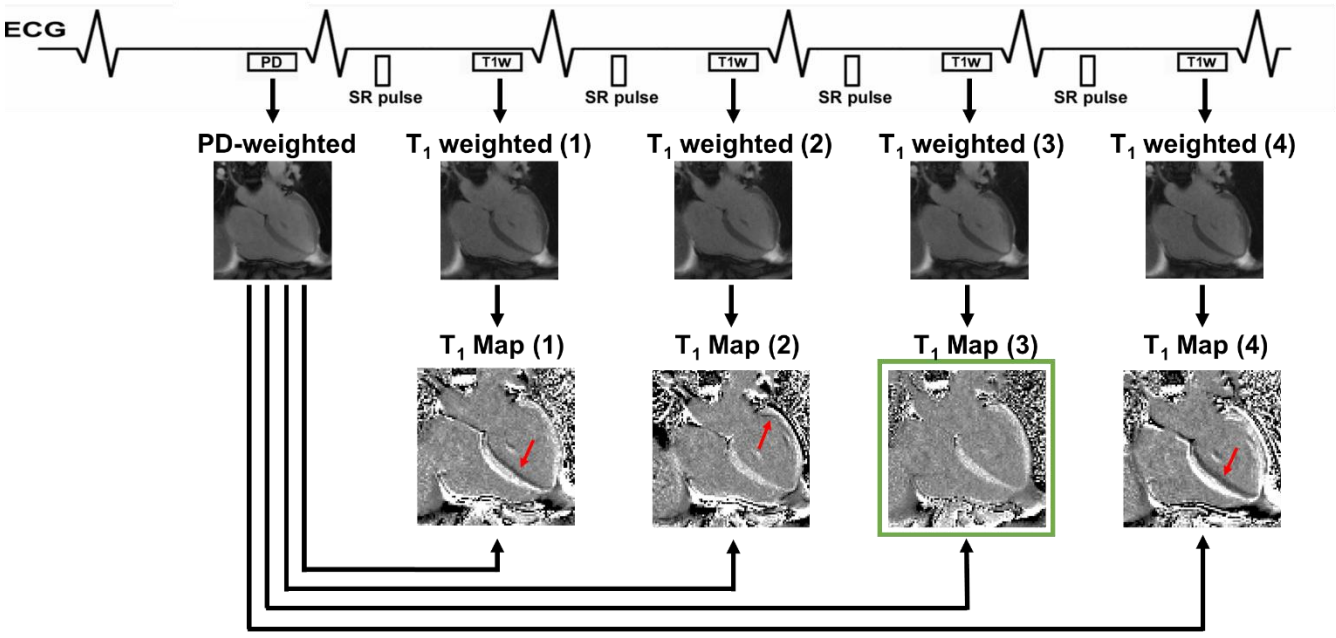

Figure 4.1**:** A schematic diagram illustrating a short (~5 s) breath-hold AIR T_1 mapping acquisition sampling one proton density image (heartbeat 1) and 4 T_1 weighted images (heartbeats 2-5). With this acquisition scheme, one T_1 weighted image among four that best registers to the proton density image (green box) is used for analysis. Red arrows point to mis-registration image artifacts arising from arrhythmia, heart rate variation, and/or respiratory motion. T_1w: T_1 weighted image; PD: proton density weighted image; ECG: electrocardiogram; SR: saturation-recovery.

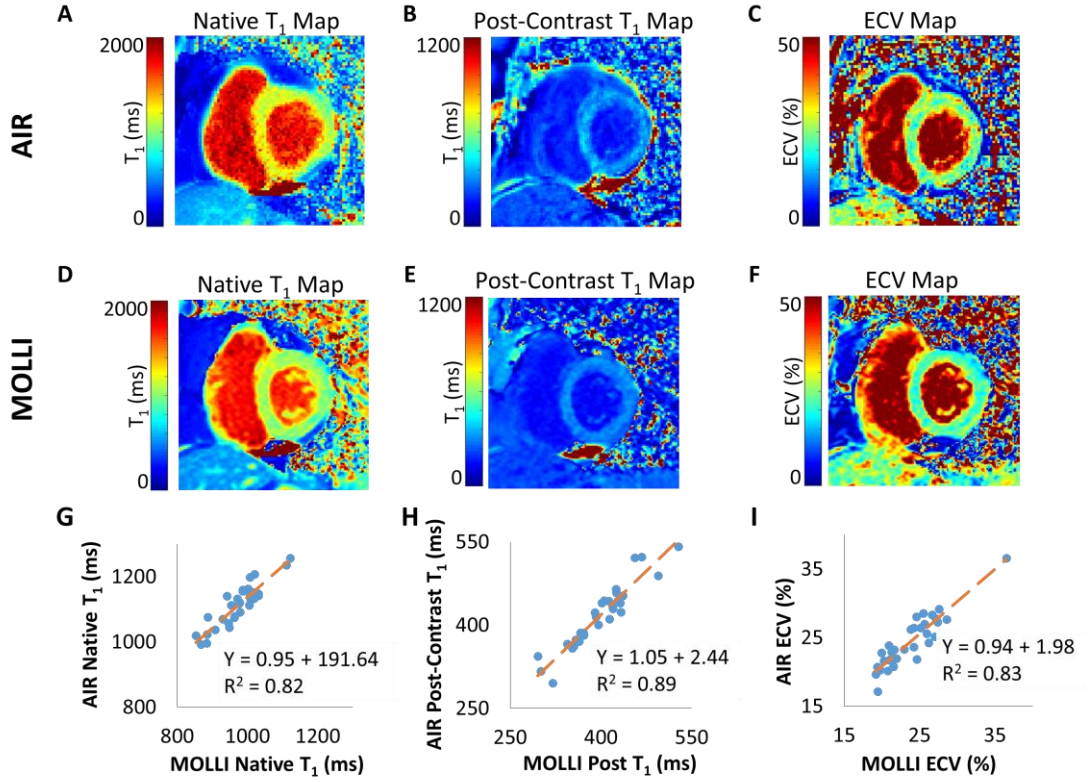

Figure 4.2: Representative native T_1 (left column), post-contrast T_1 (middle column), and ECV (right column) maps of a non-AF patient in sinus rhythm obtained using AIR (row 1) and MOLLI T_1 mapping (row 2). Scatter plots (row 3, from left to right) showing a strong correlation in native myocardial T_1 (R^2 = 0.82, slope = 0.95, bias = 191.64 ms), post-contrast T_1 (R^2 = 0.89, slope = 1.05, bias = 2.44 ms), and ECV (R^2 = 0.83, slope = 0.94, bias = 1.98%). These linear models were used to translate between AIR and MOLLI or vice versa.

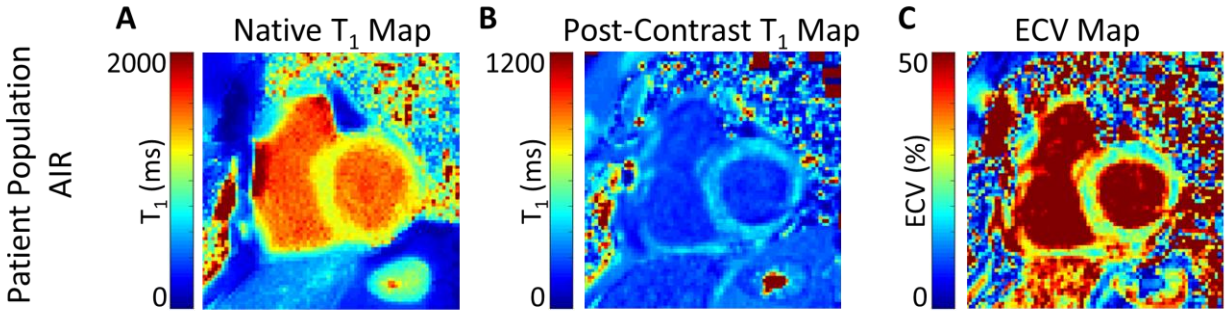

Figure 4.3**:** Representative native T_1, post-contrast T_1, and ECV maps illustrating artifact-free quality produced by AIR cardiac T_1 mapping in patients with AF. (A) Native T_1 map; (B) post-contrast T_1 map; (C) ECV map.

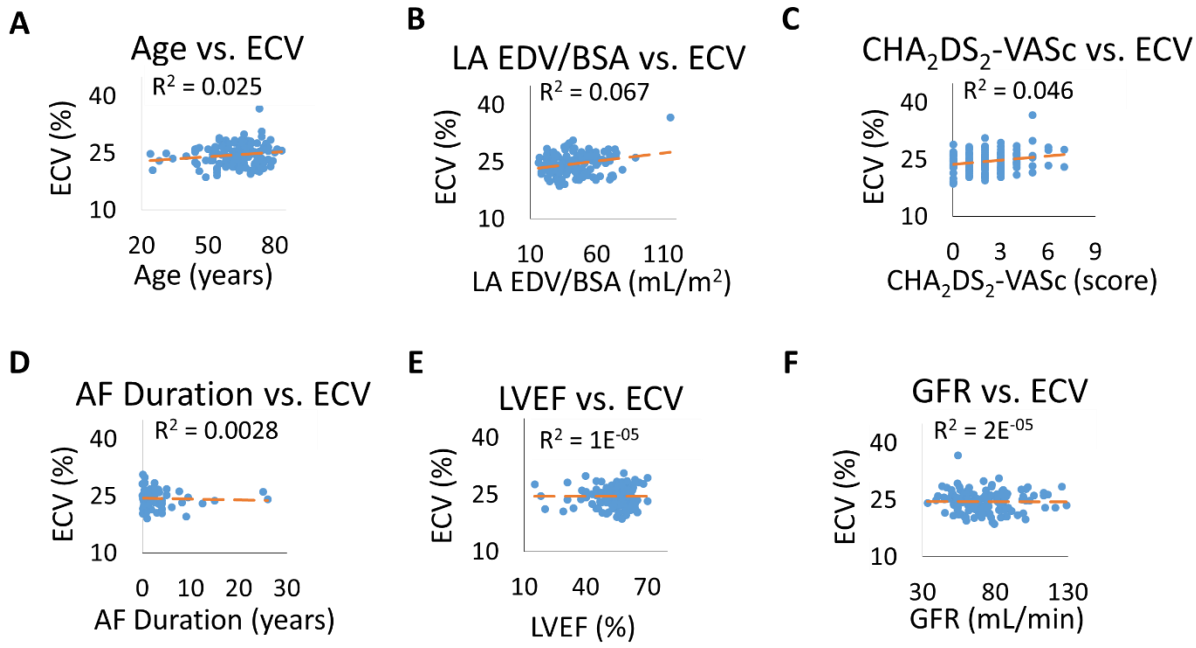

Figure 4.4: Linear regression plots showing lack of association between ECV and the following clinical variables in AF patients: (A) Age (B) LA ESV/BSA, (C) CHA_2DS_2-VASc, (D) AF Duration, (E) LVEF, and (F) GFR.

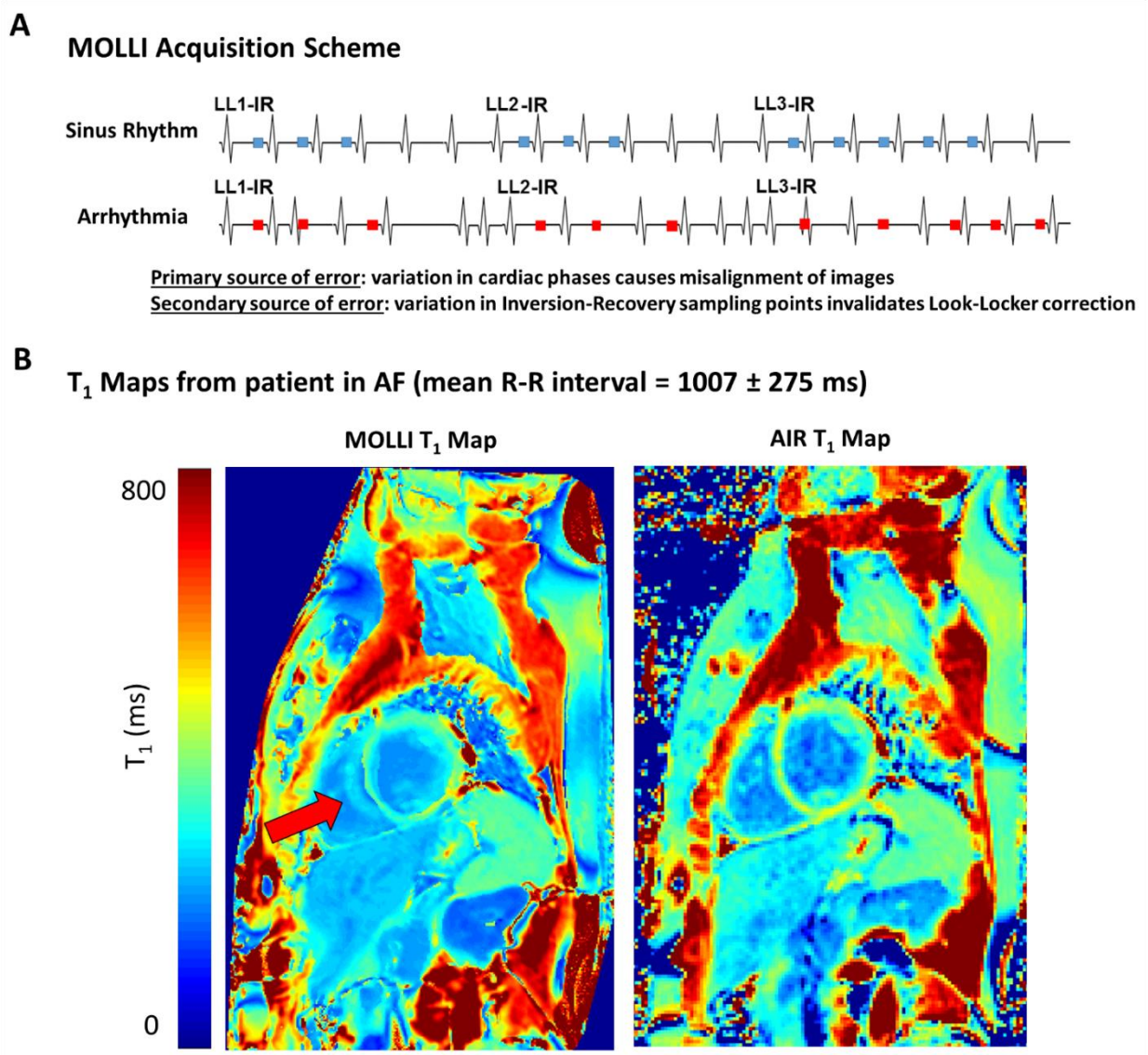

Figure 4.5**:** (A) Schematic illustrating why an inversion-recovery based cardiac T_1 mapping pulse sequence such as conventional MOLLI produces inaccurate results in patients with AF. In patients with sinus rhythm, a 3(3)5 MOLLI pulse sequence samples 8 time points along inversion recovery of magnetization at a fixed cardiac phase (mid diastole). In patients with arrhythmia, the same MOLLI pulse sequence samples 8 time points along inversion recovery of magnetization at different cardiac phases. This inconsistent sampling during arrhythmia causes misalignment of images (major source of error) and confounds the Look-Locker correction (minor source of error). (B) Representative post-contrast T_1 maps of an AF patient (mean R-R interval = 1007 ± 275 ms) comparing sensitivity of the pulse sequence to arrhythmia: MOLLI with mis-registration artifacts (left) and AIR without artifacts (right). Blue and red dots on the ECG traces represent sampled data points for sinus and irregular rhythm, respectively.

5 Left Ventricular Extracellular Volume Expansion does not Predict Recurrence of Atrial Fibrillation following Catheter Ablation

5.1 Introduction

Atrial fibrillation (AF) affects between 2.7 to 6.1 million Americans and is the most prevalent arrhythmia (1). Catheter ablation is the best rhythm control treatment for AF but its success rates are only moderate: 70-80% for paroxysmal AF and < 70% for persistent AF (42, 43). Identifying accurate predictors based on clinical (e.g., AF duration, hypertension, sex, age) and imaging metrics (e.g., left atrial [LA] size, left ventricular [LV] function) for AF recurrence has proven difficult in clinical practice. LA fibrosis has been shown to be the arrhythmogenic substrate for initiating and maintaining AF (45-48, 127). While LA fibrosis as assessed with 3D LA late gadolinium-enhanced (LGE) cardiovascular magnetic resonance (CMR) has shown promise to predict AF recurrence following catheter ablation (128-131), inadequate spatial resolution (~1.5 mm x 1.5 mm x 2.5 mm) of CMR for quantifying fibrosis in the thin (~1-2 mm) LA wall hinders its clinical translation.

One approach to overcoming the technical challenge of imaging the thin LA wall with CMR is to identify surrogate markers in the LV, since there is a complex relationship between the LA and LV in human AF pathophysiology. There are several mechanisms by which AF may impact the LV, including tachycardia (123, 132), atrial-ventricular dyssynchrony (133, 134), lack of atrial contraction (135, 136), functional mitral regurgitation (137, 138), and ventricular fibrosis (139). Given the aforementioned mechanisms, AF-mediated ventricular fibrosis, should it exist, is likely to be diffuse. A recent study by McLellan et al. (140) reported that diffuse LV fibrosis, as

measured with post-contrast cardiac T_1, predicts recurrence of AF following catheter ablation. We contend that the results from this study may have been influenced by the use of post-contrast cardiac T_1 as a marker of diffuse LV fibrosis, since post-contrast T_1 mapping is known to be sensitive to biological confounders such as the gadolinium clearance rate, time of measurement, body composition, and hematocrit and MRI-related confounders such as contrast agent type and dose and static magnetic field strength. To address these confounders, the CMR community has moved towards myocardial extracellular volume (ECV) fraction mapping (108, 117) instead, since, in the absence of myocardial edema, ECV demonstrates best overall agreement with published human histological validation studies (109). In addition, the results from the study by McLellan et al. (140) may have been influenced by use of an inversion-recovery based cardiac T_1 mapping pulse sequence, which is known to be sensitive to rapid heart rate and arrhythmia (89, 114). Due to both these biological and methodological confounders in McLellan et al. (140), another study accounting for the aforementioned confunders is warranted to investigate whether LV ECV expansion predicts recurrence of AF following catheter ablation.

Cardiac T_1 mapping in AF patients is technically challenging because of their irregular heart rhythm. For conventional inversion-recovery based pulse sequences such as Look Locker inversion recovery (MOLLI)(84) and Shortened MOLLI (ShMOLLI)(85) in patients with arrhythmia, multiple T_1-weighted images would be sampled at different cardiac phases, making it difficult for a motion correction algorithm to align the images. In addition to the residual mis-alignment of images due to arrhythmia, beat-to-beat variations in magnetization recovery during arrhythmia will confound the Look-Locker correction for MOLLI and ShMOLLI. The first step to minimizing the sensitivity to arrhythmia is to achieve T_1-weighting with saturation recovery

instead, which is commonly practiced in first-pass perfusion CMR (141). The second step is to require only a single T_1-weighted image for calculating T_1, thereby relaxing the motion correction problem. An arrhythmia-insensitive-rapid (AIR) cardiac T_1 mapping pulse sequence (89) is specifically designed with these two features to achieve insensitivity to arrhythmia; it was previously validated in large animals against histology (112) and evaluated in patients with sinus rhythm to show inferior precision than MOLLI (113).

In this observational study, we sought to overcome the methodological limitation experienced by McLellan et al. (140) and investigate whether LV ECV expansion, regardless of etiology, predicts recurrence of AF following catheter ablation, by accurately measuring ECV (improved metric) using AIR cardiac T_1 mapping (improved method).

5.2 Materials and Methods

Justification for AIR Cardiac T_1 mapping for Patients with AF

At our institution, AIR cardiac T_1 mapping replaced conventional MOLLI (84) T_1 mapping in the routine clinical CMR protocol for patients with AF, because MOLLI is known to produce inaccurate results in arrhythmia (89, 114).

Study Population

We identified 268 consecutive patients who underwent a pre-ablation clinical CMR at Northwestern Memorial Hospital from January 2017 to December 2018. The need for informed

consent was waived. A retrospective study was approved by our Institutional Review Board (IRB) and was found to comply with the Health Insurance Portability and Accountability Act (HIPAA). 75 patients were excluded for not having AIR cardiac T_1 mapping; 10 were excluded for being imaged on a 3 Tesla scanner; 7 patients were excluded because they did not have follow-up rhythm status records available at our hospital; 38 patients were excluded because they had previously undergone an ablation procedure; 34 patients were excluded because they underwent radio-frequency (RF) ablation; 4 patients were excluded because they did not undergo an ablation procedure. Patients who did not undergo ablation had several reasons including having a thrombus in their left atrial appendage, a low hemoglobin level, or electing to continue antiarrhythmic drug treatment (amiodarone or tikosyn) instead of undergoing cathether ablation.

Patients with a history of coronary artery disease (CAD) was defined as significant coronary stenosis (left main >50% or major epicardial stenosis >70%) (142), a history of coronary revascularization, or prior myocardial infarction (MI); severe left ventricular hypertrophy (LVH) was defined as wall thickness > 1.5 cm (143). Each condition was determined based on clinical chart review. We included all eligible patients, regardless of clinical history, except for those with a previous ablation procedure, as mentioned above.

MRI

CMR was performed on three 1.5 Tesla whole-body MRI scanners (MAGNETOM Aera & Avanto, Siemens Healthineers, Erlangen, Germany) equipped with a gradient system capable of achieving a maximum gradient strength of 45 mT/m and a slew rate of 200 T/m/s. Imaging was

performed with body matrix and spine array coils with 18 and 32 coil elements on the Avanto and Aera, respectively.

The relevant imaging parameters for AIR cardiac T_1 mapping with balanced steady-state free precession readout are as follows: field of view = 400 mm x 300 mm, image acquisition matrix size = 192 x 144 (phase-encoding), spatial resolution = 2.1 mm x 2.1 mm, slice thickness = 8 mm, echo time (TE) = 1.1 ms, repetition time (TR) = 2.7 ms, receiver bandwidth = 930 Hz/pixel, flip angle = 55^o, generalized autocalibrating partially parallel acquisitions (GRAPPA)(59) acceleration factor = 1.8, ECG triggering, linear k-space ordering, saturation-recovery time to center of k-space (TS) = 600 ms for native and 300 ms for post-contrast. The breath-hold duration (scan time) was 5 heart beats (one proton density weighted image during heart beat 1, 4 T_1-weighted images during heart beats 2-5) per plane. This acquisition scheme enabled us to account for arrhythmia or respiratory motion by choosing one among 4 T_1-weighted images that best registers with the proton density weighted image upon visual inspection. For each subject, we performed AIR cardiac T_1 mapping in two short-axis planes (base, mid) and one long-axis (4-chamber) plane. The apical short-axis plane was excluded due to its susceptibility to partial volume averaging around the endocardial border. Each patient received either 0.15 or 0.20 mmol/kg of gadobutrol (Gadavist, Bayer HealthCare Whippany, USA) via a power injector as part of the clinical protocol, depending whether the estimated glomerular filtrate rate (eGFR) was 45-59 or > 60 mL/min per 1.73 m^2, respectively. Post-contrast T_1 mapping was performed between 10-15 minutes after administration of gadobutrol, immediately after the clinical LGE scans.

Image Analysis

For assessment of LV ECV, first reader (SG, with 3 years of experience analyzing ECV and cardiac MRI) and second reader (LF, with 2 years of experience analyzing ECV and cardiac MRI) independently analyzed native T_1 and ECV maps, where ECV was calculated using the native and post-contrast T_1, the difference in blood T_1 based on contours of LV cavity, and the patient's hematocrit, taken from the day of CMR scan, as per SCMR consensus statement (108, 117). The mean native T_1 and ECV values were calculated after manually drawing the endo- and epicardial contours. Using clinical LGE images covering the whole heart as a guide to determine areas of focal fibrosis, ROI for analysis were drawn only in areas without any focal fibrosis (e.g. myocardial infarction), since the focus of this study is LV ECV. The contour segmentation was performed using a customized tool developed in Matlab (R2017, The Mathworks Inc, Natick, MA, USA). Normal native myocardial T_1 was defined as $\leq$ 1233.7 ms, and normal ECV was defined as $\leq$ 32.8%. These cut points were calculated by the following process. In step 1, we calculated two standard deviations above the norm of native T_1 (1102 ms) and ECV values (32.7%) derived from a prior study of 94 healthy volunteers (mean age = 50 ± 14 years; 49 males and 45 females) scanned with MOLLI cardiac T_1 mapping (116). In step 2, we applied linear models for converting MOLLI to AIR, as previously described (144). Presence of LGE were determined by the clinical radiology report. For estimating cardiac rhythm, the coefficient of variation of the R-R interval was used from a representative cine image set for each patient.

For assessment of LA end diastolic volume/body surface area (LA EDV/BSA), the first reader (SG) used CVI[42] (Circle Cardiovascular Imaging Inc., Calgary, AB, Canada) to calculate maximum LA volume based on the area-length method (118), and BSA as determined based on

the Mosteller formula. Normal LA EDV/BSA values were considered to be males ≤ 52.4 mL/m^2, females ≤ 53.4 mL/m^2 (119).

Catheter Ablation

All 100 patients underwent cryoballoon ablation (CB) (Artic Front Advance^{TM}, Medtronic, Minneapolis, MN). Standard procedures were used, including use of intracardiac echocardiography (AcuNav, Biosense Webster), fluoroscopy, and electroanatomic mapping (NavX, Abbott, and CARTO, Biosense Webster). Briefly, for CB, a minimum of two cryoablations were delivered per pulmonary vein (PV) with ablation lasting 3-4 minutes to a nadir temperature < 55°C. If PV isolation (PVI) was not achieved with CB, then focal ablation was performed using either cryocatheter (Cryocath, Medtronic) or radiofrequency catheter to achieve PVI. Entry block was confirmed by pacing from the distal poles of the coronary sinus catheter for the left sided PVs and elimination of right sided PVs. Exit block in all PVs was evaluated by pacing around the circular mapping catheter placed sequentially in each PV.

Rhythm Status following CB

Recurrence of AF was determined after a 3-month blanking period. A patient was classified as having a successful ablation if there was no recurrence of AF documented on medical chart review. AF recurrence was defined as any episodes of AF > 30 seconds off antiarrhythmic drugs.

Rhythm status was determined using routine ECGs, Holter monitoring, or Zio patch monitoring (iRhythm Technologies, Inc, San Francisco, CA, USA) at multiple clinic visits.

Statistical Analysis

We used average readers' results for statistical analysis. Continuous variables were compared using a two-tailed, two-sample t-tests while categorical variables were compared using a two-tailed Fisher's exact test. AF recurrence was modeled using Cox Regression analysis; univariate predictors with a statistical significance were entered into a multivariate stepwise regression model. P-values < 0.05 were considered statistically significant for all analyses. Statistical analyses were performed using IBM SPSS Statistics for Windows (Version 23.0. Armonk, NY: IBM Corp.

5.3 Results

Baseline Clinical and CMR Variables

In total, we studied 100 patients (mean age = 62 ± 11 years, 79 males and 31 females, 67 (67%) paroxysmal AF) who underwent cryoballoon ablation. The mean coefficient of variation in the R-R interval during CMR for all patients was 10 ± 10.4%. Table 5.1 lists patient characteristics for our cohort. For characteristics with at least 10 samples, significant differences were found for age, CHA_2DS_2-VASc, and number of cardioversions. Table 5.2 summarizes the CMR findings for our patient cohort. Both LA EDV/BSA (males ≤ 52.4 mL/m^2, females ≤ 53.4 mL/m^2) and ECV ($\leq$

32.8%) was within the normal range for all AF groups, but both metrics were significantly ($p < 0.001$) higher for peAF than pAF. In our cohort, only 1 patient had ECV > 32.7%, and ECV ranged from 17.3 to 37.1%. While LVEF was within the normal range for all AF groups, it was significantly lower for peAF (48.8 ± 12.1%) than pAF (57.4 ± 7.9%). Focal fibrosis (as assessed with LGE CMR) was detected in 29 of patients, and there was no significant difference between the pAF and peAF groups.

Clinical and CMR Variables: Ablation Success vs. Failure

During an average follow-up period of 457 ± 261 days with 4 ± 3 rhythm checks per patient, 72 (72%) patients maintained sinus rhythm. While the success rate was higher in pAF patients (75%) than peAF patients (67%) (Table 5.1), the difference was not significantly different ($p = 0.48$). According to the two-sample t-test and Fisher's exact test comparing patients with and without recurrence of AF, none of the variables were significantly different except for age ($p = 0.22$) (Tables 5.3 and 5.4). According to the Cox regression model, none of the variables predicted AF recurrence in all patients (Table 5.5), pAF subgroup (Table 5.6), peAF subgroup (Table 5.7), or all patients without LGE (Table 5.8).

5.4 Discussion

The main finding of our study is that neither LV ECV expansion measured using AIR cardiac T_1 mapping nor other imaging metrics (see Table 5.4) predict recurrence of AF following

catheter ablation. In our cohort of 100 patients, 72% of patients maintained sinus rhythm following catheter ablation, which is consistent with published success rates (42, 43, 145-148).

Our study contradicts the findings by McLellan et. al. who reported that diffuse LV fibrosis as measured with post-contrast T_1 predicts maintenance of sinus rhythm following catheter ablation (140). This discrepancy might be due to differences in patient population; our patients had less AF burden (shorter AF history and smaller LA volume) but higher co-morbidities (higher body mass index (BMI) and CHA_2DS_2-VASc). This discrepancy might be due to sensitivity of post-contrast cardiac T_1 mapping to confounders, including but not limited to renal function, type of contrast agent, and delaying time, and sensitivity of inversion-recovery based cardiac T_1 mapping to arrhythmia. In contrast, ECV measured with AIR cardiac T_1 mapping is insensitive to arrhythmia and the aforementioned confounders.

Our results also are inconsistent with the findings – LGE predicts AF recurrence - reported by Suksaranjit et. al. (149). In our patient population, the ablation success rate was similar between with (71%) and without (72%) LGE. The discrepancy might be due to differences in patient population (29% of our patients had positive LGE, of these positive LGE patients 20.7% was associated with CAD; 6.5% of their patients had positive LGE, of these positive LGE patients 46% was associated with CAD) and ablation modality (our cohort received cryoballoon ablation; their cohort received RF ablation).

Our findings have important clinical implications. First, while there is a complex relationship between the LA and LV in AF, it is likely that AF-mediated cardiomyopathy is a reversible condition (123) and not associated with diffuse LV fibrosis. While one prior study of a

canine model with AF (3 months) reported the prevalence of diffuse LV fibrosis (139), another prior study of canine model with chronic AF (up to 22 months) contradicted that study and reported the absence of diffuse LV fibrosis (112). Our recent clinical study showed that LV ECV expansion is not associated with AF (144). Findings from this study agree with findings by Koopmann et al. (112) and Gunasekaran et al. (144). Second, LA fibrosis is the arrhythmogenic substrate for AF (45-48, 127) and, thus, a better candidate for predicting AF recurrence following AF ablation. While it may have seemed like a plausible idea to overcome the technical challenge of imaging LA fibrosis with CMR by imaging LV ECV expansion as a surrogate predictor, our data suggest otherwise. Despite the technical difficulty, it is pathophysiologically more plausible to quantify LA fibrosis (i.e. substrate) using 3D LGE CMR for predicting AF recurrence (128-131). For wider clinical translation, it may be necessary to develop advanced 3D LA LGE CMR methods with higher spatial resolution, signal-to-noise ratio, and scanning efficiency, which may be possible by data acceleration techniques like extra motion-state Golden-angle Radial Sparse Parallel (XD-GRASP) (65) or higher magnetic field strength ($\geq$ 3 Tesla).

This study has several limitations that warrant discussion. First, our sample size is relatively small with only 100 patients, but it is on par with 103 patients studied by McLellan et al. (140). A future study of a large AF cohort is warranted to adjust for confounders and test whether LV ECV expansion predicts AF recurrence following AF ablation. Second, post-ablation rhythm status checks were made clinically using a mixture of modalities (ECG, Holter monitor, and ZIO monitor) at multiple time points. However, we used all available rhythm status records, and any documentation of AF following the 3-month blanking period was defined as recurrence. Third, our patient population undergoing AF ablation at the Northwestern Memorial hospital had

fewer women than men and fewer minorities (Blacks, Hispanics, or Asians) than Whites. Thus, it remains unclear whether the results from this study reflect AF pathophysiology in the general population. Fourth, LV ECV expansion was assessed from T_1 maps in 3 cardiac planes. While this approach is plausible for assessing LV ECV expansion, we acknowledge that 3 cardiac planes do not adequately reflect the whole heart. Fifth, success rates reported in this study reflects variations due to differences in skill level among ablationists. Sixth, this study did not conduct a head-to-head comparison between inversion-recovery based cardiac T_1 mapping used in McLellan et al. (140) and our AIR cardiac T_1 mapping. Inversion-based cardiac T_1 mapping pulse sequences are known to be sensitive to rapid heart rate and arrhythmia (89, 114). In contrast, our AIR cardiac T_1 mapping pulse sequence is insensitive to arrhythmia because it uses saturation-recovery and only two (one proton density and one T_1 weighted) images are needed to produce a T_1 map. A future study is warranted to compare the sensitivity of both cardiac T_1 mapping pulse sequences, particularly in a large cohort, since as our study included only 100 patients and McLellan et al. (140) included only 103 patients.

In summary, neither diffuse LV fibrosis nor other image metrics (see Tables 5.4 and 5.5) predicted recurrence of AF following catheter ablation in our patient cohort. Thus, diffuse LV fibrosis, as measured by ECV, is likely a poor predictor of AF recurrence following cryoballoon ablation.

Table 5.1: Baseline patient characteristics and ablation success outcome comparisons based on AF types (paroxysmal vs. persistent). P-values were omitted for characteristics less than 10 samples.

	All (n = 100)	Paroxysmal (n = 67)	Persistent (n = 33)	P Value
Age (years)	62 ± 11	60 ± 12	65 ± 9	0.04*
Sex				
M	69 (69)	46 (69)	23 (70)	>0.99
F	31 (31)	21 (31)	10 (30)	
BMI	29.0 ± 5.94	28.8 ± 5.6	29.4 ± 6.2	0.62
Race				
White	96 (96)	63 (94)	33 (100)	0.30
African American	1 (1)	1 (2)	0 (0)	
Asian	2 (2)	2 (3)	0 (0)	
Hispanic	1 (1)	1 (2)	0 (0)	
CHA_2DS_2-VASc Score	2.1 ± 1.6	1.8 ± 1.5	2.7 ± 1.7	0.005*
AF duration (y)	2.9 ± 4.4	3.1 ± 4.6	2.5 ± 3.8	0.57
Previous Cardioversion	0.9± 1.2	0.6 ± 1.2	1.5 ± 1.2	< 0.001*
GFR (mL/min)	72.6 ± 20.1	73.9 ± 20.3	70.1 ± 19.6	0.34

Diabetes	11 (11)	7 (10)	4 (12)	
Hypertension	52 (52)	34 (51)	18 (55)	0.83
On ACE Inhibitor	17 (17)	12 (18)	5 (15)	>0.99
On ARB	14 (14)	10 (15)	4 (12)	>0.99
Coronary Artery Disease	15 (15)	7 (10)	8 (24)	0.08
Prior MI	8 (8)	3 (4)	5 (15)	
Prior stent	7 (7)	5 (8)	2 (6)	
Prior CABG	3 (3)	0 (0)	3 (9)	
Severe LVH (≥ 15 mm)	7 (7)	5 (8)	2 (6)	
Heart Failure	8 (8)	2 (3)	6 (18)	
Prior Stroke	9 (9)	5 (8)	4 (12)	
Ablation Success	72 (72)	50 (75)	22 (67)	0.48

BMI: body mass index, AF: atrial fibrillation, GFR: glomerular filtration rate, ACE: angiotensin-converting enzyme, ARB: angiotensin receptor blocker, MI: myocardial infarction, CABG: coronary artery bypass graft, LVH: left ventricular hypertrophy

Table 5.2: Baseline CMR metrics comparisons based on AF type (paroxysmal vs. persistent). P-values were omitted for characteristics less than 10 samples.

	All (n = 100)	Paroxysmal (n = 67)	Persistent (n = 33)	P Value
LVEF (%)	54.6 ± 10.3	57.4 ± 7.9	48.8 ± 12.1	< 0.001*
LA EDV/BSA (mL/m^2)	42.7 ± 16.2	38.4 ± 14.6	47.8 ± 16.0	< 0.001*
Positive LGE	29 (29)	21 (31)	8(24)	0.49
Vascular	6 (6)	4 (6)	2 (6)	
ECV	25.0 ± 3.4	24.5 ± 3.1	26.1 ± 3.7	0.03*
Native Myocardial T_1	1087.2 ± 87.5	1080.7 ± 92.8	1100.3 ± 75.3	0.29

LVEF: left ventricular ejection fraction, LA EDV/BSA: left atrial end diastolic volume/body surface area, LGE: late gadolinium enhancement, ECV: extracellular volume fraction

Table 5.3: Patient characteristics comparisons based on rhythm status following catheter ablation. P-values were omitted for characteristics less than 10 samples.

	Maintained Sinus Rhythm (n = 72)	AF Recurrence (n = 28)	P Value
Age (years)	60 ± 12	66 ± 9	0.022*
Sex			
M	49 (68)	20 (71)	0.81
F	23 (32)	8 (29)	
BMI	29.1 ± 5.7	28.6 ± 6.6	0.69
Race			
White	68 (94)	28 (100)	0.57
African American	1 (1)	0 (0)	
Asian	2 (3)	0 (0)	
Hispanic	1 (1)	0 (0)	
CHA_2DS_2-VASc Score	2.0 ± 1.7	2.3 ± 1.5	0.48
AF Type			
Paroxysmal	50 (69)	17 (61)	0.47
Persistent	22 (31)	11 (39)	

AF Duration (y)	3.0 ± 4.8	2.7 ± 2.9	0.81
Previous Cardioversion	0.8 ± 1.3	1.0 ± 1.0	0.57
GFR (mL/min)	74.2 ± 20.4	68.5 ± 18.9	0.20
Diabetes	9 (13)	2 (7)	
Hypertension	33 (46)	19 (68)	0.074
On ACE Inhibitor	13 (18)	4 (14)	0.77
On ARB	9 (13)	5 (18)	
Coronary Artery Disease	10 (14)	5 (18)	0.76
Prior MI	5 (7)	3 (11)	
Prior stent	4 (6)	3 (11)	
Prior CABG	3 (4)	0 (0)	
Severe LVH (≥ 15 mm)	4 (6)	3 (11)	
Heart Failure	4 (6)	4 (14)	
Prior Stroke	7 (10)	2 (7)	

BMI: body mass index, AF: atrial fibrillation, GFR: glomerular filtration rate, ACE: angiotensin-converting enzyme, ARB: angiotensin receptor blocker, MI: myocardial infarction, CABG: coronary artery bypass graft, LVH: left ventricular hypertrophy

Table 5.4: CMR metrics comparisons based on rhythm status following catheter ablation. P-values were omitted for characteristics less than 10 samples.

	Maintained Sinus Rhythm (n = 72)	AF Recurrence (n = 28)	P Value
LVEF (%)	54.1 ± 11.2	55.7 ± 7.1	0.49
LA EDV/BSA (mL/m^2)	42.4 ± 14.8	43.4 ± 19.6	0.77
Positive LGE	21 (29)	8 (29)	>0.99
Vascular	4 (6)	2 (7)	
ECV	25.1 ± 3.3	24.7 ± 3.7	0.57
Native Myocardial T_1	1093.8 ± 73.5	1070.2 ± 115.9	0.23

LVEF: left ventricular ejection fraction, LA EDV/BSA: left atrial end diastolic volume/body surface area, LGE: late gadolinium enhancement, ECV: extracellular volume fraction

Table 5.5: Cox regression analysis for predicting recurrence of AF following catheter ablation.

Variable	Hazard Ratio (HR)	95.0% CI for HR Lower	Upper	P Value
Age	1.037	0.995	1.080	0.086
Previous Cardioversion	1.104	0.789	1.369	0.783
AF Type	1.171	0.548	2.504	0.683
AF Duration	0.986	0.901	1.080	0.764
LGE	0.954	0.419	2.172	0.911
Vascular LGE	0.729	0.171	3.099	0.668
LA EDV/BSA	1.009	0.986	1.032	0.466
LVEF	1.017	0.982	1.053	0.355
CHA_2DS_2-VASc	0.965	0.762	1.223	0.769
ECV	0.964	0.857	1.085	0.548
Native Myocardial T_1	0.998	0.995	1.002	0.376

The hazard ratio reflects the Cox proportional hazard ratio of AF recurrence. AF: atrial fibrillation, LGE: late gadolinium enhancement, LA EDV/BSA: left atrial end diastolic volume/body surface area, LVEF: left ventricular ejection fraction, ECV: extracellular volume fraction

Table 5.6: Cox regression analysis for predicting recurrence of AF following catheter ablation in patients with paroxysmal AF (n = 67).

Variable	Hazard Ratio (HR)	95.0% CI for HR Lower	Upper	P Value
Age	1.051	0.992	1.113	0.092
Previous Cardioversion	1.029	0.705	1.503	0.881
AF Duration	1.007	0.914	1.108	0.894
LGE	1.542	0.584	4.072	0.382
Vascular LGE	1.227	0.276	5.456	0.788
LA EDV/BSA	1.002	0.968	1.037	0.923
LVEF	0.995	0.941	1.051	0.852
CHA_2DS_2-VASc	1.108	0.825	1.487	0.497
ECV	0.940	0.798	1.108	0.463
Native Myocardial T_1	0.998	0.994	1.002	0.242

The hazard ratio reflects the Cox proportional hazard ratio of AF recurrence. AF: atrial fibrillation, LGE: late gadolinium enhancement, LA EDV/BSA: left atrial end diastolic volume/body surface area, LVEF: left ventricular ejection fraction, ECV: extracellular volume fraction

Table 5.7: Cox regression analysis for predicting recurrence of AF following catheter ablation in patients with persistent AF (n = 33).

Variable	Hazard Ratio (HR)	95.0% CI for HR Lower	Upper	P Value
Age	1.016	0.952	1.085	0.633
Previous Cardioversion	1.012	0.613	1.671	0.962
AF Duration	0.922	0.738	1.153	0.477
LGE	0.269	0.034	2.112	0.212
Vascular LGE	0.969	0.884	1.062	0.500
LA EDV/BSA	1.017	0.979	1.055	0.386
LVEF	1.049	0.994	1.107	0.084
CHA_2DS_2-VASc	0.716	0.464	1.105	0.131
ECV	0.976	0.816	1.167	0.789
Native Myocardial T_1	1.000	0.992	1.009	0.941

The hazard ratio reflects the Cox proportional hazard ratio of AF recurrence. AF: atrial fibrillation, LGE: late gadolinium enhancement, LA EDV/BSA: left atrial end diastolic volume/body surface area, LVEF: left ventricular ejection fraction, ECV: extracellular volume fraction

Table 5.8: Cox regression analysis for predicting recurrence of AF following catheter ablation in patients without LGE (n = 71).

Variable	Hazard Ratio (HR)	95.0% CI for HR Lower	Upper	P Value
Age	1.040	0.994	1.088	0.089
Previous Cardioversion	1.063	0.797	1.418	0.677
AF Type	1.731	0.720	4.162	0.220
AF Duration	0.999	0.884	1.130	0.990
LA EDV/BSA	1.027	0.999	1.055	0.059
LVEF	1.013	0.968	1.059	0.581
CHA_2DS_2-VASc	0.936	0.703	1.246	0.817
ECV	0.984	0.857	1.129	0.817
Native Myocardial T_1	0.997	0.992	1.003	0.341

The hazard ratio reflects the Cox proportional hazard ratio of AF recurrence. AF: atrial fibrillation, LGE: late gadolinium enhancement, LA EDV/BSA: left atrial end diastolic volume/body surface area, LVEF: left ventricular ejection fraction, ECV: extracellular volume fraction

6 Accelerated 3D Left Atrial Late Gadolinium-Enhanced Cardiovascular Magnetic Resonance with stack-of-stars k-space sampling, b-SSFP readout, and XD-GRASP reconstruction for Quantification of Left Atrial Fibrosis in Patients with Atrial Fibrillation at 1.5 Tesla

6.1 Introduction

Atrial fibrillation (AF) is the most common sustained arrhythmia in adults in the US (103). Catheter ablation is superior to antiarrhythmic drugs for rhythm control treatment for AF but success rates to date are still moderate: 70-80% for paroxysmal AF and < 70% for persistent AF (42, 43). Identifying accurate predictors for AF recurrence based on clinical (e.g. AF duration) and imaging metrics (e.g., left atrial [LA] size, left ventricular [LV] function) has proven difficult. Evidence suggests that LA fibrosis is the arrhythmogenic substrate for initiating and maintaining AF in some individuals (45-48). Thus, LA fibrosis is a plausible predictor of AF recurrence following catheter ablation. While myocardial biopsy is the gold standard test for myocardial fibrosis, it is rarely indicated due to procedural risk and sampling errors, particularly for the thin LA. Thus, there is a need to identify a non-invasive method for measuring LA fibrosis for predicting AF recurrence following catheter ablation.

A practical approach is to perform non-invasive imaging of myocardial fibrosis using late gadolinium-enhanced (LGE) cardiovascular magnetic resonance (CMR)(150). Indeed, LA fibrosis as assessed with 3D LA LGE CMR (151) has shown promise in predicting AF recurrence following catheter ablation (129, 131). However, current 3D LA LGE CMR has several technical limitations: (a) inadequate spatial resolution (~1.5 mm x 1.5 mm x 2.5 to 4 mm) makes it challenging to quantify fibrosis in the thin (~2 mm) LA wall (129, 152) with a high degree of

reproducibility; (b) navigator gating for tracking respiratory motion is typically 40% efficient and prolongs scanning in patients with irregular breathing patterns, leading to lengthy scan times (~10-15 min)(153). Moreover, image quality produced by 3D LA LGE CMR tends to be suboptimal at 1.5 Tesla, which represents the highest market share of clinical MRI scanners in US hospitals. Thus, there is a need to advance 3D LA LGE CMR at 1.5 Tesla for wider acceptance in routine clinical practice.

We sought to address this need by advancing 3D LA LGE CMR to achieve clinically acceptable image quality with high spatial resolution (1.5 mm x 1.5 mm x 2 mm) and predictable scan time (~6 min) at 1.5 Tesla, using stack-of-stars k-space sampling, balanced steady-state free precession (b-SSFP) readout, and extra motion-state Golden-angle Radial Sparse Parallel MRI (XD-GRASP)(65). The purpose of this study is to develop the proposed 3D LA LGE CMR pulse sequence and reconstruction methods and evaluate whether their combination produces clinically acceptable image quality with 1.5 mm x 1.5 mm x 2 mm spatial resolution for quantification of LA fibrosis in AF patients at 1.5 Tesla.

6.2 Materials and Methods

Patients

We prospectively enrolled 20 patients (11 males, 9 females, mean age = 63 ± 6 years, 15 paroxysmal and 5 persistent AF) undergoing a clinically indicated pre-ablation CMR with a standard dose of gadobutrol (Gadavist, Bayer HealthCare Pharmaceuticals, Whippany, NJ). Our 3D LA LGE CMR scans were conducted immediately after the clinical multi-slice 2D LGE

scans, without administering additional gadobutrol (see below for more details on image parameters). This study was conducted in accordance with protocols approved by our institutional review board and was Health Insurance Portability and Accountability Act compliant; all subjects provided written informed consent in writing. See Table 1 for relevant clinical profiles.

MRI Hardware

MRI examinations were conducted on two 1.5T whole-body MRI scanners (MAGNETOM Aera and Avanto, Siemens Healthcare, Erlangen, Germany) equipped with a gradient system capable of achieving a maximum gradient strength of 45 mT/m and a maximum slew rate of 200 T/m/s. The radio-frequency excitation was performed with the body coil, and the signal reception was made with the body matrix and spine coil arrays (~18 elements for Avanto and ~30 elements for Aera).

Pulse Sequence

Stack-of-Stars k-space Sampling

As shown in Figure 6.1A, we designed an inversion-recovery 3D b-SSFP pulse sequence to acquire 48 rays per heartbeat during diastole, immediately before the p-wave (i.e. atrial kick) of ECG. We elected to use a stack-of-starts k-space sampling pattern to efficiently sample the left side of the heart including the LA and pulmonary veins in an oblique sagittal plane with 96

mm field-of-view (FOV) along the partition encoding (kz) direction (Figure 6.1B). As shown in Figure 6.1C, k-space ordering is “winding stair-case” like along kz, where rays are rotated by tiny golden angle (TGA) = 23.6281° (55). Between successive heartbeats, the stair-case pattern is rotated along heartbeats by golden angle (GA) = 111.2461°. Because k-space ordering along kz is linear and all 48 kz lines are acquired per heartbeat, a unique inversion time (TI) samples the center of k-space, which is ideal for inversion-recovery based LGE CMR. Immediately before readout for each heartbeat, we sampled two rays for self-navigation of respiratory motion (Figure 6.1A), as previously described (154). The two navigator rays were oriented with in-plane rotation = 0° and 90° corresponding to the head-to-foot and oblique anterior-to-posterior directions, respectively. We elected to include two navigator rays to account for an operator error, but only the navigator ray oriented along the head-to-foot direction was used for respiratory motion tracking.

Imaging Parameters

As per CMR clinical routine, single-shot, multi-slice 2D LGE sequence was performed during free breathing, including in 2-chamber views, approximately 10 min after administration of 0.15-0.2 mmol/kg of gadobutrol with typical spatial resolution = 2.0 mm x 2.0 mm x 6 mm. Immediately after clinical LGE scans, approximately 15 min after administration of gadobutrol, we performed 3D LA LGE CMR using the following parameters: image acquisition matrix size = 192 × 192 × 48, FOV = 288 mm × 288 mm × 96 mm, spatial resolution = 1.5 mm × 1.5 mm × 2 mm, receiver bandwidth = 704 Hz/pixel, flip angle = 40°, TE/TR = 1.8/3.5 ms, TI to null the

normal myocardium = 220-350 ms, 50 rays (48 for data + 2 for navigator) acquired per heartbeat, ECG triggering every heartbeat, readout duration per heartbeat = 168 ms, and scan time = 350 heartbeats. Optimal TI was determined visually based on images obtained using a TI scout sequence (155) ran with ECG triggering every heartbeat.

Image Reconstruction

Figure 6.2 shows the XD-GRASP image reconstruction pipeline used in this study. Image reconstruction was performed off-line on a workstation (Tesla Xeon E5-2600 V2 256 GB memory, Intel, Santa Clara, California, USA) equipped with Matlab (R2018A, The MathWorks, Inc, Natick, Massachusetts) running on Windows 7 (Microsoft, Redmond, Washington). Prior to XD-GRASP reconstruction, we performed gradient trajectory delay correction while assuming identical gradient shifts around 360° (see Figure 6.7 which summarizes the incremental improvement in artifact suppression following trajectory correction). To accelerate the reconstruction time, we applied coil compression using principal component analysis (PCA)(156) to reduce the coil number to 8. For general details on self-navigation of respiratory motion into six respiratory frames and XD-GRASP reconstruction, see reference (154). Reconstruction parameters that are specific for this project include: temporal finite difference and temporal PCA as two orthogonal sparsifying transforms; the corresponding normalized regularization weight was 0.00015 and 0.0001, respectively; these parameters were determined empirically based on visual inspection of training data, as previously described (157).

Empirical Determination of Acceleration Factor

To determine an optimal acceleration factor, we scanned the first 3 patients for 500 heartbeats and performed XD-GRASP reconstruction at different numbers of heartbeats (250-500, 50 steps), with 500 heartbeats serving as the reference. This retrospective binning of data was made possible with use of golden angle sequence (i.e. irrational angles), since no ray is ever repeated. We computed the normalized root-means-square error (RMSE) and structural similarity index (SSIM)(158) relative to the 500 heartbeats reference, where acceptable is defined as RMSE < 5% and SSIM > 0.9. As shown in Figure 6.8, 350 heartbeats were determined as the shortest duration that produces RMSE < 5% and SSIM > 0.9. As such, we scanned the remaining patients for 350 heartbeats. This corresponds to 2800 rays per respiratory frame, which translates to an acceleration factor (R) 3.3 relative to an equivalent Cartesian scan with 192 x 192 x 48 acquisition matrix and 100% navigator gating efficiency.

Post-Processing Filter for Removal of Residual Aliasing Artifacts and Noise

We applied a 3D block matching (BM3D)(159) filter with an image fidelity term to each individual 2D plane with 30 iterations using a gradient descent with a step size of 0.02 for BM3D, a fidelity weight of 0.01, and a threshold of 0.0004, in order to suppress residual aliasing artifacts while maintaining edge sharpness (see Figure 6.3 which illustrates how BM3D filtering [~4 min] is used during post-processing). For quantitative evaluation, we computed coefficient of variation (CV) of LA blood pool and blood-to-myocardium intensity profile sharpness, the latter by calculating the distance between the 25 and 75 percentiles of peak intensity value. To increase precision in calculating the edge profiles, we interpolated each intensity profile by a factor of 20

(see Figure 6.9 which illustrates our method for computing blood pool CV and intensity edge sharpness).

Visual Analysis of Image Quality

One cardiologist with 17 years and one radiologist with 8 years of clinical experience with CMR graded the image quality. In total, 40 LGE image sets (20 sets each for 3D LA LGE and clinical multi-slice 2D LGE) from 20 patients were randomized and de-identified for display on a DICOM viewer (RadiAnt DICOM Viewer, Medixant, Poznan, Poland). Prior to visual evaluation, the readers were given training data sets with poor to excellent quality to calibrate reader's scores in consensus. Following this training session, the readers independently graded the scores by being blinded to image type, each other's score, and clinical history. The readers graded for each of three categories on a 5-point Likert scale: conspicuity of LA wall (1: nondiagnostic; 2: poor; 3: clinically acceptable; 4: good; 5: excellent), noise and artifact levels (1: nondiagnostic; 2: severe; 3: moderate; 4: mild; 5: minimal). The conspicuity scores were primarily for evaluating visibility of LA wall, whereas noise and artifact scores were evaluated for completeness.

LA Fibrosis Quantification

Only the 3D LA LGE data were analyzed for fibrosis quantification using ADAS 3D (Galgo Medical, Barcelona, Spain). After performing manual segmentation of LA wall, fibrosis was computed by setting the image intensity ratio (IIR)(160) to the following cut points (161): ≤

1.20 defined as normal atrial tissue, > 1.20 and ≤ 1.32 defined as interstitial fibrosis, and > 1.32 defined as dense scar. We did not analyze the multi-slice 2D LGE images because of inadequate spatial resolution and gaps between adjacent slices.

LA Volume Quantification

Segmentation of LA wall in the ADAS 3D software also computes LA volume. We computed LA end-diastolic volume to body surface area ratio (LA EDV/BSA), where BSA was computed using the Mosteller formula. Normal values for LA EDV/BSA were determined from previously published work (males = 52.4 mL/m^2, females = 53.4 mL/m^2) (119).

Statistical Analysis

The statistical analyses were conducted by one investigator (XX). We calculated Cohens' kappa coefficient to determine inter-reader variability in visual scores. Using average reader scores, we used the Wilcoxon signed-rank test to detect differences between two groups. We used paired t-test to detect differences in continuous variables between two tests. A P-value < 0.05 was considered significant for all statistical tests. A sample size of 20 was needed to conduct a Wilcoxon signed-rank test with alpha 0.05, power 0.8, and effect size greater than or equal to 0.68.

6.3 Results

All 20 patients completed 3D LA LGE CMR, which on average required 6:06 ± 0:58 min of scan time. Mean offline XD-GRASP reconstruction time was 3.5 ± 0.7 hours. Figure 6.4 shows representative XD-GRASP images of three different patients before and after BM3D filtering. In each patient, filtering noticeably reduced noise without significant blurring. Averaging results over 20 patients, mean CV of LA blood signal (14 ± 4%) was significantly ($P < 0.001$) reduced after (10 ± 3%) BM3D filtering, whereas the intensity edge-profile was not significantly ($P = 0.64$) different between before (2.07 ± 1.2 mm) and after BM3D filtering (2.04 ± 1.0 mm). Thus, we used BM3D filtered images throughout.

Figure 6.5 shows representative comparisons between the clinical 2D LGE and 3D LA LGE images in a 2-chamber plane. In each of three patients, LGE in the LA wall was more visible in 3D LA LGE than 2D LGE images. As summarized in Table 2, the median conspicuity score was significantly ($P<0.01$) higher for 3D LA LGE (4) than clinical 2D LGE (2.5). As well, the median noise score was significantly higher ($P< 0.01$) for 3D LGE (4) than clinical 2D LGE (3.5). However, the median artifacts scores were not significantly ($P>0.05$) different between 3D LA LGE (4) and clinical 2D LGE (4.5). There was no agreement in individual visual scores assessed by two readers for 3D LGE (kappa = 0 - 0.18) and 2D LGE (kappa = -0.011 - 0.16).

Figure 6.6 shows representative low LA fibrosis (= 5.4%) map of a patient with paroxysmal AF and high LA fibrosis (= 37.2%) map of a patient with persistent AF. Averaging the results over 20 patients (75% paroxysmal AF), mean LA fibrosis was 6.3 ± 7.8% (4.0 ± 2.8% for paroxysmal AF and 13.5 ± 13.3% for persistent AF), and mean LA EDV/BSA was 54.0 ± 21.2 mL/m^2 (47.9 ± 11.7 mL/m^2 for paroxysmal AF and 72.3 ± 33.0 mL/m^2 for persistent AF).

6.4 Discussion

This study describes the development of a 3.3-fold accelerated 3D LA LGE pulse sequence using stack-of-stars k-space sampling, b-SSFP readout, and XD-GRASP reconstruction. The results obtained from 20 AF patients scanned at 1.5 Tesla demonstrate that the proposed 3D LA LGE sequence is capable of producing clinically acceptable image quality (median conspicuity score =4.0) with 1.5 mm x 1.5 mm x 2 mm spatial resolution and 6-minutes predictable scan time for quantification of LA fibrosis. The proposed method also includes BM3D filtering for reducing residual aliasing artifacts and noise while preserving edge sharpness.

This study has several limitations worth emphasizing. First, we did not compare our 3D LA LGE pulse sequence to a previously described 3D LGE pulse sequence (153), because it would be difficult to add another 10-15 min long research pulse sequence onto a clinical CMR examination without significantly altering the clinical workflow or avoiding gadolinium washout effects. Thus, we elected to compare our results with high spatial resolution (1.5 mm x 1.5 mm x 2 mm) to admittedly suboptimal reference in clinical 2D LGE images with poor spatial resolution (2 mm x 2 mm x 6 mm). Second, for quantification of LA fibrosis, we used IIR cut point of 1.2 to define fibrosis based on a prior study which used a different pulse sequence (161). A future study is warranted to derive a cut point statistically by measuring IIR in both healthy controls and AF patients or experimentally by correlating IIR to electroanatomical measurements made during AF ablation procedure. Third, for this initial development work, only 20 AF patients were studied. A future study is warranted to test the performance of the proposed 3D LA LGE pulse sequence and XD-GRASP reconstruction in a diverse cohort of AF patients. Fourth,

we did not consider the impact of arrhythmia during XD-GRASP reconstruction. Irregular heart rhythm is likely to introduce mis-alignment of LA and produce motion artifacts. One approach to address this problem is to expand the XD-GRASP framework to bin the data into two different heartbeat durations (i.e. 5^{th} dimension), at the expense of signal-to-noise ratio (SNR) and residual aliasing artifacts. Fifth, the mean image reconstruction time was 3.5 hours, which is not acceptable for clinical translation. A future study is warranted to explore more rapid image reconstruction pipeline including deep learning and GPU processing.

This study has several interesting points as follows. First, most 3D LGE pulse sequences use a gradient echo readout. However, our experience with 3D LGE using a gradient echo readout at high spatial resolution indicates that it produces poor SNR at 1.5 Tesla. Our experience is consistent with the fact that leading experts in 3D LA LGE (129, 131) favor 3 Tesla. To date, 1.5 Tesla represents highest market share of clinical MRI scanners in US hospitals. We sought to boost the SNR at 1.5 Tesla by using b-SSFP readout, XD-GRASP reconstruction, and BM3D filtering. Second, our pulse sequence achieves a predictable scan time by attaining 100% efficiency in self-navigation of respiratory motion in the XD-GRASP framework. This is an advantage over a standard 3D LGE pulse sequence using conventional navigator gating with patient dependent efficiency. Third, prior 3D LA LGE pulse sequences (129, 131) reported a parallel acceleration factor of 2. Assuming navigator gating efficiency of 40%, the relative scan time with respect to Nyquist sampling with 100% gating efficiency would be 1.25 (i.e. 25% longer than Nyquist sampling with 100% gating efficiency). For our 3.3-fold accelerated acquisition with 100% navigator efficiency, the relative scan time with respect to Nyquist sampling is 0.30. As such, compared with a prior 2-fold accelerated 3D LA LGE pulse

sequence with navigator gating efficiency of 40%, our 3.3-fold accelerated 3D LA LGE with 100% navigator efficiency would be 4.2 times faster, which is significant for lengthy 3D acquisitions such as 3D LA LGE. Fourth, mean LA fibrosis in our cohort (75% paroxysmal AF) was 6.3 ± 7.8% (relatively low), which agrees with findings by a prior study (Utah stage 1: fibrosis = 5% and 60% paroxysmal AF)(130) and relatively normal LA EDV/BSA of 54.0 ± 21.2 mL/m^2 [normal cut points: males = 52.4 mL/m^2, females = 53.4 mL/m^2 (119)].

In summary, this study demonstrates that a 3.3-fold accelerated 3D LA LGE pulse sequence using stack-of-stars k-space sampling, b-SSFP readout, and XD-GRASP reconstruction with 100% navigator efficiency is capable of producing clinically acceptable image quality with 1.5 mm x 1.5 mm x 2 mm spatial resolution and 6-minutes predictable scan time for quantification of LA fibrosis in AF patients at 1.5 Tesla. Future works include establishing pulse sequence specific IIR cut points for quantification of atrial fibrosis and LA fibrosis based risk stratification system for predicting recurrence of AF following catheter ablation.

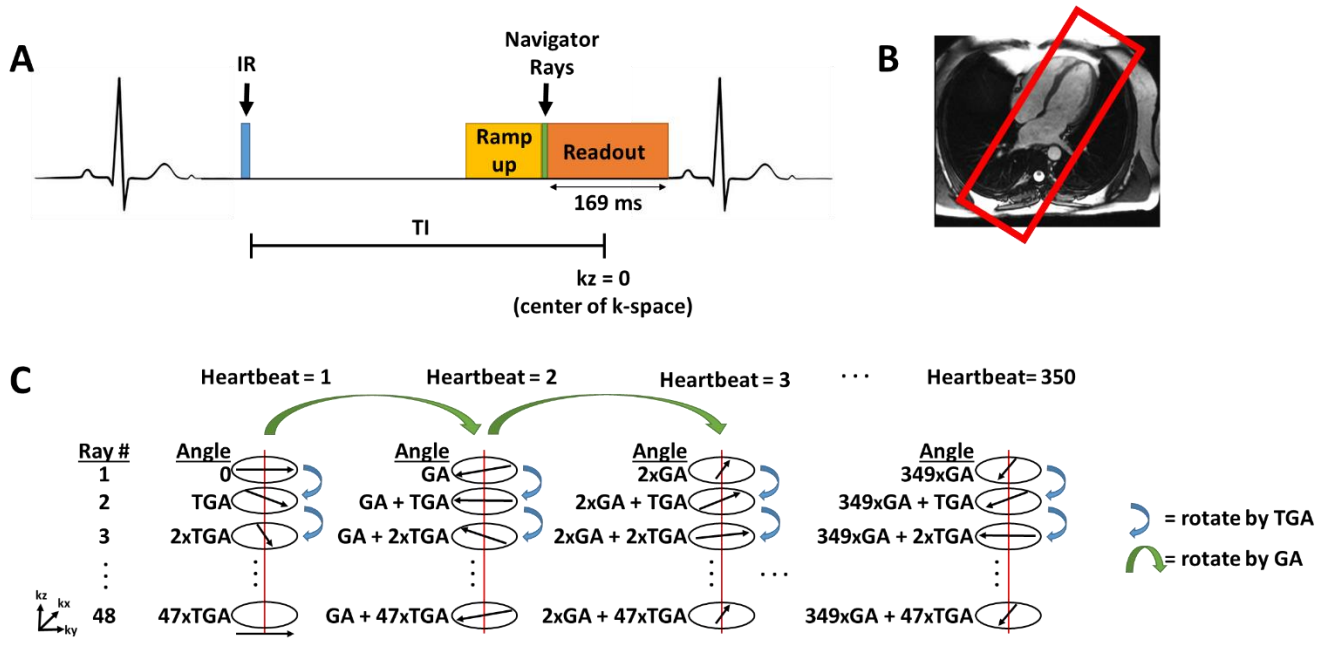

Figure 6.1**:** (A) Pulse sequence timing diagram, (B) orientation of 3D volume sampling the left side of the heart, (C) "winding stair-case" like k-space ordering with TGA sequence along kz and GA sequence along heartbeat. In this acquisition scheme, a unique TI samples the center of k-space, which is ideal for inversion-recovery based LGE. GA = golden angle; TGA = tiny golden angle; HB = heartbeat; TI: inversion time.

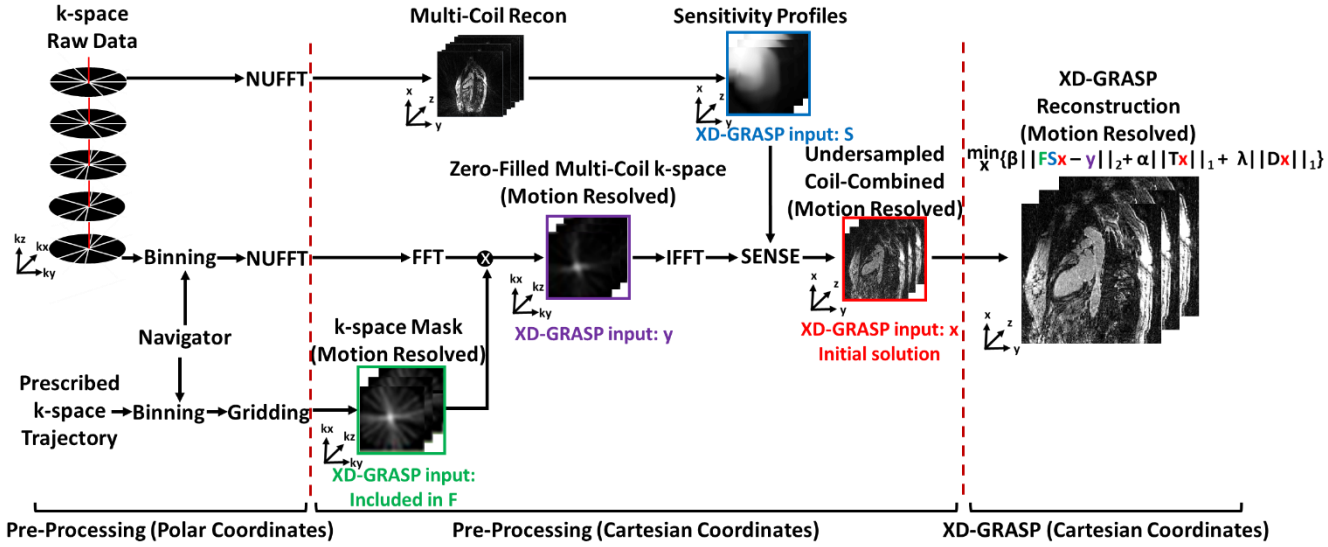

Figure 6.2: XD-GRASP reconstruction pipeline. Using the navigator ray oriented along the head-to-foot direction to extract the respiratory motion, each of six bins were populated with the same number of k-space data by adapting the bin width. In the pre-processing step in polar coordinates, both the non-motion-resolved and motion-resolved stack-of-stars k-space data sets were converted to the corresponding image sets in Cartesian space using NUFFT. The k-space sampling mask in polar coordinates was converted to the corresponding k-space sampling operator (included variable in F) Cartesian space using gridding. In the subsequent pre-processing step in Cartesian coordinates, the coil sensitivities (variable S) were calibrated intrinsically from the non-motion-resolved images as shown. The motion-resolved image in Cartesian space was transformed to k-space using FFT and then multiplied by the k-space sampling operator to produce variable y as shown. Next, the zero-filled, multi-coil, motion-resolved images (variable x) were reconstructed using SENSE along with coil sensitivities as shown. In the CS reconstruction step, we used the finite difference operator as the sparsifying transform along the respiratory dimension and nonlinear conjugate gradient with back-tracking line search as the optimization algorithm with 22 iterations. F represents undersampled FFT, S represents coil sensitivities, and x represents image to be reconstructed, y represents the k-space data, T represents the finite difference operator, α represents the normalized regularization weight, and β represents the normalized fidelity weight. SENSE: sensitivity encoding; FFT: fast Fourier transform; NUFFT: non-uniform FFT.

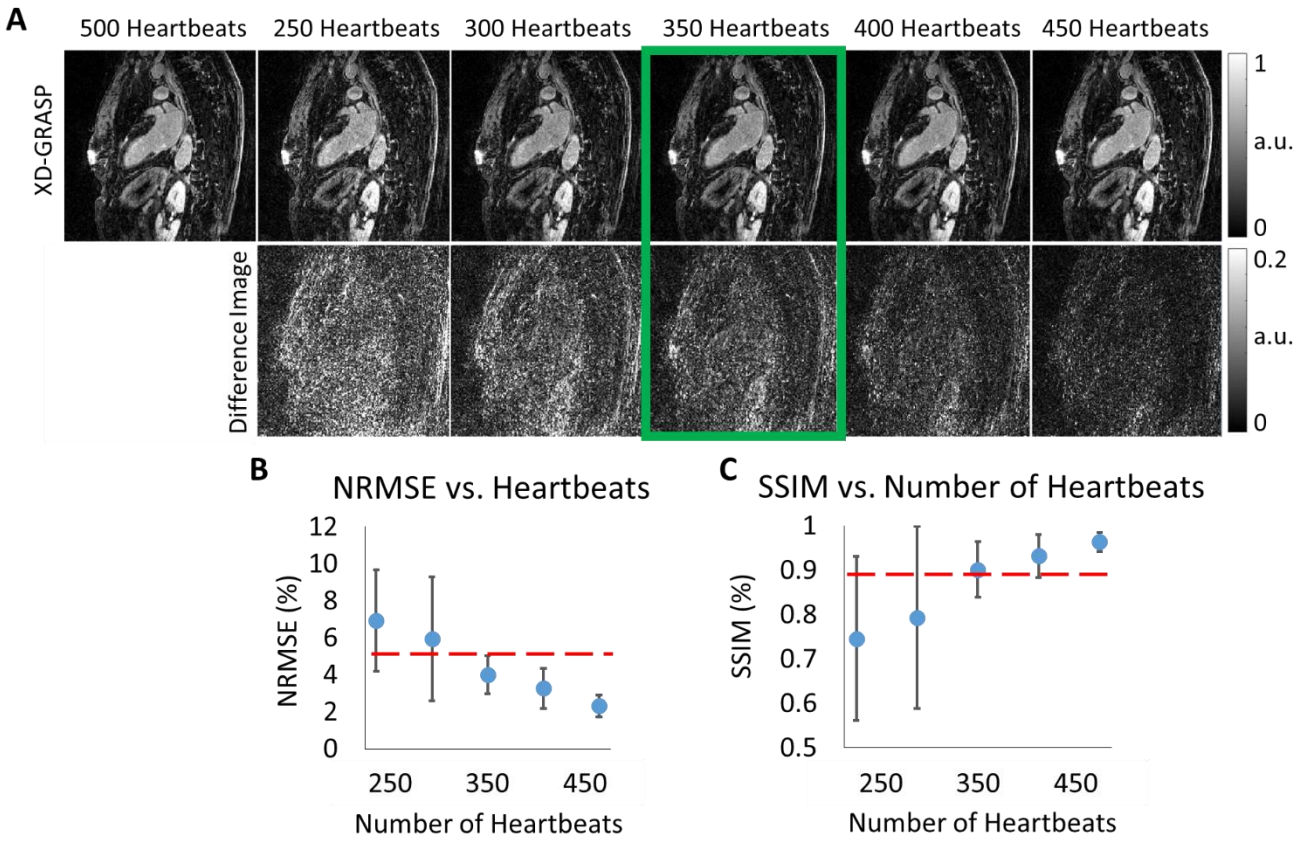

Figure 6.3**:** (A) Schematic describing how optimal acceleration factor was determined relative to 500 heartbeats acquisition (reference) in 3 patients. (B) Plot of NRMSE as a function of number of heartbeats, where NRMSE falls below 5% around 350 heartbeats. (C) Plot of SSIM as a function of number of heartbeats, where SSIM rises above 0.9 around 350 heartbeats. NMRSE: normalized root mean squared error; SSIM: structural similarity index.

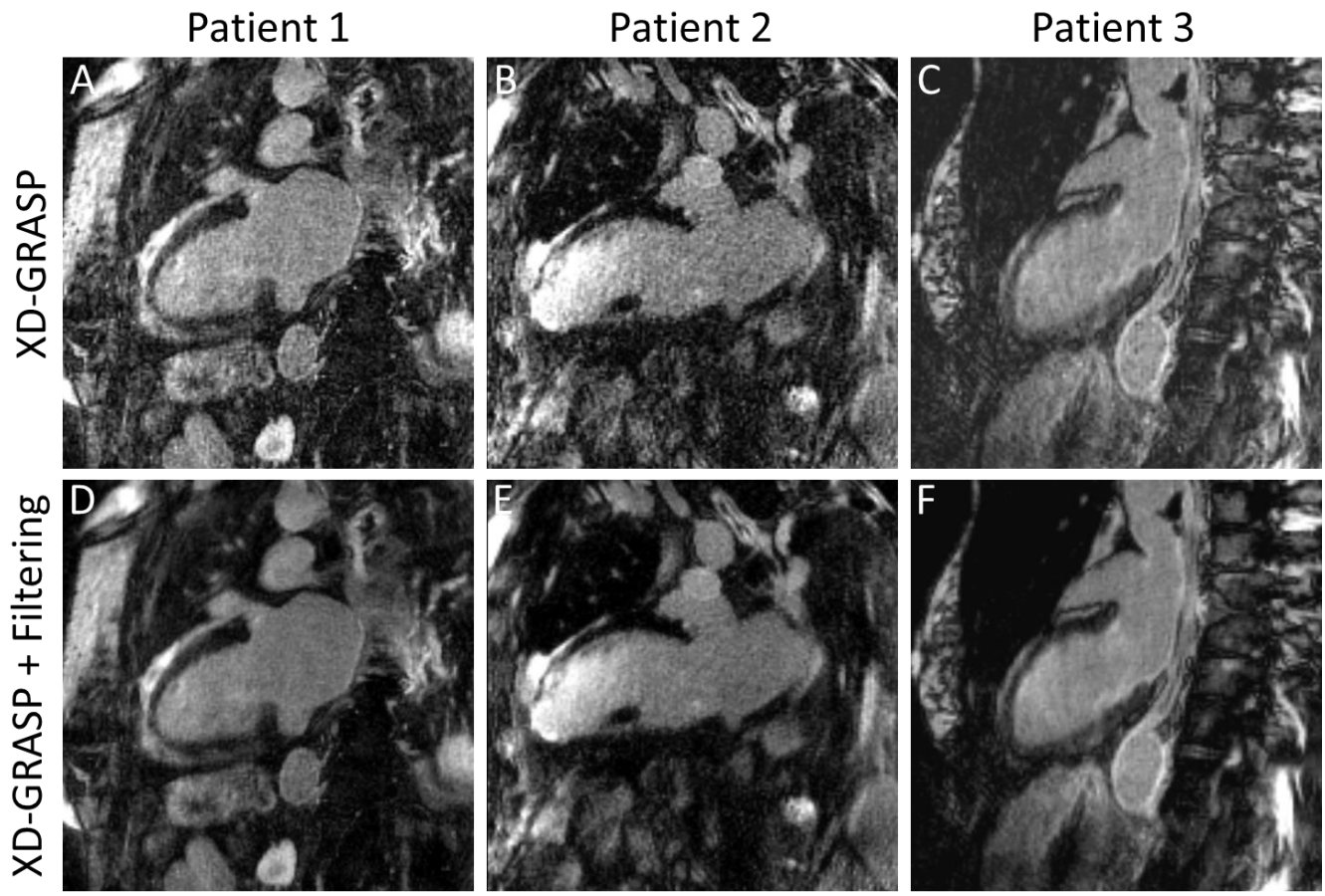

Figure 6.4: XD-GRASP reconstructed images before (top row) and after (bottom row) filtering in 3 patients: patient 1 (left column), patient 2 (middle column), and patient 3 (right column).

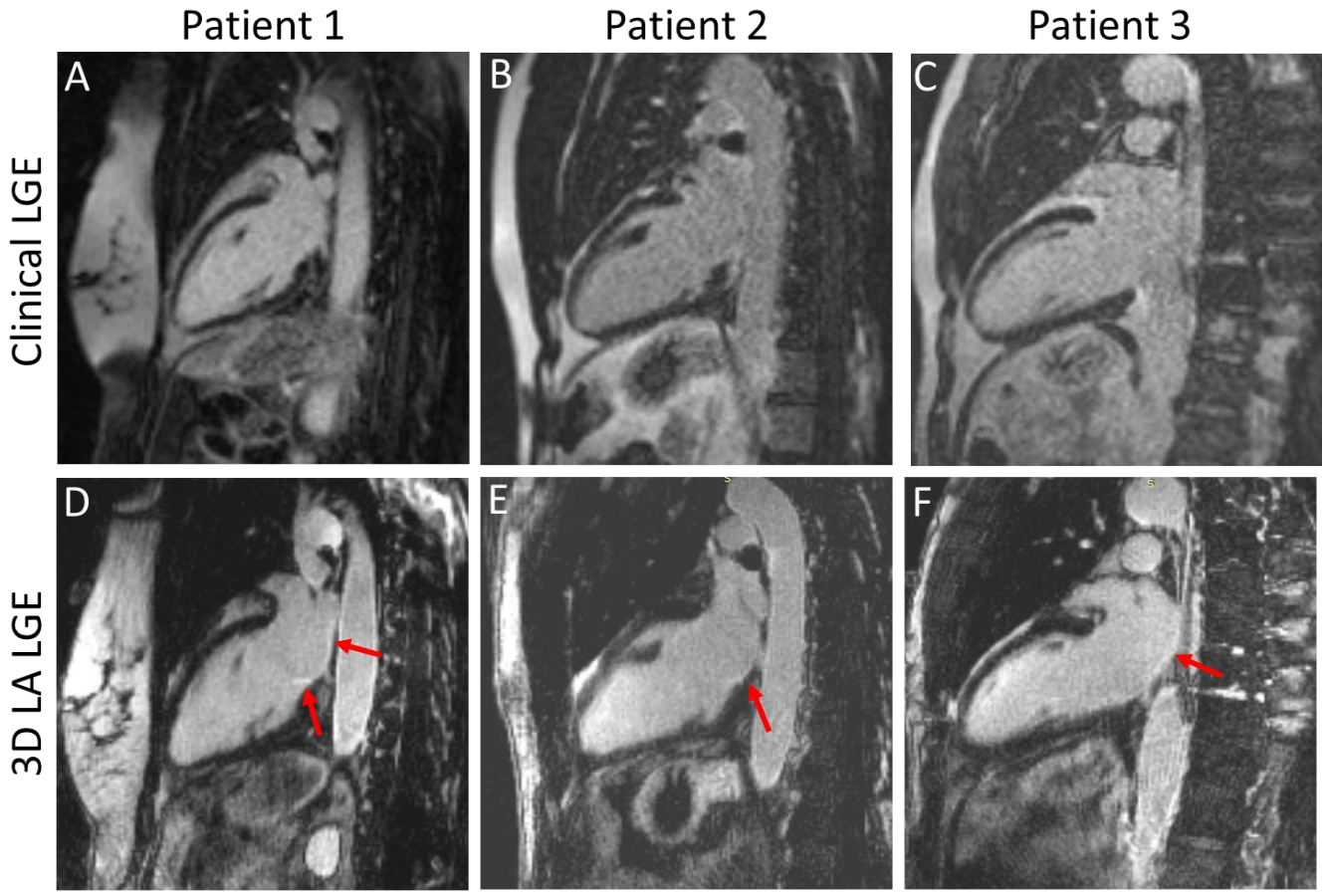

Figure 6.5: Comparison between the clinical 2D LGE (top row) and 3D LA LGE (bottom row) in a 2-chamber view exhibiting the LA. Red arrows indicate areas of LGE that can be appreciated better on 3D LA LGE than standard clinical 2D LGE.

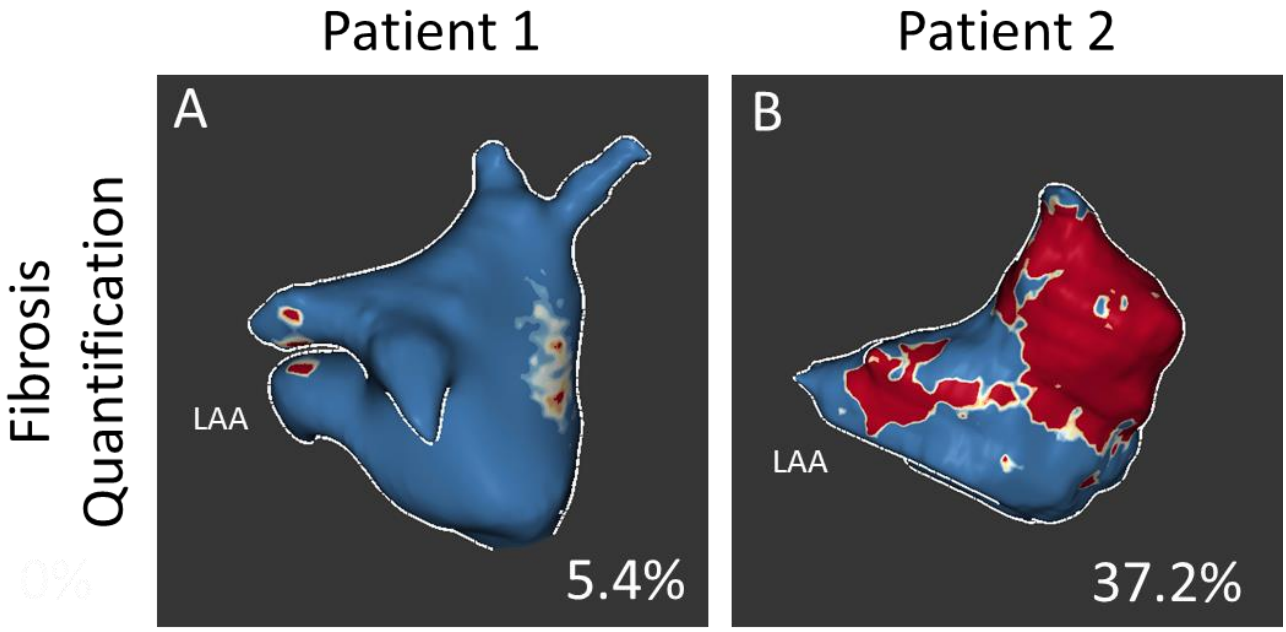

Figure 6.6: Representative LA fibrosis maps of a patient with low (A, 5.4%) and high (B, 37.2%) LA fibrosis as shown. Blue = no fibrosis; gray = interstitial fibrosis; red = dense scarring. LAA = left atrial appendage.

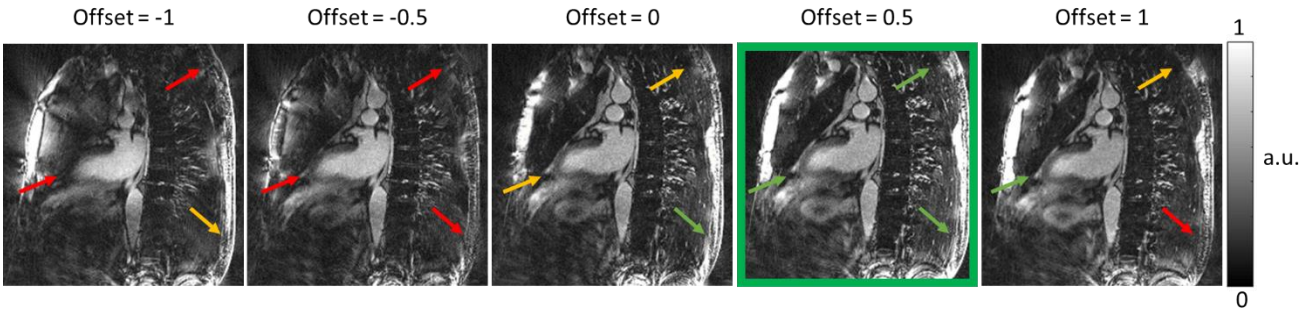

Figure 6.7: Representative images with trajectory correction by manually shifting k-space data from -1 to +1 k-space point. For convenience, only results with 0.5 steps are shown. Arrows point to example areas where signal is examined for overall homogeneous signal. Red = bad signal quality, yellow = acceptable signal quality, green = good signal quality.

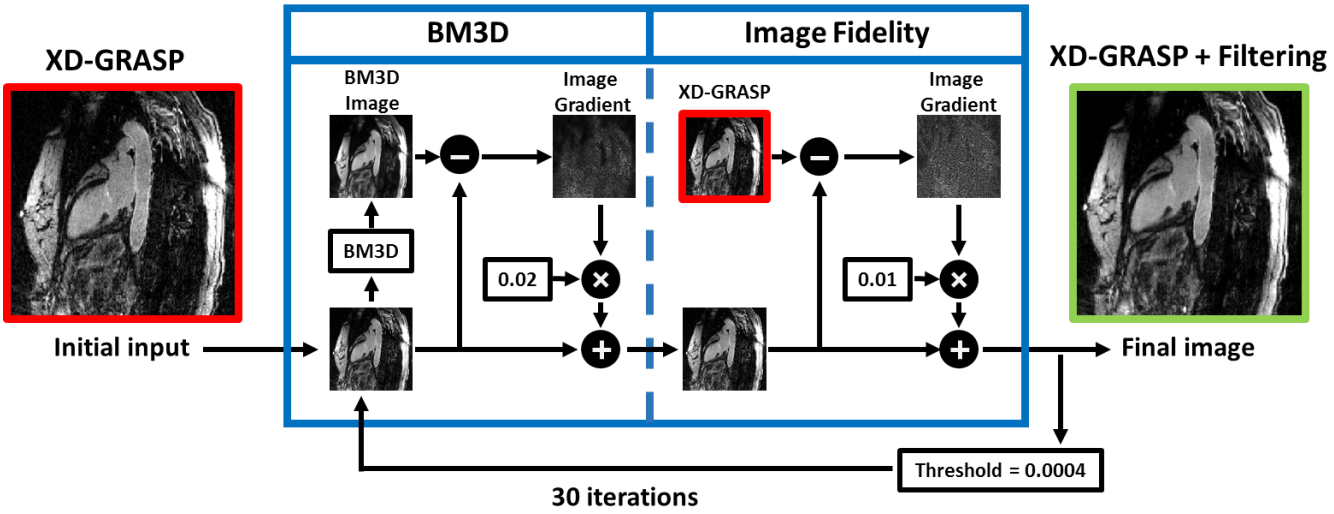

Figure 6.8: Schematics illustrating how a BM3D filter with an image fidelity term is applied with 30 iterations (~4 min) to remove residual aliasing artifact after XD-GRASP reconstruction.

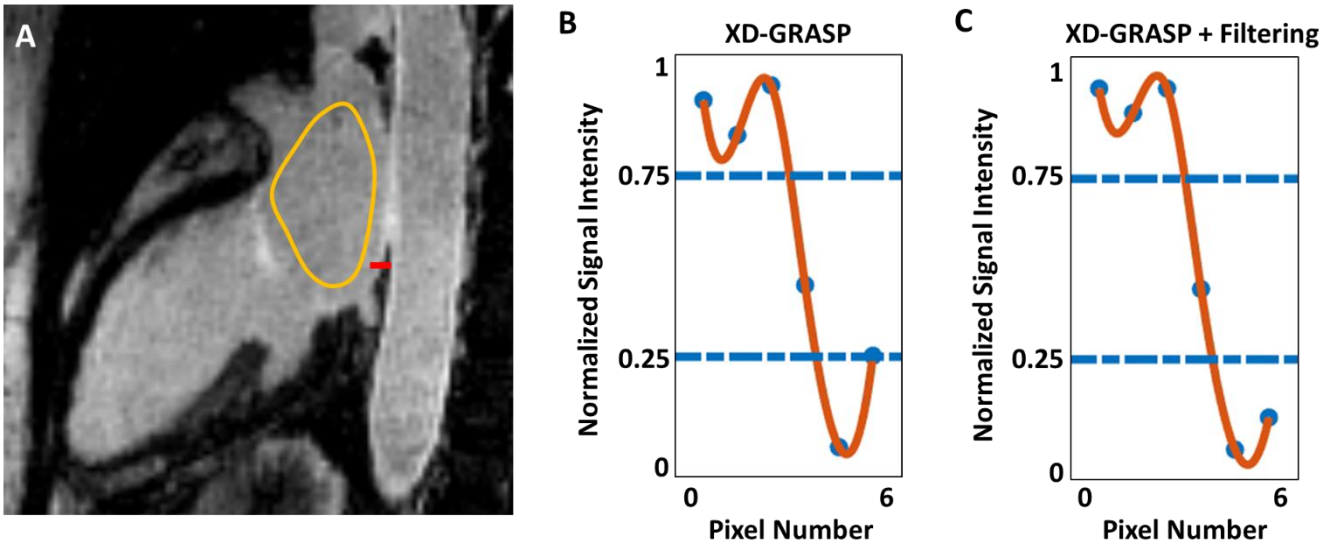

Figure 6.9: Schematics illustrating how (A) CV of LA blood pool (yellow ROI) and (B) intensity edge profiles (from red line in A) are quantified.

7 Conclusions & Future Directions

7.1 Conclusions

CMR is a useful, noninvasive technique that can be used to quantify critical cardiac biomarkers in patients with AF. This dissertation demonstrates that AIR cardiac T_1 mapping is an important MRI sequence for accurately measuring ECV in patients with AF, because it is insensitive to arrhythmia, rapid heart rate, and respiratory motion. After quantifying ECV in AF patients, our results indicate that LV ECV expansion is not associated with AF or AF-mediated LVSD, which was not previously thought. Thus, given the lack of LV ECV expansion, patients with AF-mediated LVSD are likely to benefit from restoration of sinus rhythm with catheter ablation for improvement in LVEF.

Additionally, using the arrhythmia insensitive sequence, AIR T_1 mapping, this work elucidates that neither diffuse LV fibrosis nor other imaging metrics can be used to predict recurrence of AF following catheter ablation. Therefore, diffuse LV fibrosis, as measured by ECV, is likely a poor predictor of AF recurrence following cryoballoon ablation.

Finally, in this dissertation, a new 3.3-fold accelerated 3D LA LGE pulse sequence is described using stack-of-stars k-space sampling, b-SSFP readout, and XD-GRASP reconstruction with 100% navigator efficiency is capable of producing clinically acceptable image quality with 1.5 mm x 1.5 mm x 2 mm spatial resolution and 6-minutes predictable scan time for quantification of LA fibrosis in AF patients at 1.5 Tesla.

7.2 Future Directions

While this work helps bring understanding between AF and fibrosis in the left heart, more work must be done to translate this information into clinically useful AF treatment strategies. Most importantly, determining a biomarker that allows for a risk stratification system for predicting recurrence of AF following catheter ablation would be extremely useful. The 3D LA LGE pulse sequence is promising, but requires additional studies. First, data from the 3D LA LGE must be validated through comparison with electroanatomic mapping or in vivo data (i.e. dog study). Additionally, future work that establishes the cut point for fibrosis, either by correlating against electroanatomic mapping in patients or statistically from healthy volunteers, is a critical component to correctly analyze the data we receive from the LA LGE data. Once the 3D LA LGE sequence is validated, LA fibrosis metrics can be studied against various clinical characteristics of AF patients to future elucidate the role between LA fibrosis and AF to help provide insight into new prevention strategies or treatments to ultimately improve patient outcomes.

References

1. January CT, Wann LS, Alpert JS, Calkins H, Cigarroa JE, Cleveland JC, Jr., et al. 2014 AHA/ACC/HRS guideline for the management of patients with atrial fibrillation: a report of the American College of Cardiology/American Heart Association Task Force on Practice Guidelines and the Heart Rhythm Society. J Am Coll Cardiol. 2014;64(21):e1-76.
2. Go AS, Mozaffarian D, Roger VL, Benjamin EJ, Berry JD, Blaha MJ, et al. Heart disease and stroke statistics--2014 update: a report from the American Heart Association. Circulation. 2014;129(3):e28-e292.
3. Lloyd-Jones DM, Wang TJ, Leip EP, Larson MG, Levy D, Vasan RS, et al. Lifetime risk for development of atrial fibrillation: the Framingham Heart Study. Circulation. 2004;110(9):1042-6.
4. Alonso A, Agarwal SK, Soliman EZ, Ambrose M, Chamberlain AM, Prineas RJ, et al. Incidence of atrial fibrillation in whites and African-Americans: the Atherosclerosis Risk in Communities (ARIC) study. Am Heart J. 2009;158(1):111-7.
5. Kannel WB, Wolf PA, Benjamin EJ, Levy D. Prevalence, incidence, prognosis, and predisposing conditions for atrial fibrillation: population-based estimates. Am J Cardiol. 1998;82(8A):2N-9N.
6. Wang TJ, Larson MG, Levy D, Vasan RS, Leip EP, Wolf PA, et al. Temporal relations of atrial fibrillation and congestive heart failure and their joint influence on mortality: the Framingham Heart Study. Circulation. 2003;107(23):2920-5.
7. Ott A, Breteler MM, de Bruyne MC, van Harskamp F, Grobbee DE, Hofman A. Atrial fibrillation and dementia in a population-based study. The Rotterdam Study. Stroke. 1997;28(2):316-21.
8. Kim MH, Johnston SS, Chu BC, Dalal MR, Schulman KL. Estimation of total incremental health care costs in patients with atrial fibrillation in the United States. Circ Cardiovasc Qual Outcomes. 2011;4(3):313-20.
9. Page RL, Wilkinson WE, Clair WK, McCarthy EA, Pritchett EL. Asymptomatic arrhythmias in patients with symptomatic paroxysmal atrial fibrillation and paroxysmal supraventricular tachycardia. Circulation. 1994;89(1):224-7.
10. January CT, Wann LS, Alpert JS, Calkins H, Cigarroa JE, Cleveland JC, Jr., et al. 2014 AHA/ACC/HRS guideline for the management of patients with atrial fibrillation: a report of the American College of Cardiology/American Heart Association Task Force on practice guidelines and the Heart Rhythm Society. Circulation. 2014;130(23):e199-267.
11. Wyse DG, Van Gelder IC, Ellinor PT, Go AS, Kalman JM, Narayan SM, et al. Lone atrial fibrillation: does it exist? J Am Coll Cardiol. 2014;63(17):1715-23.
12. Healey JS, Wong JA. Subclinical atrial fibrillation: The significance of progression to longer episodes. Heart Rhythm. 2018;15(3):384-5.
13. Wakili R, Voigt N, Kaab S, Dobrev D, Nattel S. Recent advances in the molecular pathophysiology of atrial fibrillation. J Clin Invest. 2011;121(8):2955-68.
14. Franz MR, Jamal SM, Narayan SM. The role of action potential alternans in the initiation of atrial fibrillation in humans: a review and future directions. Europace. 2012;14 Suppl 5:v58-v64.
15. Thompson AE. JAMA patient page. Atrial fibrillation. JAMA. 2015;313(10):1070.
16. Kistler PM, Sanders P, Fynn SP, Stevenson IH, Spence SJ, Vohra JK, et al. Electrophysiologic and electroanatomic changes in the human atrium associated with age. J Am Coll Cardiol. 2004;44(1):109-16.
17. Haissaguerre M, Jais P, Shah DC, Takahashi A, Hocini M, Quiniou G, et al. Spontaneous initiation of atrial fibrillation by ectopic beats originating in the pulmonary veins. N Engl J Med. 1998;339(10):659-66.

18. Schotten U, Verheule S, Kirchhof P, Goette A. Pathophysiological mechanisms of atrial fibrillation: a translational appraisal. Physiol Rev. 2011;91(1):265-325.
19. Kalifa J, Jalife J, Zaitsev AV, Bagwe S, Warren M, Moreno J, et al. Intra-atrial pressure increases rate and organization of waves emanating from the superior pulmonary veins during atrial fibrillation. Circulation. 2003;108(6):668-71.
20. Thijssen VL, Ausma J, Liu GS, Allessie MA, van Eys GJ, Borgers M. Structural changes of atrial myocardium during chronic atrial fibrillation. Cardiovasc Pathol. 2000;9(1):17-28.
21. Wijffels MC, Kirchhof CJ, Dorland R, Allessie MA. Atrial fibrillation begets atrial fibrillation. A study in awake chronically instrumented goats. Circulation. 1995;92(7):1954-68.
22. Corradi D, Callegari S, Benussi S, Nascimbene S, Pastori P, Calvi S, et al. Regional left atrial interstitial remodeling in patients with chronic atrial fibrillation undergoing mitral-valve surgery. Virchows Arch. 2004;445(5):498-505.
23. Wijffels MC, Kirchhof CJ, Dorland R, Power J, Allessie MA. Electrical remodeling due to atrial fibrillation in chronically instrumented conscious goats: roles of neurohumoral changes, ischemia, atrial stretch, and high rate of electrical activation. Circulation. 1997;96(10):3710-20.
24. German DM, Kabir MM, Dewland TA, Henrikson CA, Tereshchenko LG. Atrial Fibrillation Predictors: Importance of the Electrocardiogram. Ann Noninvasive Electrocardiol. 2016;21(1):20-9.
25. Barrett PM, Komatireddy R, Haaser S, Topol S, Sheard J, Encinas J, et al. Comparison of 24-hour Holter monitoring with 14-day novel adhesive patch electrocardiographic monitoring. Am J Med. 2014;127(1):95 e11-7.
26. Webb J, Fovargue L, Tondel K, Porter B, Sieniewicz B, Gould J, et al. The Emerging Role of Cardiac Magnetic Resonance Imaging in the Evaluation of Patients with HFpEF. Curr Heart Fail Rep. 2018;15(1):1-9.
27. Platonov PG. Atrial fibrosis: an obligatory component of arrhythmia mechanisms in atrial fibrillation? J Geriatr Cardiol. 2017;14(3):174-8.
28. Miragoli M, Glukhov AV. Atrial Fibrillation and Fibrosis: Beyond the Cardiomyocyte Centric View. Biomed Res Int. 2015;2015:798768.
29. Gaudesius G, Miragoli M, Thomas SP, Rohr S. Coupling of cardiac electrical activity over extended distances by fibroblasts of cardiac origin. Circ Res. 2003;93(5):421-8.
30. Gyongyosi M, Winkler J, Ramos I, Do QT, Firat H, McDonald K, et al. Myocardial fibrosis: biomedical research from bench to bedside. Eur J Heart Fail. 2017;19(2):177-91.
31. Rathod RH, Powell AJ, Geva T. Myocardial Fibrosis in Congenital Heart Disease. Circ J. 2016;80(6):1300-7.
32. Pitt B, Zannad F. The detection of myocardial fibrosis: an opportunity to reduce cardiovascular risk in patients with diabetes mellitus? Circ Cardiovasc Imaging. 2012;5(1):9-11.
33. Ferrari VA, Witschey WR, Zhou R. Cardiac magnetic resonance assessment of myocardial fibrosis: honing new clinical tools. Circ Cardiovasc Imaging. 2011;4(6):604-6.
34. Ancona R, Comenale Pinto S, Caso P, D'Andrea A, Di Salvo G, Arenga F, et al. Left atrium by echocardiography in clinical practice: from conventional methods to new echocardiographic techniques. ScientificWorldJournal. 2014;2014:451042.
35. Gardner BI, Bingham SE, Allen MR, Blatter DD, Anderson JL. Cardiac magnetic resonance versus transthoracic echocardiography for the assessment of cardiac volumes and regional function after myocardial infarction: an intrasubject comparison using simultaneous intrasubject recordings. Cardiovasc Ultrasound. 2009;7:38.

36. Lotz J, Meier C, Leppert A, Galanski M. Cardiovascular flow measurement with phase-contrast MR imaging: basic facts and implementation. Radiographics. 2002;22(3):651-71.
37. Markl M, Lee DC, Furiasse N, Carr M, Foucar C, Ng J, et al. Left Atrial and Left Atrial Appendage 4D Blood Flow Dynamics in Atrial Fibrillation. Circ Cardiovasc Imaging. 2016;9(9):e004984.
38. Sucu M, Davutoglu V, Ozer O. Electrical cardioversion. Ann Saudi Med. 2009;29(3):201-6.
39. Calkins H, Reynolds MR, Spector P, Sondhi M, Xu Y, Martin A, et al. Treatment of atrial fibrillation with antiarrhythmic drugs or radiofrequency ablation: two systematic literature reviews and meta-analyses. Circ Arrhythm Electrophysiol. 2009;2(4):349-61.
40. Wolf PA, Abbott RD, Kannel WB. Atrial fibrillation as an independent risk factor for stroke: the Framingham Study. Stroke. 1991;22(8):983-8.
41. Kamel H, Okin PM, Elkind MS, Iadecola C. Atrial Fibrillation and Mechanisms of Stroke: Time for a New Model. Stroke. 2016;47(3):895-900.
42. Khan AR, Khan S, Sheikh MA, Khuder S, Grubb B, Moukarbel GV. Catheter ablation and antiarrhythmic drug therapy as first- or second-line therapy in the management of atrial fibrillation: systematic review and meta-analysis. Circulation Arrhythmia and electrophysiology. 2014;7(5):853-60.
43. Wynn GJ, Das M, Bonnett LJ, Panikker S, Wong T, Gupta D. Efficacy of catheter ablation for persistent atrial fibrillation: a systematic review and meta-analysis of evidence from randomized and nonrandomized controlled trials. Circulation Arrhythmia and electrophysiology. 2014;7(5):841-52.
44. Khaykin Y, Morillo CA, Skanes AC, McCracken A, Humphries K, Kerr CR. Cost comparison of catheter ablation and medical therapy in atrial fibrillation. J Cardiovasc Electrophysiol. 2007;18(9):907-13.
45. Dzeshka MS, Lip GY, Snezhitskiy V, Shantsila E. Cardiac Fibrosis in Patients With Atrial Fibrillation: Mechanisms and Clinical Implications. J Am Coll Cardiol. 2015;66(8):943-59.
46. Tan AY, Zimetbaum P. Atrial fibrillation and atrial fibrosis. J Cardiovasc Pharmacol. 2011;57(6):625-9.
47. Burstein B, Nattel S. Atrial fibrosis: mechanisms and clinical relevance in atrial fibrillation. J Am Coll Cardiol. 2008;51(8):802-9.
48. Goldberger JJ, Arora R, Green D, Greenland P, Lee DC, Lloyd-Jones DM, et al. Evaluating the Atrial Myopathy Underlying Atrial Fibrillation: Identifying the Arrhythmogenic and Thrombogenic Substrate. Circulation. 2015;132(4):278-91.
49. Grover VP, Tognarelli JM, Crossey MM, Cox IJ, Taylor-Robinson SD, McPhail MJ. Magnetic Resonance Imaging: Principles and Techniques: Lessons for Clinicians. J Clin Exp Hepatol. 2015;5(3):246-55.
50. Korosec FR, Mistretta CA. MR angiography: basic principles and theory. Magn Reson Imaging Clin N Am. 1998;6(2):223-56.
51. Ridgway JP. Cardiovascular magnetic resonance physics for clinicians: part I. J Cardiovasc Magn Reson. 2010;12:71.
52. Wright KL, Hamilton JI, Griswold MA, Gulani V, Seiberlich N. Non-Cartesian parallel imaging reconstruction. J Magn Reson Imaging. 2014;40(5):1022-40.
53. Glover GH, Pauly JM. Projection reconstruction techniques for reduction of motion effects in MRI. Magn Reson Med. 1992;28(2):275-89.
54. Peters DC, Derbyshire JA, McVeigh ER. Centering the projection reconstruction trajectory: reducing gradient delay errors. Magn Reson Med. 2003;50(1):1-6.
55. Wundrak S, Paul J, Ulrici J, Hell E, Geibel MA, Bernhardt P, et al. Golden ratio sparse MRI using tiny golden angles. Magn Reson Med. 2016;75(6):2372-8.

56. Fessler JA. On NUFFT-based gridding for non-Cartesian MRI. J Magn Reson. 2007;188(2):191-5.
57. Hamilton J, Franson D, Seiberlich N. Recent advances in parallel imaging for MRI. Prog Nucl Magn Reson Spectrosc. 2017;101:71-95.
58. Pruessmann KP, Weiger M, Scheidegger MB, Boesiger P. SENSE: sensitivity encoding for fast MRI. Magn Reson Med. 1999;42(5):952-62.
59. Griswold MA, Jakob PM, Heidemann RM, Nittka M, Jellus V, Wang J, et al. Generalized autocalibrating partially parallel acquisitions (GRAPPA). Magn Reson Med. 2002;47(6):1202-10.
60. Lustig M, Donoho D, Pauly JM. Sparse MRI: The application of compressed sensing for rapid MR imaging. Magn Reson Med. 2007;58(6):1182-95.
61. Jaspan ON, Fleysher R, Lipton ML. Compressed sensing MRI: a review of the clinical literature. Br J Radiol. 2015;88(1056):20150487.
62. Schultz CL, Alfidi RJ, Nelson AD, Kopiwoda SY, Clampitt ME. The effect of motion on two-dimensional Fourier transformation magnetic resonance images. Radiology. 1984;152(1):117-21.
63. Axel L, Summers RM, Kressel HY, Charles C. Respiratory effects in two-dimensional Fourier transform MR imaging. Radiology. 1986;160(3):795-801.
64. Wang Y, Rossman PJ, Grimm RC, Riederer SJ, Ehman RL. Navigator-echo-based real-time respiratory gating and triggering for reduction of respiration effects in three-dimensional coronary MR angiography. Radiology. 1996;198(1):55-60.
65. Feng L, Axel L, Chandarana H, Block KT, Sodickson DK, Otazo R. XD-GRASP: Golden-angle radial MRI with reconstruction of extra motion-state dimensions using compressed sensing. Magn Reson Med. 2016;75(2):775-88.
66. Otazo R, Kim D, Axel L, Sodickson DK. Combination of compressed sensing and parallel imaging for highly accelerated first-pass cardiac perfusion MRI. Magn Reson Med. 2010;64(3):767-76.
67. Benjamin EJ, Blaha MJ, Chiuve SE, Cushman M, Das SR, Deo R, et al. Heart Disease and Stroke Statistics-2017 Update: A Report From the American Heart Association. Circulation. 2017;135(10):e146-e603.
68. Greupner J, Zimmermann E, Grohmann A, Dubel HP, Althoff TF, Borges AC, et al. Head-to-head comparison of left ventricular function assessment with 64-row computed tomography, biplane left cineventriculography, and both 2- and 3-dimensional transthoracic echocardiography: comparison with magnetic resonance imaging as the reference standard. J Am Coll Cardiol. 2012;59(21):1897-907.
69. Grothues F, Moon JC, Bellenger NG, Smith GS, Klein HU, Pennell DJ. Interstudy reproducibility of right ventricular volumes, function, and mass with cardiovascular magnetic resonance. Am Heart J. 2004;147(2):218-23.
70. Yancy CW, Jessup M, Bozkurt B, Butler J, Casey DE, Jr., Drazner MH, et al. 2013 ACCF/AHA guideline for the management of heart failure: a report of the American College of Cardiology Foundation/American Heart Association Task Force on Practice Guidelines. J Am Coll Cardiol. 2013;62(16):e147-239.
71. Weinmann HJ, Brasch RC, Press WR, Wesbey GE. Characteristics of gadolinium-DTPA complex: a potential NMR contrast agent. AJR Am J Roentgenol. 1984;142(3):619-24.
72. Rohrer M, Bauer H, Mintorovitch J, Requardt M, Weinmann HJ. Comparison of magnetic properties of MRI contrast media solutions at different magnetic field strengths. Invest Radiol. 2005;40(11):715-24.
73. Hiratzka LF, Bakris GL, Beckman JA, Bersin RM, Carr VF, Casey DE, Jr., et al. 2010 ACCF/AHA/AATS/ACR/ASA/SCA/SCAI/SIR/STS/SVM guidelines for the diagnosis and management of patients with thoracic aortic disease: executive summary. A report of the American College of Cardiology

Foundation/American Heart Association Task Force on Practice Guidelines, American Association for Thoracic Surgery, American College of Radiology, American Stroke Association, Society of Cardiovascular Anesthesiologists, Society for Cardiovascular Angiography and Interventions, Society of Interventional Radiology, Society of Thoracic Surgeons, and Society for Vascular Medicine. Catheter Cardiovasc Interv. 2010;76(2):E43-86.
74. Mozaffarian D, Benjamin EJ, Go AS, Arnett DK, Blaha MJ, Cushman M, et al. Heart disease and stroke statistics--2015 update: a report from the American Heart Association. Circulation. 2015;131(4):e29-322.
75. Kuruvilla S, Adenaw N, Katwal AB, Lipinski MJ, Kramer CM, Salerno M. Late gadolinium enhancement on cardiac magnetic resonance predicts adverse cardiovascular outcomes in nonischemic cardiomyopathy: a systematic review and meta-analysis. Circ Cardiovasc Imaging. 2014;7(2):250-8.
76. Puntmann VO, Valbuena S, Hinojar R, Petersen SE, Greenwood JP, Kramer CM, et al. Society for Cardiovascular Magnetic Resonance (SCMR) expert consensus for CMR imaging endpoints in clinical research: part I - analytical validation and clinical qualification. J Cardiovasc Magn Reson. 2018;20(1):67.
77. Kramer CM, Barkhausen J, Flamm SD, Kim RJ, Nagel E, Society for Cardiovascular Magnetic Resonance Board of Trustees Task Force on Standardized P. Standardized cardiovascular magnetic resonance imaging (CMR) protocols, society for cardiovascular magnetic resonance: board of trustees task force on standardized protocols. J Cardiovasc Magn Reson. 2008;10:35.
78. Yan AT, Gibson CM, Larose E, Anavekar NS, Tsang S, Solomon SD, et al. Characterization of microvascular dysfunction after acute myocardial infarction by cardiovascular magnetic resonance first-pass perfusion and late gadolinium enhancement imaging. J Cardiovasc Magn Reson. 2006;8(6):831-7.
79. Malcolme-Lawes LC, Juli C, Karim R, Bai W, Quest R, Lim PB, et al. Automated analysis of atrial late gadolinium enhancement imaging that correlates with endocardial voltage and clinical outcomes: a 2-center study. Heart Rhythm. 2013;10(8):1184-91.
80. Quail M, Grunseich K, Baldassarre LA, Mojibian H, Marieb MA, Cornfeld D, et al. Prognostic and functional implications of left atrial late gadolinium enhancement cardiovascular magnetic resonance. J Cardiovasc Magn Reson. 2019;21(1):2.
81. Chelu MG, King JB, Kholmovski EG, Ma J, Gal P, Marashly Q, et al. Atrial Fibrosis by Late Gadolinium Enhancement Magnetic Resonance Imaging and Catheter Ablation of Atrial Fibrillation: 5-Year Follow-Up Data. J Am Heart Assoc. 2018;7(23):e006313.
82. Siebermair J, Kholmovski EG, Marrouche N. Assessment of Left Atrial Fibrosis by Late Gadolinium Enhancement Magnetic Resonance Imaging: Methodology and Clinical Implications. JACC Clin Electrophysiol. 2017;3(8):791-802.
83. Luetkens JA, Wolpers AC, Beiert T, Kuetting D, Dabir D, Homsi R, et al. Cardiac magnetic resonance using late gadolinium enhancement and atrial T1 mapping predicts poor outcome in patients with atrial fibrillation after catheter ablation therapy. Sci Rep. 2018;8(1):13618.
84. Messroghli DR, Radjenovic A, Kozerke S, Higgins DM, Sivananthan MU, Ridgway JP. Modified Look-Locker inversion recovery (MOLLI) for high-resolution T1 mapping of the heart. Magnetic resonance in medicine : official journal of the Society of Magnetic Resonance in Medicine / Society of Magnetic Resonance in Medicine. 2004;52(1):141-6.
85. Piechnik SK, Ferreira VM, Dall'Armellina E, Cochlin LE, Greiser A, Neubauer S, et al. Shortened Modified Look-Locker Inversion recovery (ShMOLLI) for clinical myocardial T1-mapping at 1.5 and 3 T within a 9 heartbeat breathhold. J Cardiovasc Magn Reson. 2010;12:69.
86. Song T, Stainsby JA, Ho VB, Hood MN, Slavin GS. Flexible cardiac T1 mapping using a modified Look-Locker acquisition with saturation recovery. Magn Reson Med. 2012;67(3):622-7.

87. Chow K, Flewitt JA, Green JD, Pagano JJ, Friedrich MG, Thompson RB. Saturation recovery single-shot acquisition (SASHA) for myocardial T(1) mapping. Magn Reson Med. 2014;71(6):2082-95.
88. Weingartner S, Akcakaya M, Basha T, Kissinger KV, Goddu B, Berg S, et al. Combined saturation/inversion recovery sequences for improved evaluation of scar and diffuse fibrosis in patients with arrhythmia or heart rate variability. Magn Reson Med. 2014;71(3):1024-34.
89. Fitts M, Breton E, Kholmovski EG, Dosdall DJ, Vijayakumar S, Hong KP, et al. Arrhythmia insensitive rapid cardiac T1 mapping pulse sequence. Magnetic resonance in medicine : official journal of the Society of Magnetic Resonance in Medicine / Society of Magnetic Resonance in Medicine. 2013;70(5):1274-82.
90. Hong K, Jeong EK, Wall TS, Drakos SG, Kim D. Wideband arrhythmia-Insensitive-rapid (AIR) pulse sequence for cardiac T1 mapping without image artifacts induced by an implantable-cardioverter-defibrillator. Magn Reson Med. 2015;74(2):336-45.
91. Dastidar AG, Harries I, Pontecorboli G, Bruno VD, De Garate E, Moret C, et al. Native T1 mapping to detect extent of acute and chronic myocardial infarction: comparison with late gadolinium enhancement technique. Int J Cardiovasc Imaging. 2019;35(3):517-27.
92. Saunders LC, Johns CS, Stewart NJ, Oram CJE, Capener DA, Puntmann VO, et al. Diagnostic and prognostic significance of cardiovascular magnetic resonance native myocardial T1 mapping in patients with pulmonary hypertension. J Cardiovasc Magn Reson. 2018;20(1):78.
93. Muehlberg F, Funk S, Zange L, von Knobelsdorff-Brenkenhoff F, Blaszczyk E, Schulz A, et al. Native myocardial T1 time can predict development of subsequent anthracycline-induced cardiomyopathy. ESC Heart Fail. 2018;5(4):620-9.
94. Zhao L, Li S, Ma X, Bai R, Liu N, Li N, et al. Prognostic Significance of Left Ventricular Fibrosis Assessed by T1 Mapping in Patients with Atrial Fibrillation and Heart Failure. Sci Rep. 2019;9(1):13374.
95. Kato S, Foppa M, Roujol S, Basha T, Berg S, Kissinger KV, et al. Left ventricular native T1 time and the risk of atrial fibrillation recurrence after pulmonary vein isolation in patients with paroxysmal atrial fibrillation. Int J Cardiol. 2016;203:848-54.
96. Kellman P, Wilson JR, Xue H, Ugander M, Arai AE. Extracellular volume fraction mapping in the myocardium, part 1: evaluation of an automated method. J Cardiovasc Magn Reson. 2012;14:63.
97. Wong TC, Piehler K, Meier CG, Testa SM, Klock AM, Aneizi AA, et al. Association between extracellular matrix expansion quantified by cardiovascular magnetic resonance and short-term mortality. Circulation. 2012;126(10):1206-16.
98. Goldberg A, Jha S. Phase-contrast MRI and applications in congenital heart disease. Clin Radiol. 2012;67(5):399-410.
99. Srichai MB, Lim RP, Wong S, Lee VS. Cardiovascular applications of phase-contrast MRI. AJR Am J Roentgenol. 2009;192(3):662-75.
100. Markl M, Fluckiger J, Lee DC, Ng J, Goldberger JJ. Velocity quantification by electrocardiography-gated phase contrast magnetic resonance imaging in patients with cardiac arrhythmia: a simulation study based on real time transesophageal echocardiography data in atrial fibrillation. J Comput Assist Tomogr. 2015;39(3):422-7.
101. Shively BK, Gelgand EA, Crawford MH. Regional left atrial stasis during atrial fibrillation and flutter: determinants and relation to stroke. J Am Coll Cardiol. 1996;27(7):1722-9.
102. Pelc NJ, Bernstein MA, Shimakawa A, Glover GH. Encoding strategies for three-direction phase-contrast MR imaging of flow. J Magn Reson Imaging. 1991;1(4):405-13.
103. Anter E, Jessup M, Callans DJ. Atrial fibrillation and heart failure: treatment considerations for a dual epidemic. Circulation. 2009;119(18):2516-25.

104. Prabhu S, Taylor AJ, Costello BT, Kaye DM, McLellan AJA, Voskoboinik A, et al. Catheter Ablation Versus Medical Rate Control in Atrial Fibrillation and Systolic Dysfunction: The CAMERA-MRI Study. J Am Coll Cardiol. 2017;70(16):1949-61.
105. Cha YM, Redfield MM, Shen WK, Gersh BJ. Atrial fibrillation and ventricular dysfunction: a vicious electromechanical cycle. Circulation. 2004;109(23):2839-43.
106. Halperin HR, Nazarian S. Atrial fibrillation and diffuse left ventricular fibrosis, a causal association? J Am Coll Cardiol. 2012;60(23):2409-10.
107. Ling LH, Kistler PM, Ellims AH, Iles LM, Lee G, Hughes GL, et al. Diffuse ventricular fibrosis in atrial fibrillation: noninvasive evaluation and relationships with aging and systolic dysfunction. J Am Coll Cardiol. 2012;60(23):2402-8.
108. Messroghli DR, Moon JC, Ferreira VM, Grosse-Wortmann L, He T, Kellman P, et al. Clinical recommendations for cardiovascular magnetic resonance mapping of T1, T2, T2* and extracellular volume: A consensus statement by the Society for Cardiovascular Magnetic Resonance (SCMR) endorsed by the European Association for Cardiovascular Imaging (EACVI). Journal of cardiovascular magnetic resonance : official journal of the Society for Cardiovascular Magnetic Resonance. 2017;19(1):75.
109. Schelbert EB, Sabbah HN, Butler J, Gheorghiade M. Employing Extracellular Volume Cardiovascular Magnetic Resonance Measures of Myocardial Fibrosis to Foster Novel Therapeutics. Circulation Cardiovascular imaging. 2017;10(6):e005619.
110. Neilan TG, Mongeon FP, Shah RV, Coelho-Filho O, Abbasi SA, Dodson JA, et al. Myocardial extracellular volume expansion and the risk of recurrent atrial fibrillation after pulmonary vein isolation. JACC Cardiovasc Imaging. 2014;7(1):1-11.
111. Maanja M, Wieslander B, Schlegel TT, Bacharova L, Abu Daya H, Fridman Y, et al. Diffuse Myocardial Fibrosis Reduces Electrocardiographic Voltage Measures of Left Ventricular Hypertrophy Independent of Left Ventricular Mass. J Am Heart Assoc. 2017;6(1).
112. Koopmann M, Hong K, Kholmovski EG, Huang EC, Hu N, Ying J, et al. Post-contrast myocardial T(1) and ECV disagree in a longitudinal canine study. NMR in biomedicine. 2014;27(8):988-95.
113. Hong K, Collins J, Lee DC, Wilcox JE, Markl M, Carr J, et al. Optimized AIR and investigational MOLLI cardiac T1 mapping pulse sequences produce similar intra-scan repeatability in patients at 3T. NMR in biomedicine. 2016;29(10):1454-63.
114. Gai N, Stehning C, Nacif M, Bluemke D. Modified Look-Locker T1 evaluation using Bloch simulations: Human and phantom validation. Magnetic Resonance in Medicine. 2012;DOI: 10.1002/mrm.24251.
115. Lip GY, Nieuwlaat R, Pisters R, Lane DA, Crijns HJ. Refining clinical risk stratification for predicting stroke and thromboembolism in atrial fibrillation using a novel risk factor-based approach: the euro heart survey on atrial fibrillation. Chest. 2010;137(2):263-72.
116. Rosmini S, Bulluck H, Captur G, Treibel TA, Abdel-Gadir A, Bhuva AN, et al. Myocardial native T1 and extracellular volume with healthy ageing and gender. Eur Heart J Cardiovasc Imaging. 2018;19(6):615-21.
117. Moon JC, Messroghli DR, Kellman P, Piechnik SK, Robson MD, Ugander M, et al. Myocardial T1 mapping and extracellular volume quantification: a Society for Cardiovascular Magnetic Resonance (SCMR) and CMR Working Group of the European Society of Cardiology consensus statement. Journal of cardiovascular magnetic resonance : official journal of the Society for Cardiovascular Magnetic Resonance. 2013;15(1):92.
118. Jiamsripong P, Honda T, Reuss CS, Hurst RT, Chaliki HP, Grill DE, et al. Three methods for evaluation of left atrial volume. Eur J Echocardiogr. 2008;9(3):351-5.

119. Maceira AM, Cosin-Sales J, Roughton M, Prasad SK, Pennell DJ. Reference left atrial dimensions and volumes by steady state free precession cardiovascular magnetic resonance. Journal of cardiovascular magnetic resonance : official journal of the Society for Cardiovascular Magnetic Resonance. 2010;12:65.
120. Shrout PE, Fleiss JL. Intraclass correlations: uses in assessing rater reliability. Psychological bulletin. 1979;86(2):420-8.
121. Zhao L, Li S, Ma X, Greiser A, Zhang T, An J, et al. Systolic MOLLI T1 mapping with heart-rate-dependent pulse sequence sampling scheme is feasible in patients with atrial fibrillation. Journal of cardiovascular magnetic resonance : official journal of the Society for Cardiovascular Magnetic Resonance. 2016;18:13.
122. Ferreira VM, Wijesurendra RS, Liu A, Greiser A, Casadei B, Robson MD, et al. Systolic ShMOLLI myocardial T1-mapping for improved robustness to partial-volume effects and applications in tachyarrhythmias. Journal of cardiovascular magnetic resonance : official journal of the Society for Cardiovascular Magnetic Resonance. 2015;17:77.
123. Packer DL, Bardy GH, Worley SJ, Smith MS, Cobb FR, Coleman RE, et al. Tachycardia-induced cardiomyopathy: a reversible form of left ventricular dysfunction. Am J Cardiol. 1986;57(8):563-70.
124. Ravassa S, Ballesteros G, Lopez B, Ramos P, Bragard J, Gonzalez A, et al. Combination of Circulating Type I Collagen-Related Biomarkers Is Associated With Atrial Fibrillation. J Am Coll Cardiol. 2019;73(12):1398-410.
125. Olchowy C, Cebulski K, Łasecki M, Chaber R, Olchowy A, Kałwak K, et al. The presence of the gadolinium-based contrast agent depositions in the brain and symptoms of gadolinium neurotoxicity-A systematic review. PloS one. 2017;12(2):e0171704.
126. Marrouche NF, Brachmann J, Andresen D, Siebels J, Boersma L, Jordaens L, et al. Catheter Ablation for Atrial Fibrillation with Heart Failure. N Engl J Med. 2018;378(5):417-27.
127. Spragg D. Left Atrial Fibrosis: Role in Atrial Fibrillation Pathophysiology and Treatment Outcomes. Journal of atrial fibrillation. 2013;5(6):810.
128. Mahnkopf C, Badger TJ, Burgon NS, Daccarett M, Haslam TS, Badger CT, et al. Evaluation of the left atrial substrate in patients with lone atrial fibrillation using delayed-enhanced MRI: implications for disease progression and response to catheter ablation. Heart Rhythm. 2010;7(10):1475-81.
129. Oakes RS, Badger TJ, Kholmovski EG, Akoum N, Burgon NS, Fish EN, et al. Detection and quantification of left atrial structural remodeling with delayed-enhancement magnetic resonance imaging in patients with atrial fibrillation. Circulation. 2009;119(13):1758-67.
130. Akoum N, Daccarett M, McGann C, Segerson N, Vergara G, Kuppahally S, et al. Atrial fibrosis helps select the appropriate patient and strategy in catheter ablation of atrial fibrillation: a DE-MRI guided approach. Journal of cardiovascular electrophysiology. 2011;22(1):16-22.
131. McGann C, Akoum N, Patel A, Kholmovski E, Revelo P, Damal K, et al. Atrial fibrillation ablation outcome is predicted by left atrial remodeling on MRI. Circ Arrhythm Electrophysiol. 2014;7(1):23-30.
132. Patel JJ, Whittaker CT. Tachycardia-induced heart failure. Perm J. 2007;11(3):50-2.
133. Abraham WT, Fisher WG, Smith AL, Delurgio DB, Leon AR, Loh E, et al. Cardiac resynchronization in chronic heart failure. N Engl J Med. 2002;346(24):1845-53.
134. Auricchio A, Ding J, Spinelli JC, Kramer AP, Salo RW, Hoersch W, et al. Cardiac resynchronization therapy restores optimal atrioventricular mechanical timing in heart failure patients with ventricular conduction delay. J Am Coll Cardiol. 2002;39(7):1163-9.
135. Timek T, Dagum P, Lai DT, Green GR, Glasson JR, Daughters GT, et al. The role of atrial contraction in mitral valve closure. J Heart Valve Dis. 2001;10(3):312-9.

136. Keren G, Bier A, Sherez J, Miura D, Keefe D, LeJemtel T. Atrial contraction is an important determinant of pulmonary venous flow. Journal of the American College of Cardiology. 1986;7(3):693-5.
137. Gertz ZM, Raina A, Saghy L, Zado ES, Callans DJ, Marchlinski FE, et al. Evidence of atrial functional mitral regurgitation due to atrial fibrillation: reversal with arrhythmia control. J Am Coll Cardiol. 2011;58(14):1474-81.
138. Delgado V, Bax JJ. Atrial Functional Mitral Regurgitation: From Mitral Annulus Dilatation to Insufficient Leaflet Remodeling. Circ Cardiovasc Imaging. 2017;10(3).
139. Avitall B, Bi J, Mykytsey A, Chicos A. Atrial and ventricular fibrosis induced by atrial fibrillation: evidence to support early rhythm control. Heart rhythm : the official journal of the Heart Rhythm Society. 2008;5(6):839-45.
140. McLellan AJ, Ling LH, Azzopardi S, Ellims AH, Iles LM, Sellenger MA, et al. Diffuse ventricular fibrosis measured by T(1) mapping on cardiac MRI predicts success of catheter ablation for atrial fibrillation. Circulation Arrhythmia and electrophysiology. 2014;7(5):834-40.
141. Tsekos NV, Zhang Y, Merkle H, Wilke N, Jerosch-Herold M, Stillman A, et al. Fast anatomical imaging of the heart and assessment of myocardial perfusion with arrhythmia insensitive magnetization preparation. Magnetic resonance in medicine : official journal of the Society of Magnetic Resonance in Medicine / Society of Magnetic Resonance in Medicine. 1995;34(4):530-6.
142. Rosenthal RL. The 50% coronary stenosis. Am J Cardiol. 2015;115(8):1162-5.
143. American College of Cardiology Foundation/American Heart Association Task Force on P, American Association for Thoracic S, American Society of E, American Society of Nuclear C, Heart Failure Society of A, Heart Rhythm S, et al. 2011 ACCF/AHA guideline for the diagnosis and treatment of hypertrophic cardiomyopathy: a report of the American College of Cardiology Foundation/American Heart Association Task Force on Practice Guidelines. J Thorac Cardiovasc Surg. 2011;142(6):e153-203.
144. Gunasekaran S, Lee D, Knight B, Fan L, Collins J, Chow K, et al. Left ventricular extracellular volume expansion is not associated with atrial fibrillation or atrial fibrillation-mediated left ventricular systolic dysfunction. Radiology: Cardiothoracic Imaging.(in press).
145. Takigawa M, Takahashi A, Kuwahara T, Okubo K, Takahashi Y, Watari Y, et al. Long-term follow-up after catheter ablation of paroxysmal atrial fibrillation: the incidence of recurrence and progression of atrial fibrillation. Circ Arrhythm Electrophysiol. 2014;7(2):267-73.
146. Miyazaki S, Kuwahara T, Kobori A, Takahashi Y, Takei A, Sato A, et al. Long-term clinical outcome of extensive pulmonary vein isolation-based catheter ablation therapy in patients with paroxysmal and persistent atrial fibrillation. Heart. 2011;97(8):668-73.
147. Brooks AG, Stiles MK, Laborderie J, Lau DH, Kuklik P, Shipp NJ, et al. Outcomes of long-standing persistent atrial fibrillation ablation: a systematic review. Heart Rhythm. 2010;7(6):835-46.
148. Clarnette JA, Brooks AG, Mahajan R, Elliott AD, Twomey DJ, Pathak RK, et al. Outcomes of persistent and long-standing persistent atrial fibrillation ablation: a systematic review and meta-analysis. Europace. 2018;20(FI_3):f366-f76.
149. Suksaranjit P, Akoum N, Kholmovski EG, Stoddard GJ, Chang L, Damal K, et al. Incidental LV LGE on CMR Imaging in Atrial Fibrillation Predicts Recurrence After Ablation Therapy. JACC Cardiovasc Imaging. 2015;8(7):793-800.
150. Kim RJ, Fieno DS, Parrish TB, Harris K, Chen EL, Simonetti O, et al. Relationship of MRI delayed contrast enhancement to irreversible injury, infarct age, and contractile function. Circulation. 1999;100(19):1992-2002.

151. Peters DC, Wylie JV, Hauser TH, Kissinger KV, Botnar RM, Essebag V, et al. Detection of pulmonary vein and left atrial scar after catheter ablation with three-dimensional navigator-gated delayed enhancement MR imaging: initial experience. Radiology. 2007;243(3):690-5.
152. Hu C, Sinusas AJ, Huber S, Thorn S, Stacy MR, Mojibian H, et al. T1-refBlochi: high resolution 3D post-contrast T1 myocardial mapping based on a single 3D late gadolinium enhancement volume, Bloch equations, and a reference T1. J Cardiovasc Magn Reson. 2017;19(1):63.
153. Pontecorboli G, Figueras IVRM, Carlosena A, Benito E, Prat-Gonzales S, Padeletti L, et al. Use of delayed-enhancement magnetic resonance imaging for fibrosis detection in the atria: a review. Europace : European pacing, arrhythmias, and cardiac electrophysiology : journal of the working groups on cardiac pacing, arrhythmias, and cardiac cellular electrophysiology of the European Society of Cardiology. 2017;19(2):180-9.
154. Haji-Valizadeh H, Collins JD, Aouad PJ, Serhal AM, Lindley MD, Pang J, et al. Accelerated, free-breathing, noncontrast, electrocardiograph-triggered, thoracic MR angiography with stack-of-stars k-space sampling and GRASP reconstruction. Magnetic resonance in medicine : official journal of the Society of Magnetic Resonance in Medicine / Society of Magnetic Resonance in Medicine. 2019;81(1):524-32.
155. Gupta A, Lee VS, Chung YC, Babb JS, Simonetti OP. Myocardial infarction: optimization of inversion times at delayed contrast-enhanced MR imaging. Radiology. 2004;233(3):921-6.
156. Adluru G, DiBella E. Compression2: compressed sensing with compressed coil arrays. Journal of Cardiovascular Magnetic Resonance. 2012;14(Suppl 1):P242.
157. Feng L, Srichai MB, Lim RP, Harrison A, King W, Adluru G, et al. Highly accelerated real-time cardiac cine MRI using k-t SPARSE-SENSE. Magnetic resonance in medicine : official journal of the Society of Magnetic Resonance in Medicine / Society of Magnetic Resonance in Medicine. 2013;70(1):64-74.
158. Wang Z, Bovik AC, Sheikh HR, Simoncelli EP. Image quality assessment: from error visibility to structural similarity. IEEE transactions on image processing : a publication of the IEEE Signal Processing Society. 2004;13(4):600-12.
159. Dabov K, Foi A, Katkovnik V, Egiazarian K. Image denoising by sparse 3-D transform-domain collaborative filtering. IEEE Trans Image Process. 2007;16(8):2080-95.
160. Khurram IM, Beinart R, Zipunnikov V, Dewire J, Yarmohammadi H, Sasaki T, et al. Magnetic resonance image intensity ratio, a normalized measure to enable interpatient comparability of left atrial fibrosis. Heart rhythm : the official journal of the Heart Rhythm Society. 2014;11(1):85-92.
161. Benito EM, Carlosena-Remirez A, Guasch E, Prat-Gonzalez S, Perea RJ, Figueras R, et al. Left atrial fibrosis quantification by late gadolinium-enhanced magnetic resonance: a new method to standardize the thresholds for reproducibility. Europace : European pacing, arrhythmias, and cardiac electrophysiology : journal of the working groups on cardiac pacing, arrhythmias, and cardiac cellular electrophysiology of the European Society of Cardiology. 2017;19(8):1272-9.